

Washington University in St. Louis

Washington University Open Scholarship

McKelvey School of Engineering Theses & Dissertations

McKelvey School of Engineering

Spring 5-15-2020

Ultrasensitive Biodetection based on Plasmonically-active Materials

Jingyi Luan

Washington University in St. Louis

Follow this and additional works at: https://openscholarship.wustl.edu/eng_etds



Part of the [Biomedical Engineering and Bioengineering Commons](#)

Recommended Citation

Luan, Jingyi, "Ultrasensitive Biodetection based on Plasmonically-active Materials" (2020). *McKelvey School of Engineering Theses & Dissertations*. 548.

https://openscholarship.wustl.edu/eng_etds/548

This Dissertation is brought to you for free and open access by the McKelvey School of Engineering at Washington University Open Scholarship. It has been accepted for inclusion in McKelvey School of Engineering Theses & Dissertations by an authorized administrator of Washington University Open Scholarship. For more information, please contact digital@wumail.wustl.edu.

WASHINGTON UNIVERSITY IN ST. LOUIS
DEPARTMENT OF MECHANICAL ENGINEERING & MATERIALS SCIENCE

Dissertation Examination Committee:
Srikanth Singamaneni, Chair
Shantanu Chakrabartty
Guy Genin
Rohan Mishra
Jeremiah Morrissey

Ultrasensitive Biodetection based on
Plasmonically-active Materials
by
Jingyi Luan

A dissertation presented to
The Graduate School
of Washington University in
partial fulfillment of the
requirements for the degree
of Doctor of Philosophy

May 2020

Saint Louis, Missouri

© 2020, Jingyi Luan

Table of Contents

List of Figures	v
List of abbreviations	xiii
Acknowledgments.....	xvii
Abstract of dissertation	xix
Chapter 1: Research goals and objective	1
1.1 Objective 1	2
Introduce simple and broadly applicable plasmonically-active material platforms for ultrasensitive biodetection.....	2
Task 1: Realize plasmonically-active elastomeric films that can readily serve as fluorescence enhancers in conventional fluoroimmunoassays.	2
Task 2: Understand the effects of optical properties of the plasmonic patches on the fluorescence enhancement efficiency.....	2
Task 3: Design and realize an ultrabright fluorescent nanolabel based on plasmonic nanoantennas that readily improve the bioanalytical parameters of a wide range of fluorescence based analytical and imaging techniques.	2
1.2 Objective 2	2
Understand the sensitivity, specificity, and stability of artificial biorecognition elements realized through molecular imprinting on plasmonic nanostructures as a function of their surface/interfacial properties and composition.	2
Task 1: Compare the stability of plasmonic biosensor based on artificial antibody and natural antibody.	2
Task 2: Design and develop a surface PEGylation method of artificial antibody to improve the selectivity of the plasmonic biosensor.....	2
Task 3: Understand the role of aromatic interactions in the biorecognition capabilities of artificial antibody based plasmonic biosensor.....	2
Chapter 2: Background and motivation	3
2.1 Localized Surface Plasmon Resonance (LSPR).....	3
2.2 Plasmon-enhanced fluorescence	4
2.3 Label-free plasmonic biological sensors based on synthetic biorecognition element (artificial antibody).....	5
Chapter 3: Add-on plasmonic patch as universal fluorescence enhancer.....	7

3.1 Introduction	7
3.2 Results and discussion.....	9
3.2.1 Plasmonic patch fabrication and material characterization.	10
3.2.2 Distance-dependent fluorescence enhancement and spacer layer.	11
3.2.3 Patterned plasmonic patch and localized fluorescence enhancement.	12
3.2.4 Plasmonic patch-enhanced fluoroimmunoassays.	13
3.2.5 Application of a plasmonic patch on a protein microarray.	17
3.3 Conclusions	19
3.4 Materials and Methods	22
3.5 Figures	24
Chapter 4: Gold Nanorod Size-dependent Fluorescence Enhancement	30
4.1 Introduction	30
4.2 Results and discussion.....	31
4.3 Conclusions	38
4.4 Experimental section	39
4.5 Figures	43
Chapter 5: Ultrabright Plasmonic-fluor as a Cross-platform Nanolabel for Femtomolar Detection of Bioanalytes	49
5.1 Introduction	49
5.2 Results and discussion.....	51
5.2.1 Fabrication of plasmonic-fluor.	51
5.2.2 Plasmonic-fluor enhanced fluorescence-linked immunosorbent assay (p-FLISA) and multiplexed bead-based assay	55
5.2.3 Plasmonic-fluor enhanced high throughput multiplexed proteomic array	60
5.2.4 Plasmonic-fluor enhanced immunocytochemistry/immunofluorescence (ICC/IF).....	62
5.2.5 Plasmonic-fluor enhanced flow cytometry measurement	63
5.3 Conclusions	66
5.4. Figures	67
Chapter 6: Environmental Stability of Plasmonic Biosensors based on Natural vs. Artificial Antibody	74
6.1 Introduction	74
6.2 Results and discussion.....	77

6.3 Conclusion.....	83
6.4 Experimental section	84
6.5 Figures:	88
Chapter 7: PEGylated Artificial Antibodies: Plasmonic Biosensors with Improved Selectivity .	93
7.1 Introduction	93
7.2 Results and discussion.....	95
7.3 Conclusions	103
7.4 Figures	104
Chapter 8: Aromatic functionality of target proteins influences monomer selection for creating artificial antibodies on plasmonic biosensors	108
8.1 Introduction	108
8.2 Results and Discussion.....	110
8.3 Conclusions	116
8.4 Experimental Section	117
8.5 Figures.....	121
Chapter 9: Conclusions	125
9.1 General conclusions	125
9.2 Significance and outlook.....	128
Reference	129
Curriculum Vitae	141

List of Figures

Figure 1. 1 Illustration outlining the overall research goal. 1

Figure 3. 1 (A) Schematic illustration of the fabrication of a plasmonic patch and its application in fluoroimmunoassays. A large enhancement in the fluorescence signal is simply achieved by the transfer of the plasmonic patch onto a surface with fluorescent species. This “add-on” step does not change the well-established procedures of current fluoroimmunoassays and can thus be seamlessly integrated with a variety of existing assays to significantly enhance their fluorescence. (B) Top: Photograph showing the transfer of a plasmonic patch to a planar surface. Middle: SEM image demonstrating the flexibility, as well as conformability to the substrate, of the plasmonic patch. Bottom: SEM image of the cross-section of the plasmonic patch showing an average thickness of 30 μm . (C) Normalized extinction spectra of aqueous solutions of the three representative plasmonic nanostructures employed in this study (from left to right: Au@Ag-490, AuNR-670, and AuNR-760). The extinction bands of Au@Ag-490, AuNR-670, and AuNR-760 exhibit significant overlap with the absorption bands (excitation source) of FITC, 680LT, and 800CW, respectively. (D) SEM images of the plasmonic patch surface revealing the uniform distribution of plasmonic nanostructures on PDMS (from left to right: Au@Ag-490, AuNR-670, and AuNR-760). Insets show representative TEM images of the corresponding plasmonic nanostructures. (E) Photograph of plasmonic patches modified with various nanostructures (left). The flexibility of the plasmonic patch is further demonstrated by rolling it around a cylindrical support (right). The scale bar represents 1 cm. (F) Fluorescence map of three fluorophores adsorbed on a silicon substrate in the presence and absence of a plasmonic patch (left scale bar represents 10 μm ; middle and right scale bars represent 1 mm). 24

Figure 3. 2 (A) Schematic illustration showing a plasmonic patch with a polymer layer acting as a spacer between fluorophores and plasmonic nanostructures. The spacer thickness is optimized to achieve the maximum enhancement efficiency. (B) Fluorescence map of 800CW in the presence of plasmonic patches with increasing spacer layer thickness (TMPS and APTMS volume ratio is 0:0, 0:8, 0.25:8, 0.5:8, 1:8, 4:8, and 8:8 from left to right). (C) Fluorescence enhancement factor as a function of the spacer thickness (TMPS amount in the polymerization process). (D) AFM images of pristine Au nanorods (left) and Au nanorods with a polymer spacer (right) (TMPS and APTMS volume ratio of 4:8). 25

Figure 3. 3 (A) Schematic showing a patterned plasmonic patch, which selectively enhances the fluorescence in the regions of conformal contact. In all of the used patterns, the height of the surface-relief portions is greater than 200 nm. SEM image of a (B) stripe array and (C) square lattice PDMS with Au@Ag-490 adsorbed (insets show zoomed-in SEM images of the highlighted area revealing a uniform distribution of the plasmonic nanostructures on both elevated and surface-relief regions; inset scale bars represent 500 μm). AFM images of (D) stripe array (z scale: 430

nm) and (E) square lattice (z scale: 200 nm) plasmonic patches revealing the height profile of the surfaces. Fluorescence images of an FITC-coated silicon surface with (F) stripe array and (G) square lattice plasmonic patches on top. The plots below reveal the fluorescence intensity profiles. (H) Fluorescence map of FITC with a plasmonic patch (with Au@Ag-490 adsorbed) with circular pores. (I) Fluorescence image (800CW) of the “Washington University in St. Louis” logo obtained using a plasmonic patch (with AuNR-760 adsorbed) with an engraved logo. 26

Figure 4. 1 (A) Schematic representation of the simple “add-on” process to enhance the fluorescence emission based on an elastomeric plasmonic patch. (B) Photographs of plasmonic patch comprised of gold nanorods (AuNRs). (C) SEM image of the plasmonic patch showing the high flexibility. (D) Zoom-in SEM image of the interface between the plasmonic patch and the silicon substrate showing the high conformability. 43

Figure 4. 2 (A) TEM images of AuNRs with increasing size (length×diameter) (B) Aspect ratio of the AuNRs shown (A). (c) Normalized extinction spectra of the aqueous solutions of AuNRs, showing similar LSPR wavelength. 44

Figure 4. 3 (A) SEM images of the plasmonic patch revealing similar density of different size AuNRs on PDMS (from left to right: AuNR-46×18nm, AuNR-57×18nm, AuNR-62×18nm, AuNR-85×24nm, AuNR-105×31nm, AuNR-113×38nm, AuNR-130×40nm and AuNR-155×48nm). (B) Vis-NIR extinction spectra of the plasmonic patches comprised of AuNRs with different dimensions after being transferred to 96-well plate, which exhibit a slight red shift compared to the LSPR wavelength in aqueous solutions. (C) The fluorescence map and (D) calculated enhancement factors of emission of 800CW using the plasmonic patches with AuNR of different sizes. (E) Finite-difference time-domain (FDTD) simulation, showing electromagnetic field around AuNRs with different sizes (Scale bar represents 50 nm). (F) Plot showing the electromagnetic field intensity enhancement for AuNRs of different dimensions (from length 46 nm to 200 nm). 45

Figure 4. 4 (A) SEM images of the plasmonic patch AuNR-130×40nm with increasing density of AuNR. (B) Extinction spectra of plasmonic patches of AuNR-130×40nm with different AuNR densities after transferring them to 96 well plate. (C) Fluorescence maps and (D) plot showing the fluorescence enhancement efficacy of plasmonic patches with different AuNR density. (E) Simulated spectra of AuNR-130×40 nm with incident light polarized along the long-axis of the AuNR. (F) Illustration showing the finite-difference time-domain (FDTD) simulation of AuNR 130×40 nm, (G) (H) Distribution of electric field intensity (background) and Poynting vector (white arrows) in Y-Z plane and X-Z plane (Scale bars represent 50 nm). 46

Figure 4. 5 (A) Schematic showing the steps involved in plasmonic patch-enhanced IL-6 fluoroimmunoassay implemented on a plastic bottom 96-well plate. Fluorescence map of (B) unenhanced IL-6 fluoroimmunoassay (C) AuNR-57nm (57×18 nm) enhanced, and (D) AuNR-130 nm (130×40 nm) enhanced IL-6 fluoroimmunoassay. Plot showing the IL-6 dose dose-response

curve of (E) conventional IL-6 fluoroimmunoassay (F) AuNR-57 nm (57×18 nm) enhanced, and (G) AuNR-130 nm (130×40 nm) enhanced IL-6 fluoroimmunoassay. 47

Figure 4. 6 Quantitative measurement of multiplexed microarray of 10 human cytokines using size optimized plasmonic patch. (A) Layout of the antibodies corresponding to the cytokines on the quantitative microarray. Each type of antibody is printed in quadruplicate on the glass substrate. (B) Fluorescence map of the 10-plex microarray under various analytes concentrations. Top: without adding plasmonic-patch. Bottom: with plasmonic-patch enhancement. (C) Limit-of-detection of each cytokine before and after addition of plasmonic-patch. Standard curves of IL-6 (D) before and (E) after applying plasmonic-patch. 48

Figure 5. 1 Plasmonic-fluor synthesis and material characterization. (A) Schematic illustration showing the structure of “plasmonic-fluor”, which consists of a plasmonically-active core (*e.g.* gold nanorod (AuNR)), a polymer shell as spacer layer, light emitters, and a universal biorecognition element (biotin). BSA is employed as a key design element to assemble all components into the functional nanoconstruct and to resist non-specific binding. (B) Working principle of plasmonic-fluor as an “add-on” biolabel to enhance the fluorescence intensity and consequent signal-to-noise ratio of fluorescence-based assays, without changing the existing assay workflow. (C) Zeta potential of AuNR, AuNR/MPTMS, AuNR/MPTMS/polysiloxane (AuNR/polymer), and the plasmonic-fluor-800CW (AuNR/polymer/BSA-biotin-800CW). Error bar represents s.d. (n=3 repeated tests). (D) AFM images showing the AuNR before and after coating with polymer. (E) Vis-NIR extinction spectra of AuNR, AuNR/polymer, and plasmonic-fluor, showing a progressive red shift in the LSPR wavelength after each step. (F) TEM images of bare AuNR and plasmonic-fluor-800CW. 67

Figure 5. 2 Plasmon-enhanced fluorescence and colloidal stability of plasmonic-fluors. (A) Excited state lifetime measurements of conventional fluor (BSA-biotin-800CW) and plasmonic-fluor-800CW (AuNR/polymer/BSA-biotin-800CW) showing a significant decrease in the lifetime of 800CW after adsorption on AuNR. (B) Fluorescence intensity of conventional fluor-800CW and plasmonic-fluor-800CW at their different molar concentrations. The difference in the slopes of two curves indicates that a single plasmonic-fluor-800CW is as bright as 6700 (± 900) fluorophores. Error bar represents s.d. (n=3 repeated tests). (C) Fluorescence intensity of 800CW-streptavidin followed by the specific binding of plasmonic-fluor-800CW through biotin-streptavidin interaction, showing an average of 1200 (±40)-fold increase in fluorescence intensity. Error bar represents s.d. (n=4 independent tests). Data statistically significant *P* value= 0.0044, ** *P* < 0.01 by two-tailed unpaired t-test with Welch's correction. (D) Left: LSPR wavelength of gold nanoparticles (AuNPs) and AuNRs with similar surface area. Plot also shows the absorption and emission spectra of 800CW. Right: Fluorescence enhancement factor upon binding of “off-resonant” AuNP-plasmonic-fluor-800CW and “on-resonant” AuNR-plasmonic-fluor-800CW to 800CW-streptavidin. Error bar represents s.d. (n≥3 independent tests). Data statistically significant *P* value= 0.0013, ** *P* < 0.01 by two-tailed unpaired t-test with Welch's correction. (E)

Fluorescence enhancement factor obtained using plasmonic-fluor-800CW with different polymer spacer thickness. Error bar represents s.d. (n=5 independent tests). **** $P < 0.0001$ and ** $P < 0.01$ by one-way ANOVA with Tukey's post test. (F) Left: plot showing the stability of plasmonic-fluor suspension stored at 4°C and reconstituted from lyophilized powder. Error bar represents s.d. (n=6 repeated tests). NS: not significant. $P \text{ value} > 0.9999$ by one-way ANOVA with Tukey's post test. Right: Photographs depicting the lyophilized powder of plasmonic-fluor before and after reconstitution..... 68

Figure 5. 3 Plasmonic-fluor enhanced fluorophore-linked immunosorbent assay (FLISA) and multiplexed bead-based immunoassay. (A) Schematic showing the concept of conventional FLISA (800CW) and plasmonic-fluor-800CW enhanced FLISA (p-FLISA), implemented in a standard 96-well plate. P-FLISA assay does not require any change in the routine workflow except adding the plasmonic-fluor as the new, last step. (B) Fluorescence intensity maps of human IL-6 FLISA and p-FLISA at various analyte concentrations. (C) Fluorescence intensity maps (with zoomed-in scale bar) of human IL-6 FLISA and p-FLISA and photograph of colorimetric signal of “gold standard” human IL-6 ELISA. Plots showing human IL-6 dose-dependent fluorescence intensity from (D) conventional FLISA and (E) p-FLISA. Compared to conventional FLISA, p-FLISA exhibits 4750-fold improvement in the limit-of-detection (LOD) and more than three-order-magnitude larger dynamic range. (F) Plot showing the standard curve of human IL-6 ELISA. Compared to ELISA, p-FLISA exhibited 189-fold lower LOD and more than two-order-magnitude larger dynamic range. (G) IL-6 concentrations in human serum samples (diluted by 10-fold) measured using p-FLISA. Error bars represent s.d. (n=3 repeated tests). (H) Schematic illustration showing the concept of using plasmonic-fluor-Cy3 to enhance the sensitivity of bead-based immunoassay (*e.g.*, Luminex assay). (I) TEM image of plasmonic-fluor-Cy3 utilizing AuNR@Ag as the plasmonic nanoantenna. (J) SEM and (K) fluorescence images of microbead(s) before and after being probed with plasmonic-fluor-Cy3. (L) Mouse IL-6 and (M) mouse TNF- α standard curves obtained before (left) and after (right) applying plasmonic-fluor-Cy3. All standard curves are performed independently on different days with different batches of plasmonic-fluors at least three times (data included in supporting information)..... 69

Figure 5. 4 Plasmonic-fluor enhanced high-throughput proteome profiler array. (A) Illustration showing the application of plasmonic-fluor-800CW to enhance the bioanalytical parameters of multiplexed proteome profiler for human kidney disease biomarkers implemented on a nitrocellulose membrane. (B) SEM image showing the uniform distribution of plasmonic-fluor-800CW (a few highlighted by the yellow circles) on and in subsurface regions of the nitrocellulose membrane. Fluorescence intensity map representing kidney disease protein biomarker profile of a kidney disease patient obtained (C, D) using conventional fluorophores (streptavidin-800CW) and (E) after the addition of plasmonic-fluor-800CW (note the difference in fluorescence intensity scale bar). Fluorescence intensity corresponding to the concentrations of various urinary biomarkers (F) before (typical assay using conventional fluorophore) and (G) after the addition of plasmonic-fluor-800CW. [+] indicates biomarkers detected only with plasmonic-fluor-800CW. (H) Photograph (acquired by mobile phone) showing the color change of the nitrocellulose

membrane with urine sample from kidney disease patient after the addition of plasmonic-fluor-800CW. (I) Histogram showing the optical intensity of the mobile phone acquired photograph corresponding to each analyte in the patient urine sample. All error bars represent s.d. (n=2 repeated tests). Experiment was repeated three times independently on different days with different batches of plasmonic-fluors and the data is shown in supporting information..... 70

Figure 5. 5 Plasmonic-fluor enhanced immunocytochemistry and flow cytometry. (A) Confocal laser scanning microscopy (CLSM) images of breast cancer cells (SK-BR-3) probed with conventional fluor (800CW, top row) and plasmonic-fluor-800CW (bottom row) at different concentrations of ErbB2 primary antibody. Scale bar represents 10 μ m. (B) Plot showing the fluorescence intensity of SK-BR-3 cells stained with conventional fluor and plasmonic-fluor-800CW. Error bars represent s.d. (over three different locations). (C) Schematic showing flow cytometry of ErbB2-stained SK-BR-3 cells probed by conventional fluor (680LT) followed with plasmonic-fluor-680LT. (D) Flow contour plot (with outliers) of fluorescence vs. forward scatter (vertically offset for clarity) of SK-BR-3 cells probed using different concentrations of ErbB2 primary antibody (Red: control group without adding primary antibody. Blue: cells treated with different dilutions of primary antibody). Cells are stained with conventional fluor (680LT, left plot) followed by the addition of plasmonic-fluor-680LT (right plot). (E) Fluorescence histogram of SK-BR-3 cells probed using conventional fluor (680LT) followed by the addition of plasmonic-fluor-680LT (at 10^3 -fold dilution of primary antibody). Error bars represent s.d. (n=3 independent tests). **** $p < 0.0001$ by two-tailed unpaired t-test with Welch's correction. (F) Histogram showing fluorescence for SK-BR-3 cells before (top) and after (bottom) the addition of plasmonic-fluor-680LT. Red: no primary antibody; blue: 2×10^5 -fold dilution; orange: 10^5 -fold dilution; light green: 10^4 -fold dilution; green: 10^3 -fold dilution; rose: 10^2 -fold dilution of the stock solution provided by the vendor. (G) Plot showing the mean fluorescence intensity obtained from flow cytometry at different primary antibody concentrations. Error bars represent s.d. (n=3 independent tests). All experiments were repeated three times independently on different days with different batches of plasmonic-fluors and the data is shown in supporting information..... 71

Figure 5. 6 Flow cytometry measurement of BMDC maturation maker probed by conventional fluor (680LT) and plasmonic-fluor-680LT. (A) Schematic illustration showing bone marrow derived dendritic cells (BMDCs) treated with the immuno-stimulant (lipopolysaccharide (LPS)). The small changes of maturation markers (CD80) expression after stimulation are detected by immunofluorescence staining followed by addition of plasmonic-fluor-680LT. Fluorescence intensity distribution corresponding to naïve (control) and LPS-stimulated BMDCs obtained using (B) conventional fluors (680LT) and (C) plasmonic-fluor-680LT. (D) Plot showing mean fluorescence intensity of BMDCs (corresponding to the expression level of CD80) after stimulation with different amounts of LPS. (E) Secretion levels of pro-inflammatory cytokines (TNF- α and IL-12), which confirmed the dose-dependent activation and maturation of BMDCs. Error bar represents s.d. (n=2 repeated tests). Experiment was repeated three times independently on different days with different batches of plasmonic-fluors and the data is shown in supporting information..... 73

Figure 6. 1 (A) TEM image showing the core-shell structure of Au nanorattles (AuNRT) employed as the nanotransducers in plasmonic biosensors (B) Vis-NIR extinction spectrum of aqueous suspension of AuNRT..... 88

Figure 6. 2 (A) Schematic illustration showing the concept of plasmonic biosensor based on artificial antibodies as biorecognition elements. The artificial antibody is realized on AuNRT by molecular imprinting using siloxane copolymer (B) Vis-NIR extinction spectra of the AuNRT along the molecular imprinting process (inset shows zoom-in spectra highlighting the LSPR shift) (C) Plot showing the LSPR shift of AuNRT with artificial antibody (artificial anti-hemoglobin) after exposure to various concentrations of hemoglobin. Results are the mean \pm SD (n=3)..... 89

Figure 6. 3 (A) Schematic illustration representing the fabrication of plasmonic biosensor based on natural antibodies as recognition elements (B) Vis-NIR extinction spectra showing the LSPR shift of AuNRT after conjugation with natural anti-hemoglobin antibody (inset reveals the red shift in the LSPR wavelength to be 6 nm) (C) LSPR shift of plasmonic biosensor based on natural antibodies (anti-hemoglobin antibody) upon exposure to various concentrations of hemoglobin. Results are the mean \pm SD (n=3). 90

Figure 6. 4 (A) Retained recognition ability of natural and artificial antibody-based biosensor stored at room temperature for different durations. (B) Retained recognition of artificial antibody-based biosensor, as determined by exposure to various concentrations of the analyte (hemoglobin) solution, after storage at room temperature for one week (C) Retained recognition ability of natural and artificial antibody-based biosensors stored for 1 day at various temperatures and (D) Retained recognition ability of natural and artificial antibody-based biosensors after exposure to a wide range of pH conditions. Results are the mean \pm SD (n=3). 91

Figure 6. 5 (A) Vis-NIR extinction spectra of the AuNRT exhibiting a progressive red shift in the LSPR wavelength upon modification with pATP and GA, immobilization of KIM-1 and copolymerization of the silane monomers, (B) LSPR shift of AuNRT after each step along the formation of the artificial antibodies, template removal and template rebinding (C) LSPR shift of KIM-1-imprinted AuNRT upon exposure to various concentrations of KIM-1 solutions (D) Retained recognition ability of KIM-1 imprinted artificial antibody biosensor after storage at room temperature for different durations (E) at various temperatures for 1 day and (F) after exposure to a wide range of pH conditions. Results are the mean \pm SD (n=3)..... 92

Figure 7. 1 TEM image of (A) Au@Ag nanocubes and (B) Au nanorattles. (C) Vis-NIR extinction spectra of aqueous suspension of Au@Ag nanocubes and Au nanorattles. Inset shows the photographs of the corresponding aqueous solutions (D) Schematic illustration of the chemical grafting of PEG chains to the siloxane copolymer surface (E) Schematic illustration showing the various steps involved in the formation and PEGylation of the artificial antibodies. 104

Figure 7. 2 (A) Extinction spectra of AuNRT before and after PEGylation of the siloxane copolymer surface before template extraction (Zoomed-in plot in the inset shows the ~2 nm red shift) (B) FTIR spectrum after PEGylation of the siloxane copolymer showing the characteristic bands corresponding to PEG. X-ray photoelectron spectra (C) before and (D) after PEGylation of the siloxane copolymer surface showing the dramatic increase in the C-O/C-C intensity ratio from 0.36 to 0.68 105

Figure 7. 3 (A) PEGylation of molecular imprinted polymer before template removal (i) schematic showing the PEGylated non-cavity regions (ii) LSPR shift of AuNRT after each step along the formation of the artificial antibodies, PEGylation, template removal and template rebinding (iii) Plot showing the LSPR shift for various concentrations of Hb (target biomarker) with and without PEGylation. (B) PEGylation of molecular imprinted polymer after template removal (i) schematic showing the PEGylated cavity and non-cavity regions (ii) LSPR shift of AuNRT after each step along the formation of the artificial antibodies, template removal, PEGylation, and template rebinding (iii) Plot showing the LSPR shift for various concentrations of Hb for artificial antibodies PEGylated before and after template removal (C) PEGylation of siloxane copolymer without template (i) schematic showing the PEGylated siloxane copolymer (ii) LSPR shift of AuNRT after each step along the formation of siloxane copolymer on AuNRT, PEGylation, and non-specific binding of proteins (iii) Plot showing the LSPR shift for various concentrations of Hb for PEGylated siloxane copolymer with and without recognition cavities..... 106

Figure 7. 4 (A) Efficiency of different blocking methods in resisting the non-specific adsorption of BSA (an interfering protein) on MIP (B) LSPR shift of PEGylated and non-PEGylated MIPs on AuNRT after exposure to various interfering proteins (blue and red column for PEGylated, no PEGylation, respectively) (C) LSPR shift vs. concentration of target (Hb) and interfering protein (HSA) depicting the excellent selectivity of the Hb-imprinted PEGylated artificial antibody (D) Improved selectivity of PEGylated plasmonic biosensor to target biomarker (Hb) from artificial urine spiked with Hb (1 µg/ml) and HSA (10 µg/ml). 107

Figure 8. 1 (A) Schematic illustration showing the steps involved in molecular imprinting of gold nanorods with different monomers. (B) TEM image of gold nanorods (scale bar is 50nm). (C) Vis-NIR extinction spectra of aqueous suspension of gold nanorods. Inset shows the histogram of long axis length of gold nanorods obtained from TEM images..... 121

Figure 8. 2 (A) (B) Surface enhanced Raman scattering spectra with different amorphous polymers on gold nanorods reveal the Raman bands corresponding to trimethoxyphenylsilane..... 122

Figure 8. 3 (A) (B) (C) Extinction spectra and corresponding LSPR shift corresponding to each step in the molecular imprinting process when detecting 5 µg/ml lysozyme. (A) spectra in aqueous media with step 1, black spectra; step 2, red spectra, step 3, blue spectra; and step 4, lavender spectra. (B) Spectra in air with step 4, black spectra, step 5, blue spectra and step 6, red spectra. (C) Summary of LSPR peak spectra shift at each step of the imprinting process. (D) Sensitivity of

MIP-AuNR nanosensor expressed by the shift of LSPR wavelength when detecting lysozyme at different concentrations with polymers of different compositions. (E) Specificity of the lysozyme imprinted artificial antibody compared with interference protein (HSA or BSA) at distinct concentrations with polymers of different compositions..... 123

Figure 8. 4 (A) Sensitivity of MIP-AuNR nanosensor expressed by the shift of LSPR wavelength when detecting PLIN2 at different concentrations with polymers of different compositions. (B) Specificity of the PLIN2 imprinted artificial antibody compared with interference protein (HSA or BSA) at distinct concentrations with polymers of different compositions. (C) Sensitivity of MIP-AuNR nanosensor expressed by the shift of LSPR wavelength when detecting hemoglobin at different concentrations with polymers of different compositions. (D) LSPR shift of interference proteins (HSA or BSA) on hemoglobin imprinted plasmonic artificial antibody with polymers of different compositions. 124

List of abbreviations

AFM	Atomic force microscopy
AuNPs	Gold nanoparticles
AuNRs	Gold nanorods
Au@Ag	Silver coated gold nanoparticles
AuNR@Ag	Silver coated gold nanorods
AuNRT	Gold nanorattles
FTIR	Fourier-transform infrared spectroscopy
NIR	Near infrared
PBS	Phosphate-buffered saline
PDMS	Polydimethylsiloxane
SEM	Scanning electron microscopy
SERS	Surface enhanced Raman scattering
TEM	Transmission electron microscopy
UV-vis	Ultraviolet-visible
XPS	X-ray photoelectron spectroscopy
MIP	Molecularly imprinted polymer

PDMS	Polydimethylsiloxane
LSPR	Localized surface plasmon resonance
TMPS	Trimethoxypropylsilane
APTMS	(3-aminopropyl) trimethoxysilane,
XPS	X-ray photoelectron spectroscopy
MIP	Molecularly imprinted polymer
PDMS	Polydimethylsiloxane
LSPR	Localized surface plasmon resonance
TMPS	Trimethoxypropylsilane
AKI	Acute kidney injury
CKD	Chronic kidney disease
KIM-1	Kidney injury molecule-1
NGAL	Neutrophil gelatinase-associated lipocalin
LOD	Limit-of-detection
BSA	Bovine serum albumin
ELISA	Enzyme-linked immunosorbent assay
FLISA	Fluorophore-linked immunosorbent assay

eGFR	Estimated glomerular filtration rate
PEF	Plasmon enhanced fluorescence
FDTD	Finite-difference time-domain
EM field	Electromagnetic field
IL-6	Interleukin 6
ISF	Interstitial fluid
LPS	Lipopolysaccharide
PE	Phycoerythrin
TNF- α	Tumor necrosis factor- α
ICC	Immunocytochemistry
IF	Immunofluorescence
CLSM	Confocal laser scanning microscopy
BMDCs	Bone marrow-derived dendritic cells
POC	Point-of-care
PEG	Polyethylene glycol
Hb	Hemoglobin
TMPHS	Trimethoxyphenylsilane

MEF	Metal enhanced fluorescence
SD	Standard deviation
Mb	Myoglobin

Acknowledgments

First and foremost, I would like to express my sincere gratitude to my advisor Prof. Srikanth Singamaneni, who gave tremendous support for my PhD study. Having chance to be one of his students is the luckiest thing during my life. His patience, guidance, and immense knowledge helped me to understand fundamental scientific aspects, think independently, and get so close to cutting-edge researches, which I have never imagined five years back. Always doing the best work and trying to contribute as much as we can is the most inspiring “knowledge” passed by him. Thanks for his mentoring! I would also like to thank Prof. Guy Genin, who keeps encouraging me to be brave and confident. I would like to thank my PhD committee Prof. Jeremiah Morrissey, Prof. Shantanu Chakrabartty, Prof. Guy Genin, and Prof. Rohan Mishra for their valuable time, insightful comments, and inputs on my research, which helps me to improve the work quality.

I would like to thank all the previous and current members of the soft nanomaterials lab: Dr. Limei Tian, Dr. Kengku Liu, Dr. Sirimuvva Tadepalli, Dr. Qisheng Jiang, Dr. Congzhou Wang, Dr. Rong Hu, Dr. Chao Liang, Dr. Bo Hu, Dr. Anushree Seth, Mr. Zheyu Wang, Ms. Sisi Cao, Mr. Hamed Gholami Derami, Mr. Rohit Gupta, Mr. Prashant Gupta, Ms. Priya Rathi, Ms. Ting Xu for preccious help, sleepless nights we were working together, and for all the joy we have had in the last five years, making our lab feel like home.

Most of all, I want to thank my parents. During the past years, time spent with them is mostly on cellphone. Thanks for their understanding and huge support. Their love, encourage, and passion, give me motivations and inspire me all the time.

Jingyi Luan

Washington University in St. Louis

May 2020

ABSTRACT OF THE DISSERTATION

Ultrasensitive Biodetection based on

Plasmonically-active Materials

by

Jingyi Luan

Doctor of Philosophy in Mechanical Engineering and Material science

Washington University in St. Louis, 2020

Professor Srikanth Singamaneni, Chair

A broad range of biomarkers continue to emerge as potentially important parameters for early detection of many pathological conditions.¹ A disease biomarker (e.g. protein, a fragment of a protein, DNA/RNA, or metabolites) is a ‘molecular signature’ of the physiological state of patient at specific time and is therefore extremely important for early and possibly pre-symptomatic diagnosis and accurate monitoring of therapeutic intervention. Relevant concentrations of biomarkers related to diseases such as cancer, heart disease, inflammation, and neurological disorders can range in many orders of magnitude from $\mu\text{g/ml}$ levels to sub-fg/ml, some of which possibly still remain unidentified due to the lack of simple and sensitive bioanalytical tools. Moreover, there is an unmet need for stable biosensors for point-of-care (POC) diagnostics to provide accessibility to patients in developing countries, remote areas, and other resource-limited settings.

In the first part of the thesis, we harness the localized surface plasmon resonance (LSPR) of plasmonically active materials (e.g. “plasmonic patch”, “plasmonic fluor”), and show that plasmon-

enhanced fluorescence can vastly improve the sensitivity of a broad variety of bioanalytical methods, such as fluorophore-linked immunosorbent assays (FLISA), multiplexed bead-based fluoroimmunoassay, protein arrays, immunocytochemistry/immunofluorescence (ICC/IF), and flow cytometry.

In the second part of thesis, we focus on the design of molecular recognition element at the interface between plasmonic nanostructures and target biomolecule. We have designed specific and sensitive plasmonic biosensors based on synthetic biorecognition elements (artificial antibodies), to realize specific, stable, and sensitive detection of multiple protein biomarkers. Various fundamental aspects related to the use of artificial antibodies such as specificity and stability have been systematically investigated.

Overall, we have realized ultrasensitive and stable biodetection platform based on plasmonically-active materials, which can be potentially deployed in point-of-care and resource-limited settings

Chapter 1: Research goals and objective

The overall goal of this research effort is to harness localized surface plasmon resonance (LSPR) of noble metal nanostructures to overcome the fundamental scientific and technological challenges associated with ultrasensitive biosensors for point-of-care (POC) and resource-limited settings (Figure 1). Towards this goal, we have pursued the following two main objectives: 1) realize ultrasensitive bioanalytical methods based on novel plasmonically-active material platforms; 2) understand interfacial interactions between a molecular imprint that serves as artificial biorecognition element and the corresponding target analyte for maximizing their binding affinity, and selectivity. Taken together, these advances propel plasmonic biosensors closer to POC and resource limited settings, such as rural clinics, developing countries, and eventually at patient's home. We have accomplished several specific technical tasks noted below to realize these objectives:

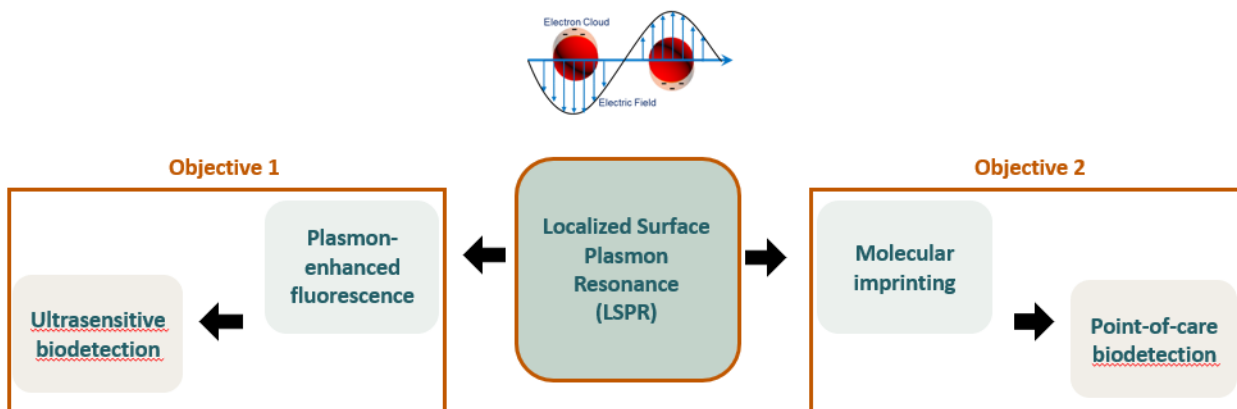


Figure 1. 1 Illustration outlining the overall research goal.

1.1 Objective 1

Introduce simple and broadly applicable plasmonically-active material platforms for ultrasensitive biodetection.

Task 1: Realize plasmonically-active elastomeric films that can readily serve as fluorescence enhancers in conventional fluoroimmunoassays.

Task 2: Understand the effects of optical properties of the plasmonic patches on the fluorescence enhancement efficiency.

Task 3: Design and realize an ultrabright fluorescent nanolabel based on plasmonic nanoantennas that readily improve the bioanalytical parameters of a wide range of fluorescence based analytical and imaging techniques.

1.2 Objective 2

Understand the sensitivity, specificity, and stability of artificial biorecognition elements realized through molecular imprinting on plasmonic nanostructures as a function of their surface/interfacial properties and composition.

Task 1: Compare the stability of plasmonic biosensor based on artificial antibody and natural antibody.

Task 2: Design and develop a surface PEGylation method of artificial antibody to improve the selectivity of the plasmonic biosensor.

Task 3: Understand the role of aromatic interactions in the biorecognition capabilities of artificial antibody based plasmonic biosensor.

Chapter 2: Background and motivation

2.1 Localized Surface Plasmon Resonance (LSPR)

Localized surface plasmon resonance (LSPR) occurs when the dimensions of a metallic nanostructure are less than the wavelength of incident light, leading to collective but non-propagating oscillations of surface electrons in the metallic nanostructure.²⁻³ The extremely intense and highly confined electromagnetic fields induced by the LSPR can significantly influence optical processes such as fluorescence, Raman scattering and infrared absorption, resulting in plasmon-enhanced fluorescence (PEF),⁴ surface-enhanced Raman scattering (SERS),⁵ and surface-enhanced infrared absorption spectroscopy (SEIAS).⁶ LSPR of metal nanostructure is highly sensitive to numerous factors such as composition, size, shape, surrounding dielectric medium, and proximity to other nanostructures.⁷⁻¹⁰ Size and shape dependence provides us with a wide spectral tunability along the whole visible and NIR spectrum, which is extremely useful to optimize surface-enhanced effects (*e.g.* plasmon-enhanced fluorescence (PEF), surface-enhanced Raman scattering (SERS)), photothermal effect and also to maximize the biosensing response of the nanostructures. On the other hand, the high sensitivity of the refractive index of the surrounding medium provides the basis for label-free plasmonic biosensors.^{3, 11-12} Local refractive index changes such as those induced by biomolecular interactions at the surface of the nanostructures can be monitored via the LSPR peak shift. LSPR of metal nanostructures has been shown to be sensitive enough to differentiate inert gases with refractive index contrast (δn) on the order of 3×10^{-4} , probe the conformational changes of biomacromolecules, detect single biomolecule binding events, monitor the kinetics of catalytic activity of single nanoparticles, and even optically detect single electron.¹³⁻¹⁶ Detection of various biomolecules such as proteins and DNA,¹⁷⁻¹⁹ have been demonstrated in the

past few years making the transduction platform promising for the development of simple, highly sensitive, label-free, and cost-effective diagnostics.

2.2 Plasmon-enhanced fluorescence

The use of fluorescent molecules is currently the most common labelling technique in biosensing and bioimaging. Fluorescence-based techniques have radically transformed biology and life sciences by unravelling the genomic, transcriptomic, and proteomic signatures of disease development, progression, and response to therapy.²⁰⁻²² Such approaches have seen widespread use in clinical practice but a plateau in the technology has been reached. Issues faced by fluorescent molecules are low intensities and photo stability, especially in the case of near infrared fluorophores, which need to be overcome. Amplification of light from fluorophores by coupling to metal nanostructures is a promising strategy for significantly improving the detection sensitivity and image enhancement and hence maximizing the potential of fluorescence based technologies in bio-applications.

Plasmonics has been recognized as a simple and highly effective approach for enhancing fluorescence. Enhancement of the emission of fluorophores in close proximity to plasmonic nanostructures is attributed to the enhanced electromagnetic field (local excitation field) at the surface of the plasmonic nanostructures and the decrease in the fluorescence lifetime due to the coupling between the excited fluorophores and the surface plasmons of the nanostructures.^{9, 23-31} During the past decade a number of existing and novel nanoparticles and structures have appeared in the literature designed to improve both the fluorescence intensity and photo stability of fluorophores through MEF. To date, various plasmonic substrates, such as periodic gold arrays³²⁻³³ and metal nanoislands,²⁶⁻²⁹ have been shown to give rise to strong fluorescence enhancement.

2.3 Label-free plasmonic biological sensors based on synthetic biorecognition element (artificial antibody).

Antibody–antigen interactions form the basis for current LSPR-based bioassays. Although natural receptors (e.g., monoclonal antibodies) have excellent molecular recognition capabilities, their biological origin imposes several inherent limitations, such as (i) limited pH and temperature stability; (ii) loss of conformation and recognition functionality in nonaqueous media; (iii) high cost associated with raising and harvesting natural antibodies; and (iv) poor compatibility with micro and nanofabrication processes for efficient integration with various transduction platforms. These issues impose severe challenges in the translation of a number of label-free plasmonic biosensing platforms to point-of-care and resource-limited settings.

Synthetic biorecognition elements or artificial antibodies based on molecular imprinting, which exhibit remarkable stability over a wide range of conditions (e.g., pH, temperature, solvent) are an attractive alternative to natural receptors. Artificial antibodies based on molecular imprinting are produced by creating “binding or recognition sites” in a polymer network using target (bio)molecules as templates. The binding sites are achieved by (co)polymerizing and cross-linking functional monomers around the template species. The template is subsequently removed by cleaving a predesigned reversible bond between the biomolecular template and the substrate. Upon removal of the template species, the polymer is left with cavities (i.e., binding sites), which are complementary in size, shape, and chemical functionality to the template species. The imprinted binding sites can then be accessed by target analytes with the same size, shape, and chemical functionality as the template species. Recently, we have demonstrated plasmonic biosensors based on artificial antibodies using gold nanorods and nanocages as plasmonic nanotransducers.³⁴⁻³⁵ These previous

studies from our group has shown the feasibility of combining plasmonic biosensors with artificial antibody to achieve label-free detection of disease biomarkers.

Chapter 3: Add-on plasmonic patch as universal fluorescence enhancer

3.1 Introduction

Fluorescence probes and fluorometric approaches have been ubiquitously employed in biomedical research, not only as imaging tools for the visualization of the location and dynamics of cells and of various sub-cellular species and molecular interactions in cells and tissues but also as labels in fluoroimmunoassays for the detection and quantification of molecular biomarkers. Fluorescence-based techniques have radically transformed biology and life sciences by unravelling the genomic, transcriptomic, and proteomic signatures of disease development, progression, and response to therapy.²⁰⁻²² However, the occurrence of a “feeble signal” has been a persistent and recurring problem in the battery of detection and imaging techniques that rely on fluorescence. Overcoming this fundamental challenge without the use of specialized reagents, equipment, or significant modifications to well-established procedures is a holy grail in the field of biomedical optics. For example, there is an urgent need for ultra-sensitive fluoroimmunoassays that can be broadly adopted by most biological and clinical laboratories for the detection of target biological species with low abundance.

Improving the signal-to-noise ratio of the assays without deviating from the existing assay protocols will also relax the stringent requirements of high sensitivity and bulky photodetectors, shorten the overall assay time, lower the cost of implementation, eliminate cross-laboratory cross-platform inconsistency, and potentially propel these technologies to use in point-of-care, in-field and resource-limited settings. Various techniques, including multiple-fluorophore labeling,³⁶ rolling cycle amplification,³⁷⁻³⁸ and photonic crystal enhancement,³⁹ have been introduced to improve the signal-to-noise ratio of fluorescence-based imaging and sensing techniques. Despite the improved

sensitivity, these technologies have not been widely adopted in research and clinical settings because most of them require significant modifications to the existing practices such as additional steps that significantly prolong the overall operation time, the need for specialized and expensive read-out systems, non-traditional data processing and analysis, or the use of temperature-sensitive reagents, which usually require tightly controlled transport and storage conditions.

Plasmonics has been recognized as a simple and highly effective approach for enhancing fluorescence. Enhancement of the emission of fluorophores in close proximity to plasmonic nanostructures is attributed to the enhanced electromagnetic field (local excitation field) at the surface of the plasmonic nanostructures and the decrease in the fluorescence lifetime due to the coupling between the excited fluorophores and the surface plasmons of the nanostructures.^{9, 23-31} To date, various plasmonic substrates, such as periodic gold arrays³²⁻³³ and metal nanoislands,²⁶⁻²⁹ have been shown to give rise to strong fluorescence enhancement. Although these plasmonic surfaces are highly attractive, their real-world application, for example, in fluoroimmunoassays, has been limited. The limited application of plasmon-enhanced fluoroimmunoassays in research and clinical settings is due to several factors: (i) Most of the existing techniques require the fluoroimmunoassay to be performed on pre-fabricated substrates, typically a rigid glass slide with metal nanostructures deposited on it, instead of standard or sometimes irreplaceable bioanalytical platforms (*e.g.*, 96-well plates and nitrocellulose membranes), which significantly limits the broad applicability of the techniques; more importantly, the requirement for the use of special substrates limits cross-platform and cross-laboratory consistency and seamless integration with widely employed bioanalytical procedures, representing a major bottleneck for the exploitation of conventional plasmon-enhanced fluorescence. (ii) Non-traditional bioconjugation procedures, complex interactions between biomolecules and metal nanostructures, and poor stability of biomolecules (*e.g.*, antibodies)

immobilized on metal surfaces not only complicate the assay procedures but also impose further technical challenges in their widespread application.⁴⁰ Thus, it is imperative to address these challenges to propel the plasmon-enhanced fluorescence techniques to practical applications.

Here, we introduce a simple, universal, and “add-on” fluorescence enhancement technique based on a “plasmonic patch” that can be applied on various fluorescent surfaces to achieve large and uniform fluorescence enhancement. To the best of our knowledge, this work represents the first demonstration of flexible plasmonics for fluorescence enhancement. In stark contrast with the existing plasmon enhancement techniques, which require significant modifications of the existing fluoroimmunoassay methods, the plasmonic patch approach demonstrated here requires virtually no change of the existing protocols except for the addition of the “patch” as the new, final step. Due to the enhanced electromagnetic field, the plasmonic patch can efficiently enhance the fluorescence by up to 100 times, leading to an ~300-fold increase in assay sensitivity. More importantly, the plasmonic patch exhibits excellent stability and low cost and entails the use of an extremely user-friendly protocol. This represents a “ready-to-use” technique that can be integrated with current biomedical research and clinical infrastructure to generate immediate results and impact.

3.2 Results and discussion

We introduce a novel material platform, namely, a “plasmonic patch”, for the enhancement of fluorescence on arbitrary surfaces. The fluorescence enhancement demonstrated here involves the transfer of a plasmonic patch, a transparent elastomeric film with adsorbed rationally designed metal nanostructures, onto a fluorescent surface to achieve conformal contact (Figure 1A). The plasmonic nanostructures on the elastomeric film come into close proximity to the fluorescent species on the surface, resulting in a large and uniform enhancement of the fluorescence.

3.2.1 Plasmonic patch fabrication and material characterization.

A thin polydimethylsiloxane (PDMS) layer (~ 30 μm thick) is employed as the “patch” material due to its high mechanical flexibility (elastic modulus ~ 1 MPa) (Figure 1B), optical transparency ($>95\%$ transmittance within the wavelength range of 400-900 nm),⁴¹ excellent processability, and low cost.⁴² The elastomeric nature of the PDMS enables conformal contact (down to the atomic level) of the patch with diverse surfaces, which is critical for fluorescence enhancement because the enhanced electromagnetic field of the plasmonic nanostructures is limited to the first few nanometers from the metal surface.⁴³ The plasmonic patch can be tailored for a specific fluorophore by maximizing the overlap between the localized surface plasmon resonance (LSPR) of the nanostructures and the optical absorption (excitation source) of the fluorophore to achieve the highest enhancement.⁴⁴⁻⁴⁵ As representative examples, we fabricated plasmonic patches using three distinct nanostructures: (i) gold core-silver shell nanocubes (Au@Ag nanocubes) with an LSPR wavelength of 490 nm (Au@Ag-490 henceforth, edge length ~ 48.5 nm) and gold nanorods (AuNRs) with a longitudinal LSPR wavelength of (ii) 670 nm (AuNR-670 henceforth, length ~ 112.2 nm, diameter ~ 54.5 nm) and (iii) 760 nm (AuNR-760 henceforth, length ~ 62.7 nm, diameter ~ 18.1 nm) (Figure 1C). SEM images indicate a highly uniform distribution of the plasmonic nanostructures on the PDMS film, with no sign of aggregation or patchiness (Figure 1D), ensuring nanoscale conformal contact between the plasmonic patch and the surface of interest. Extinction spectra obtained from the plasmonic patches further validate the absence of aggregates (Figure S1). The final density of the plasmonic nanostructures on the PDMS was determined to be $31/\mu\text{m}^2$ for Au@Ag-490, $21.4/\mu\text{m}^2$ for AuNR-670, and $169/\mu\text{m}^2$ for AuNR-760. The flexible plasmonic patches exhibit a distinct and uniform color corresponding to the LSPR wavelength of the

nanostructures (Figure 1E). The three plasmonic patches described above were designed for fluorescein isothiocyanate (FITC) (Au@Ag-490), 680LT (AuNR-670), and 800CW (AuNR-760), chosen in this study as representative fluorophores. Transfer of the corresponding plasmonic patches to silicon surfaces coated with FITC, 680LT, and 800CW resulted in a uniform enhancement of the fluorescence from these surfaces (Figure 1F). Additionally, the transfer process is easy, and its implementation does not require special training for users (Figure S2). The fluorescence intensity in the presence of a plasmonic patch was found to be nearly 50 times higher than that obtained from an unenhanced surface under identical illumination conditions (Figure S3). In addition to silicon, we applied plasmonic patches to glass, nitrocellulose, and polystyrene (a common material for microtiter plates) surfaces, which are extensively employed in various fluorescence-based detection, quantitative sensing and imaging techniques. The excellent conformality of the plasmonic patch with all of the above materials resulted in large fluorescence enhancements of the dyes deposited on these surfaces. The intensity cross-section profiles obtained for these different materials demonstrate up to 80-fold enhancement in the fluorescence from the regions with the plasmonic patch (center) compared to unenhanced regions (periphery) (Figure S4).

3.2.2 Distance-dependent fluorescence enhancement and spacer layer.

It is known that the evanescent nature of the enhanced electromagnetic field at the surface of plasmonic nanostructures results in a highly distance-dependent enhancement of Raman scattering and fluorescence at the surface of the plasmonic nanostructures.⁴⁶⁻⁵⁰ When fluorophores are brought in direct contact (or in extremely close proximity) to plasmonic nanostructures, non-radiative energy transfer between the fluorophore and metal surface results in fluorescence quenching.⁵¹ On the other hand, an increase in the distance between the fluorophores and metal nanostructures re-

sults in a decrease in the enhancement due to the decay in the electromagnetic field from the surface of the nanostructures. Taken together, these effects mean that an optimal distance between the metal surface and fluorophore is critical to ensure the maximum enhancement.⁵² To achieve an optimal distance between the plasmonic nanostructures and fluorophores of interest, we employed a polysiloxane copolymer film formed on the surface of the plasmonic patch as a spacer layer (Figure 2A). Trimethoxypropylsilane (TMPS) and (3-aminopropyl) trimethoxysilane (APTMS), which are hydrolytically unstable, were copolymerized onto the plasmonic patch composed of AuNR-760. The two monomers underwent rapid hydrolysis and subsequent condensation, yielding an amorphous copolymer layer (Figure S5A).³⁴ An increase in the thickness of the spacer layer resulted in a gradual redshift of the longitudinal LSPR wavelength of AuNRs due to the increase in the refractive index of the medium surrounding the nanostructures (Figure S5B). We estimated the thickness of the spacer layer for the different TMPS amounts used during the polymerization (see Supporting Information for an estimation of the spacer thickness, Figure S5C-I). With the increase in the spacer layer thickness, we observed a steep increase in the fluorescence enhancement efficacy of 800CW followed by a relatively shallow reduction (Figure 2B, C). Atomic force microscopy (AFM) images depicted the morphology change of the plasmonic patch after the formation of the polysiloxane layer, which further confirmed the uniform deposition of the polymer spacer onto the AuNRs (Figure 2D). Plasmonic patches with the optimal spacer layer were used in the subsequent studies (described below).

3.2.3 Patterned plasmonic patch and localized fluorescence enhancement.

To demonstrate that the fluorescence enhancement induced by the “plasmonic patch” is localized to areas that are in conformal contact with the plasmonic patch, we employed a patterned patch layer with well-defined surface-relief structures on both micro- and macroscales. Transfer of the

patterned plasmonic patch onto a silicon substrate with uniformly adsorbed fluorophores resulted in conformal contact between the raised regions of the plasmonic patch and the substrate, while the surface relief regions remained far from the substrate (Figure 3A). As representative microscale structures, we employed plasmonic patches with a stripe array and a square lattice composed of Au@Ag-490 (Figure 3B, C). Insets of the SEM images depict the uniform adsorption of the nanostructures in both the elevated and surface-relief regions of the microstructured PDMS surface. AFM images reveal that the depth of the ridges in the stripe array are ~400 nm (Figure 3D). The square lattice array, on the other hand, is composed of three regions with distinct heights (pores, struts and nodes with increasing height) (Figure 3E). After the transfer of the patterned plasmonic patch onto silicon coated with FITC, the plasmonic patch exhibited selective enhancement of fluorescence from the raised regions of the plasmonic patch that came into conformal contact with the silicon surface. In the case of the plasmonic patch with the stripe pattern, the fluorescence image shows arrays of bright and dark stripes corresponding to the raised and surface-relief regions of the plasmonic patch, respectively (Figure 3F). Notably, the fluorescence enhancement in the case of the square array is confined to nodes, indicating that the struts and pores are too far from the surface to enhance the fluorescence (Figure 3G). In addition to micropatterns, we also fabricated a plasmonic patch with a feature size ranging from tens of microns to millimeters (Figure 3H, I and Figure S6). Transfer of plasmonic patches engraved with a square array of circular holes (with Au@Ag-490) and the “Washington University in St. Louis” logo (with AuNR-760) resulted in fluorescence images with a square array of dark circles and the logo with high image quality and feature fidelity (Figure 3H, I).

3.2.4 Plasmonic patch-enhanced fluoroimmunoassays.

We now turn our attention to the application of the plasmonic patch as a universal fluorescence enhancer in fluoroimmunoassays. A typical sandwich fluoroimmunoassay involves the following major steps: (i) capture of the target antigen by an immobilized antibody; (ii) binding of the biotinylated detection antibody to the captured antigen; and (iii) binding of fluorescently labeled streptavidin (Figure 4A). We hypothesize that the addition of a plasmonic patch after the last step (*i.e.*, binding of the fluorescently labeled streptavidin) can result in a large enhancement of the fluorescence intensity and significantly improve the limit-of-detection (LOD given by the average fluorescence intensity at zero concentration (blank) plus three times its standard deviation). To verify this hypothesis, we implemented a fluoroimmunoassay in a heterogeneous, solid-phase format by using a 96-well microtiter plate as a sampling platform, a standard assay format extensively employed in bioanalytical research and clinical diagnostics (Figure 4A).

We used two early stage biomarkers for acute kidney injury (AKI) and chronic kidney disease (CKD), namely, kidney injury molecule-1 (KIM-1) and neutrophil gelatinase-associated lipocalin (NGAL), as representative examples for probing the efficacy of the plasmonic patch in improving the bioanalytical parameters of fluoroimmunoassays.⁵³⁻⁵⁵ The assays were first implemented on a 96-well plate with a glass bottom. In the KIM-1 immunoassay, we used 680LT as the fluorescence tag and the plasmonic patch based on AuNR-670 as the enhancer. To probe the enhancement in the sensitivity and LOD, serial dilutions of KIM-1 of known concentrations (5 ng/ml to 500 fg/ml) in phosphate-buffered saline (PBS) with 1% bovine serum albumin (BSA) were employed as standards. Fluorescence images obtained after the application of the plasmonic patch revealed a strong enhancement in the fluorescent intensity compared to that obtained prior to the application of the plasmonic patch (Figure 4B). The fluorescence signal from the unenhanced (pristine) spots

was detectable only for the two highest concentrations (5 and 0.5 ng/ml) (Figure 4B, left and middle images). On the other hand, the fluorescence signal with the plasmonic patch could be detected down to 500 fg/ml (Figure 4B). The concentration-response plot revealed a 36-fold enhancement in the fluorescence intensity with the plasmonic patch compared to the unenhanced signal (Figure 4C). The LOD (3σ) values of the unenhanced and plasmon-enhanced KIM-1 assays were determined to be 140 pg/ml and 0.5 pg/ml, respectively, representing a 280-fold improvement in the LOD. Consequently, the enhanced KIM-1 assay exhibited a three orders of magnitude higher dynamic range compared to the unenhanced assay. The fluorescence signal after the application of the plasmonic patch exhibited excellent stability even after four weeks of storage under dark conditions (Figure S7). To demonstrate the broad applicability of the plasmon-enhanced fluoroimmunoassay, we used NGAL as another representative example. 800CW (conjugated to streptavidin) was used as the fluorescence label to demonstrate the tunability of the plasmonic patch. Following the transfer of the plasmonic patch, we observed a fluorescence enhancement of up to 103 times and an ~100-fold lower LOD compared to the unenhanced NGAL assay (Figure 4D and 4E). Consistently, the NGAL assay implemented on a common 96-well plate with a plastic bottom (instead of a glass bottom) also exhibited a strong fluorescence enhancement in the presence of the plasmonic patch (Figure S8), further validating the plasmonic patch as a substrate material-agnostic technology.

Enzyme-linked immunosorbent assay (ELISA) is widely employed in clinical and research settings and is often considered as the “gold standard” for protein biomarker detection and quantification. We compared the performance of the plasmon-enhanced fluoroimmunoassay with ELISA using KIM-1 as a representative biomarker. In addition to simplifying the overall assay procedure (*e.g.*,

obviating the need for enzymatic amplification), the LOD of the plasmon-enhanced fluoroimmunoassay was found to be ~30 times lower (0.5 pg/ml) than that of ELISA (15.6 pg/ml) (Figures 4C and S9). Notably, the dynamic range of the enhanced fluoroimmunoassay spanned five log orders of KIM-1 concentration, while the dynamic range of ELISA was only 2.5 log orders of KIM-1 concentration (Figures 4C and S9). The higher dynamic range of the enhanced fluoroimmunoassay is expected to enable the quantification of a wider range of biomarker concentrations in human urine samples, as described below.

Following the successful demonstration of the plasmonic patch-enhanced fluoroimmunoassay, we set out to analyze urine samples from patients and self-described healthy volunteers in order to determine the concentrations of KIM-1 and NGAL. To demonstrate the wide applicability of the technique, we implemented KIM-1 and NGAL fluoroimmunoassays on glass and plastic bottom 96-well plates, respectively. The urine samples were diluted with 1% BSA in PBS to minimize the confounding from inter-individual differences in urine pH and solute content. For KIM-1 (10-fold dilution) and NGAL (40-fold dilution), the plasmon-enhanced fluoroimmunoassay exhibited a dramatic increase in the fluorescence compared to the unenhanced fluoroimmunoassay (Figure 5A (KIM-1) and 5B (NGAL)). The enhanced fluorescence signal was used to quantify the biomarker concentration in the urine samples. We also used standard ELISA to determine the KIM-1 and NGAL concentrations in the human urine samples. The concentrations of the biomarker in urine determined by the above three assays (unenhanced and enhanced fluoroimmunoassays and ELISA) are compared in Figure 5C (KIM-1) and 5D (NGAL). The unenhanced fluoroimmunoassay was not able to detect KIM-1 or NGAL in any of the human urine samples. In stark contrast, the plasmon-enhanced fluoroimmunoassay was able to quantify both KIM-1 and NGAL concentrations in all human urine samples, some of which were even lower than the LOD of ELISA. For

the samples that were quantifiable using both ELISA and enhanced fluoroimmunoassay, the concentration of the biomarker determined using the enhanced fluoroimmunoassay showed excellent agreement with that determined using “gold standard” ELISA for both KIM-1 ($r^2=0.934$) and NGAL ($r^2=0.998$) (Figure 5E and 5F).

The biomarker concentrations in the human urine samples were determined by accounting for the dilutions in each of the assays, and the results are presented in Figure 5G. The estimated glomerular filtration rate (eGFR) determined from the serum creatinine concentration is the standard metric of kidney function.⁵⁶ eGFR decreases to below 90 (ml/min) as the kidney function declines.⁵⁶ The two urine biomarkers can provide diagnostic kidney disease information beyond that of eGFR. NGAL and KIM-1 concentrations in healthy humans are <20 ng/ml and <1 ng/ml, respectively. In acute kidney injury, NGAL exceeds 100 ng/ml.^{55, 57-58} Taking patients #24 and #37 as examples, while their eGFR levels (153 ml/min and 90 ml/min) are within the normal range, their NGAL and KIM-1 concentrations were significantly higher, indicating a high risk of chronic kidney disease (#24) and acute kidney injury (#37). Notably, for diabetics, the eGFR levels tend to increase to 150 ml/min followed by a significant decrease (down to 30 ml/min) with time. The higher eGFRs of patients #24 and #37 and their slightly elevated KIM-1 and NGAL concentrations may be due to the patients being diabetic, which is a risk factor for chronic kidney disease (Figure 5G).⁵⁹

3.2.5 Application of a plasmonic patch on a protein microarray. To demonstrate the applicability of the plasmonic patch in enhancing the sensitivity of immuno-microarrays, we customized a microarray of antibodies to the biomarkers of kidney injury as a representative example to test the performance of the plasmonic patch in a multiplexed and high-throughput biosensing platform (Figure 6A). This microarray is composed of eight capture antibodies corresponding to the AKI and CKD protein biomarkers, printed in duplicate on a glass slide isolated by a plastic frame with

a feature diameter of 150 μm . Biotinylated IgGs of three gradient concentrations were printed in duplicate as positive controls (Figure 6B, left schematic showing the protein layout on the microarray). Six human urine samples were diluted 2-fold using a blocking buffer and added to each sub-well on the glass slide. Subsequently, the captured biomarker proteins were exposed to a biotinylated detection antibody cocktail followed by exposure to 800CW-labeled streptavidin. The conventional microarray procedure ends at this step, at which point the biomarker concentration is quantified by analyzing the localized fluorescent signal on the respective antibody spot. The enhanced assay demonstrated here involves the addition of a $1 \times 1 \text{ cm}^2$ plasmonic patch modified with AuNR-760 on top of each array (see Methods for details).

The fluorescence map from a single sample (patient #81, Figure 6B, right panels) is informative. In addition to the large enhancement of the weak fluorescence of albumin, cystatin C, β_2 microglobulin (Beta 2M), and NGAL in the unenhanced microarray, the plasmonic patch enabled the detection and quantification of analytes that could not be detected at all by the conventional method (red boxes in Figure 6B). These new analytes are tissue inhibitor of metalloproteinases 2 (TIMP-2), KIM-1, and insulin-like growth factor-binding protein 7 (IGFBP-7), which are specific and important biomarkers for early detection of acute kidney injury.^{47, 60} In addition to patient #81, the plasmonic patch consistently enhanced the fluorescence signals of the microarray exposed to urine samples from patients #29, #37, and #67 and healthy volunteers #M70 and #403 (Figure S10). Quantitative measurement of the antibody spot intensity from the urine of the six individuals showed 20- to 137-fold increase in the fluorescence of several analytes and the detection of other analytes enabled only by the enhancement from the plasmonic patch (Figure 6C, the [+] mark indicates that the biomarker is only detected with the plasmonic patch). Comparison between the

unenanced and plasmonic patch enhanced fluorescence heat maps from the six donors further revealed the high signal-to-noise ratio and a broadened dynamic range (Figure 6D).

3.3 Conclusions

Most previous plasmon-enhanced fluorescence assays rely on engineering the substrate to be plasmonically active through either the deposition of metal islands or adsorption of plasmonic nanostructures. These methods naturally require the utilization of special surfaces and possibly significant alterations of the read-out devices and the bioassay protocol. Here, we demonstrated an alternative method in which the enhancement is achieved by a simple transfer of a plasmonic patch onto a surface with fluorescent species. This novel approach not only obviates the need for special substrates or tedious bioconjugation procedures but also offers excellent tunability of the plasmonic properties (over the entire visible and NIR wavelength range) and distance between the metal surface and fluorophores. Notably, the magnitude of the fluorescence enhancement obtained using plasmonic substrates described in the past is highly dependent on the size of the capture antibody, antigen, and detection antibody that exist between the plasmonic nanostructures on the substrate and the fluorophores. The enhancement is therefore dictated by the preset “biological spacer”, leaving little control over the key design parameter for maximum enhancement, namely, the spacer layer thickness. By contrast, as an “add-on-top” layer, the plasmonic patch demonstrated here enables complete control over the distance between the plasmonic nanoantennas and fluorescent species. The facile control of the spacer thickness ensures the highest fluorescence enhancement despite the variations in the immunofluorescent assays, which is especially important in multiplexed platforms.

We also demonstrated the application of this platform technology in enhancing the bioanalytical parameters (sensitivity, LOD, and dynamic range) of fluoroimmunoassays implemented in a standard 96-microplate format and an antibody microarray. The plasmonic patch consistently resulted in a more than two orders of magnitude fluorescence intensity enhancement, leading to an ~300-fold lower LOD and a three orders of magnitude higher dynamic range. The improvement in the bioanalytical parameters was found to be consistent across different assay formats, target biomarkers, and fluorophores. Significantly, this method can be implemented with existing bioassays without any modification of the standard operating procedures, additional operational training, or modification of the read-out devices. As a part of the rigorous validation of this technology, we analyzed urine samples from patients and healthy volunteers. Unlike the unenhanced fluoroimmunoassay and ELISA, the plasmon-enhanced fluoroimmunoassay enabled the detection and quantification of low concentration biomarkers from all patients and healthy volunteers. The added sensitivity of the plasmon-enhanced assay enables facile quantification of the biomarkers with low abundance and provides physiological and pathological information that is often missed by the conventional immunoassays.

Multiplexed microarrays based on fluorescence are extensively employed in expression profiling, drug-target binding assays, and high-throughput proteomics.⁶¹⁻⁶² Compared to a singlex platform, such as ELISA, the technique presented here allows researchers and clinicians to examine a large number of biomarkers in parallel to achieve patient stratification and monitoring of multifactorial diseases with a limited sample volume, thereby minimizing the assay cost and time for the performance of multiple individual biomarker assays. Moreover, high-throughput profiling of the biomarkers enables personalized medicine with holistic, molecular fingerprinting of diseases, ac-

commodating greater diagnostic resolution between closely related disease phenotypes.⁶³ The sensitivity and specificity for the diagnosis of kidney disease have been proven to be significantly greater when combining the urinary levels of multiple biomarkers compared to the use of individual biomarkers.⁵⁵ However, despite the availability of various commercialized products, this multiplexed methodology suffers from inferior sensitivity and relatively high LOD compared to ELISA, which hinders its widespread application.

The plasmonic patch demonstrated here overcomes the abovementioned challenges and provides a path forward for broad application of multiplexed microarrays. We have demonstrated the application of the plasmonic patch in the multiplexed detection of a panel of biomarkers for kidney diseases. Our results suggest that the plasmonic patch could significantly enhance the ability to elucidate low-level kidney function parameters (biomarkers) to provide holistic kidney disease information. Notably, the better performance of the multiplexed microarray originates from the extremely simple “patch transfer” process, which does not alter the established process flow of immuno-microarrays. Additionally, this technique represents an inexpensive approach for the enhancement of fluorescence, and the cost for one piece of plasmonic film ($1 \times 1 \text{ cm}^2$) was estimated to be approximately \$0.05. We expect that this easily deployed technique could be seamlessly applied to a broad range of multiplexed platforms in diagnostics, proteomics, and genetics to address the unmet need for a greater signal intensity.

Our work here has primarily focused on the introduction of the plasmonic patch concept and on demonstrating its application in the enhancement of the bioanalytical parameters of fluoroimmunoassays implemented in microtiter plates and microarrays. However, it is important to note that this technique has broad implications in bioimaging, blotting, histology, and virtually any other appli-

cation involving fluorescence. Due to the minimal perturbation of the standard materials and procedures, this novel technique can be readily adapted to a number of different fluorescence-based technologies to alleviate the waste of resources arising from facility update, reduce the assay cost and time, eliminate cross-platform inconsistency, and potentially propel these technologies to use in point-of-care, in-field and resource-limited settings.

3.4 Materials and Methods

Fabrication of a plasmonic patch: Sylgard 186 (Dow Corning) polydimethylsiloxane (PDMS) elastomer was mixed at a 10:1 (base to curing agent) ratio. The prepolymer was spin-coated at 3000 rpm for 30 seconds on a polystyrene dish with a diameter of 3.5 cm. PDMS was then cured at 70 °C for 15 hours. Once cured, PDMS was treated with oxygen plasma for 3 mins and subsequently immersed into 0.2% aqueous poly(styrene sulfonate) (PSS) solution for 20 mins. PSS treatment gave rise to a negative charge on the surface of the PDMS film, facilitating the absorption of positively charged plasmonic nanoparticles through electrostatic interactions. Plasmonic nanoparticle solution was centrifuged and redispersed into a specific volume of nanopure water (for details, please see the supporting information). PSS-treated PDMS was incubated with the plasmonic nanoparticle solution for 15 hours in dark conditions. Subsequently, PDMS was rinsed with nanopure water and blow dried with nitrogen, leaving a surface with uniformly adsorbed plasmonic nanoparticles.

Polymer spacer on a plasmonic patch: Eight microliters of (3-Aminopropyl)trimethoxysilane (APTMS) and the desired amount of trimethoxypropylsilane (TMPS (0-8 μ l)) (for details, please see the supporting information) were added to 3 ml of phosphate-buffered saline (1X PBS). The plasmonic patch was incubated in the above solution for 2 hours. After 2 hours, the plasmonic patch was rinsed with PBS and nanopure water followed by blow drying with nitrogen gas.

Fluorescence-linked immunosorbent assay with a plasmonic patch: Fluorescence-linked immunosorbent assay was first implemented using 96-well plates with a glass bottom (Cellvis). The glass surface of each well was treated to achieve aldehyde functionality. The subsequent procedures were identical to those of ELISA (R&D systems (DY1750B, DY1757)) until the streptavidin binding step. Instead of HRP-labeled streptavidin, 100 μ l of dye-labeled streptavidin (800CW or 680LT (LICOR)) was diluted to the final concentration of 50 ng/ml using a reagent diluent and added to each well, followed by a 20-min incubation. A plasmonic patch was subsequently transferred to each well of the 96-well plate. The LICOR Odyssey CLx scanner was used to scan the 96-well plate. For the fluorescence-linked immunosorbent assay performed using plastic bottom 96-well plates, the procedure remained the same except for the omission of the surface modification steps.

Fluorescence enhancement on a protein microarray: Commercialized protein microarray chip kits were purchased from RayBiotech (Custom G-Series Antibody Array, AAX-CUST-G). Antibodies were printed on a glass slide with 4 subarrays available per slide. The slide was blocked by a blocking buffer (in kit) for 30 mins. Patients' and volunteers' urine samples were diluted twice using the blocking buffer, and 90 μ l of the diluted samples was added into each sub-well of the microarray chip, followed by a two-hour incubation at room temperature. The chip was then washed thoroughly with the wash buffer (in kit). Seventy microliters of biotin-conjugated anti-cytokines (in kit) was added to each subarray, and the chip was incubated at room temperature with gentle shaking. After two hours, the chip was washed, 70 μ l of streptavidin-800CW (100 ng/ml in blocking buffer, LICOR) was added, and the plate was incubated under dark conditions for 20 mins. The chip was washed thoroughly first with wash buffer and then with nanopure water and was then blow dried under nitrogen gas. The glass chip was scanned using a LICOR Odyssey

CLx scanner. A plasmonic patch was cut into $1 \times 1 \text{ cm}^2$ pieces and applied to the top of each subarray, followed by the attachment of a gold-coated reflective film with the same dimensions.

3.5 Figures

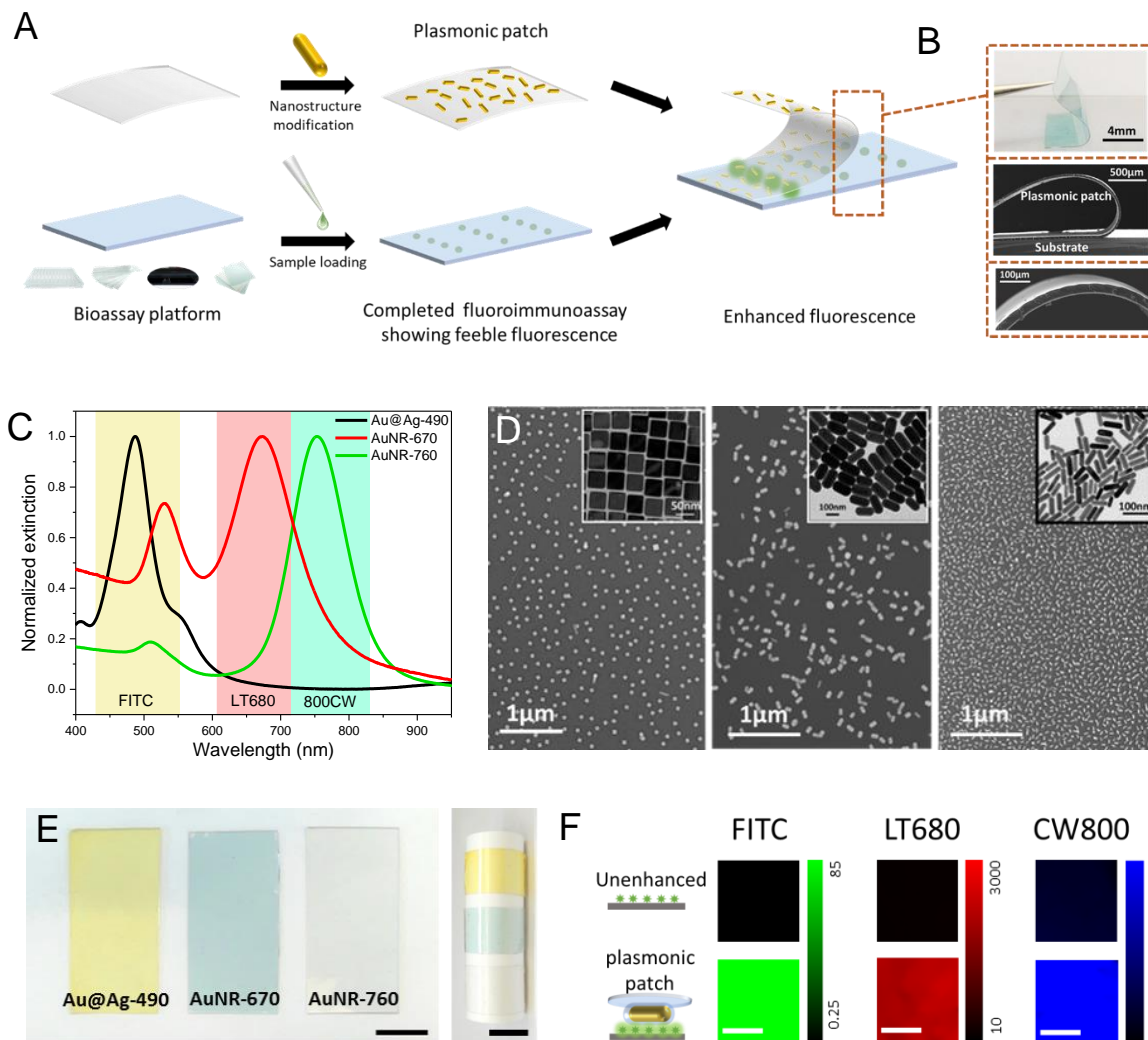


Figure 3. 1 (A) Schematic illustration of the fabrication of a plasmonic patch and its application in fluoroimmunoassays. A large enhancement in the fluorescence signal is simply achieved by the transfer of the plasmonic patch onto a surface with fluorescent species. This “add-on” step does not change the well-established procedures of current fluoroimmunoassays and can thus be seamlessly integrated with a variety of existing assays to significantly enhance their fluorescence. (B) Top: Photograph showing the transfer of a plasmonic patch to a planar surface. Middle: SEM image demonstrating the flexibility, as well as conformability to the substrate, of the plasmonic patch. Bottom: SEM image of the cross-section of the plasmonic patch showing an average thickness of $30 \mu\text{m}$. (C) Normalized extinction spectra of aqueous solutions of the three representative plasmonic nanostructures employed in this study (from left to right: Au@Ag-490, AuNR-670, and AuNR-760). The extinction bands of Au@Ag-490, AuNR-670, and AuNR-760 exhibit significant overlap with the absorption bands (excitation source) of FITC, 680LT, and 800CW, respectively.

(D) SEM images of the plasmonic patch surface revealing the uniform distribution of plasmonic nanostructures on PDMS (from left to right: Au@Ag-490, AuNR-670, and AuNR-760). Insets show representative TEM images of the corresponding plasmonic nanostructures. (E) Photograph of plasmonic patches modified with various nanostructures (left). The flexibility of the plasmonic patch is further demonstrated by rolling it around a cylindrical support (right). The scale bar represents 1 cm. (F) Fluorescence map of three fluorophores adsorbed on a silicon substrate in the presence and absence of a plasmonic patch (left scale bar represents 10 μm ; middle and right scale bars represent 1 mm).

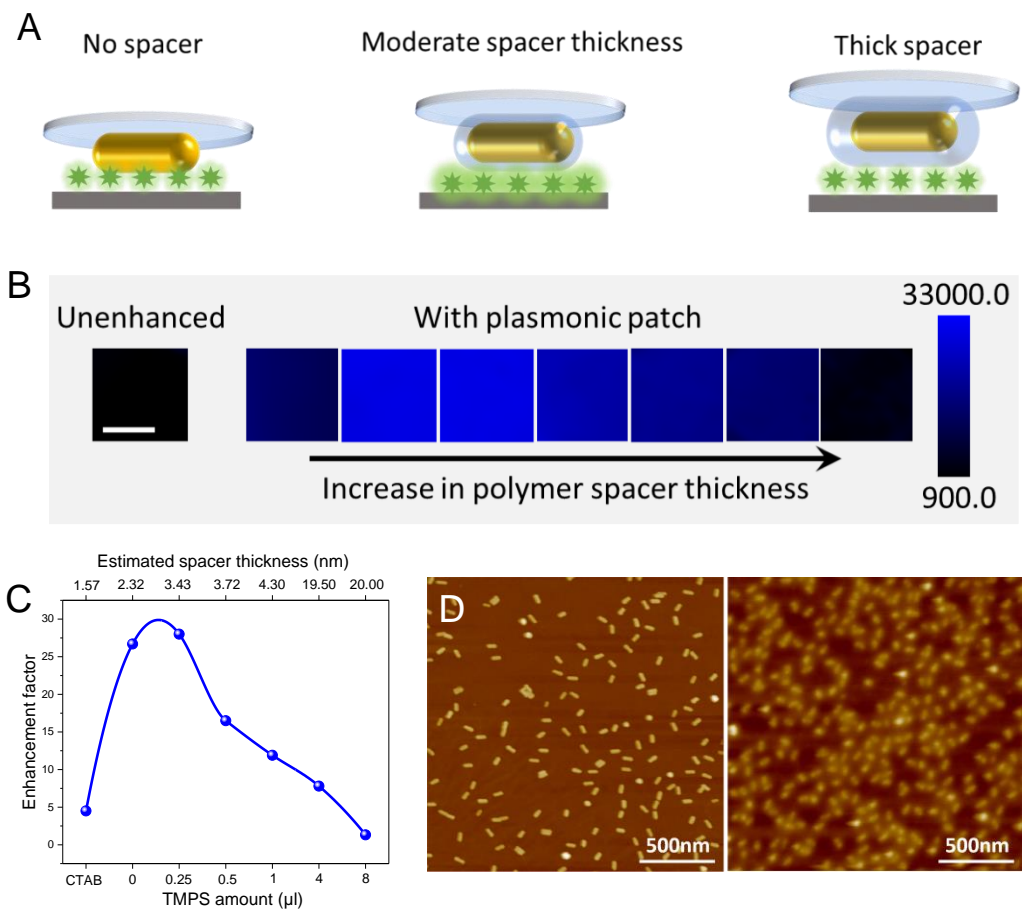


Figure 3. 2 (A) Schematic illustration showing a plasmonic patch with a polymer layer acting as a spacer between fluorophores and plasmonic nanostructures. The spacer thickness is optimized to achieve the maximum enhancement efficiency. (B) Fluorescence map of 800CW in the presence of plasmonic patches with increasing spacer layer thickness (TMPS and APTMS volume ratio is 0:0, 0:8, 0.25:8, 0.5:8, 1:8, 4:8, and 8:8 from left to right). (C) Fluorescence enhancement factor as a function of the spacer thickness (TMPS amount in the polymerization process). (D) AFM images of pristine Au nanorods (left) and Au nanorods with a polymer spacer (right) (TMPS and APTMS volume ratio of 4:8).

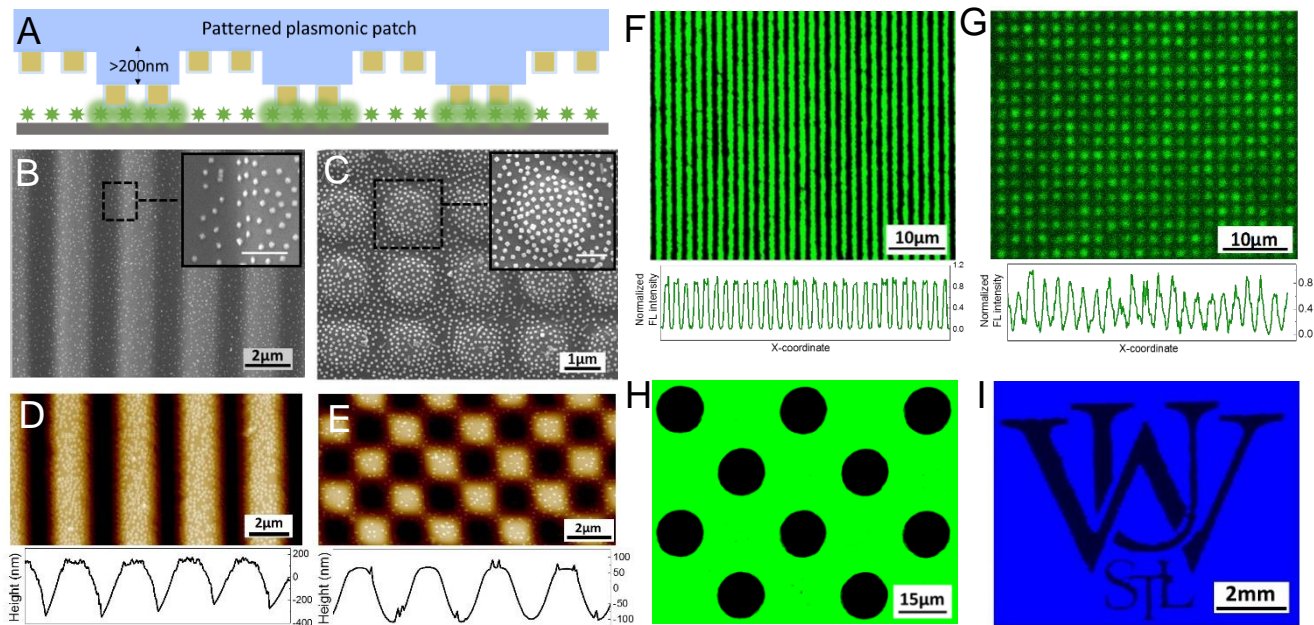


Figure 3. 3 (A) Schematic showing a patterned plasmonic patch, which selectively enhances the fluorescence in the regions of conformal contact. In all of the used patterns, the height of the surface-relief portions is greater than 200 nm. SEM image of a (B) stripe array and (C) square lattice PDMS with Au@Ag-490 adsorbed (insets show zoomed-in SEM images of the highlighted area revealing a uniform distribution of the plasmonic nanostructures on both elevated and surface-relief regions; inset scale bars represent 500 μm). AFM images of (D) stripe array (z scale: 430 nm) and (E) square lattice (z scale: 200 nm) plasmonic patches revealing the height profile of the surfaces. Fluorescence images of an FITC-coated silicon surface with (F) stripe array and (G) square lattice plasmonic patches on top. The plots below reveal the fluorescence intensity profiles. (H) Fluorescence map of FITC with a plasmonic patch (with Au@Ag-490 adsorbed) with circular pores. (I) Fluorescence image (800CW) of the “Washington University in St. Louis” logo obtained using a plasmonic patch (with AuNR-760 adsorbed) with an engraved logo.

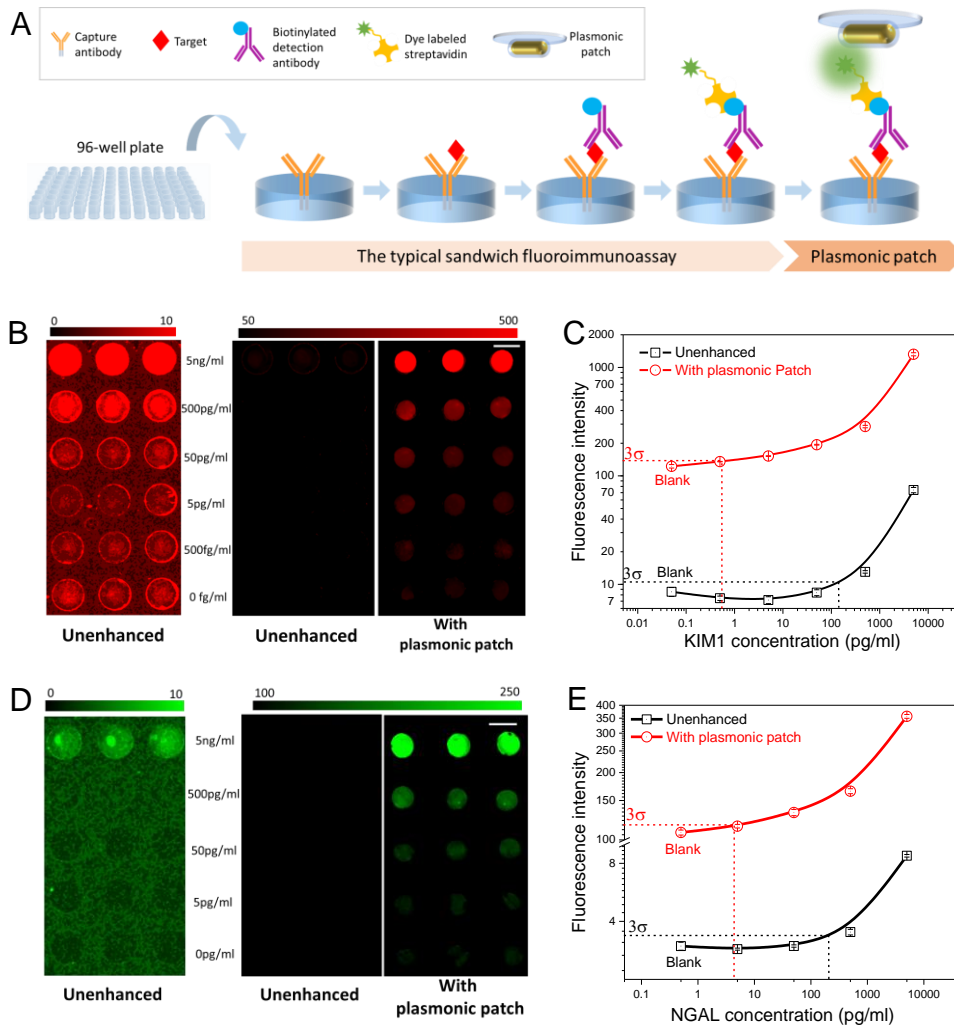


Figure 3. 4 (A) Schematic showing the concept of a plasmonic patch-enhanced fluoroimmunoassay implemented in a glass bottom 96-well plate, demonstrating the wide applicability of the plasmonic patch. Fluorescence intensity maps of fluoroimmunoassays corresponding to different concentrations of (B) KIM-1 and (D) NGAL, two early stage biomarkers for acute kidney injury (AKI) and chronic kidney disease (CKD) (left and middle images show the unenhanced assays corresponding to the different color scales shown in the figures; right image shows the plasmonic patch-enhanced assay revealing a large enhancement in the fluorescence signal as well as a broadened dynamic range compared to the unenhanced assay (scale bar represents 5 mm)). Plot showing the fluorescence intensities corresponding to different concentrations of (C) KIM-1 and (E) NGAL. The limits of detection identified in the plots show ~300-fold and ~100-fold improvement for KIM-1 and NGAL, respectively, compared to the unenhanced assay.

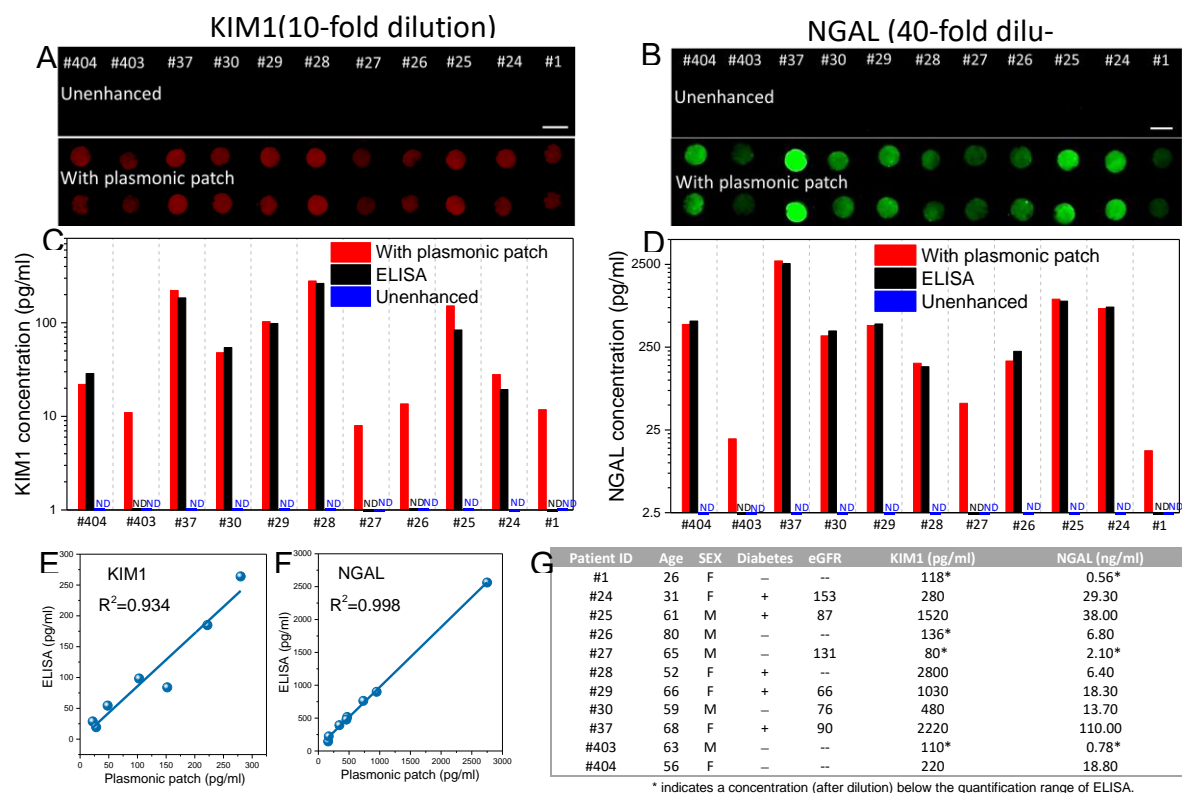


Figure 3. 5 Fluorescence intensity maps of (A) KIM-1 (10-fold dilution) and (B) NGAL (40-fold dilution) immunoassay for urine samples from eight patients (ID: #24, #25, #26, #27, #28, #29, #30, and #37) and three self-described healthy volunteers (ID: #1, #403, and #404). (Top: Unenhanced fluorescence map. Bottom: Plasmonic patch-enhanced fluorescence map. Scale bar=5 mm.) (C) KIM-1 and (D) NGAL concentrations in the urine samples (diluted 10-fold for KIM-1 and 40-fold for NGAL) as determined by unenhanced fluorescence assay, plasmon-enhanced fluorescence assay, and ELISA. Plot showing the correlation between the concentration of (E) KIM-1 and (F) NGAL determined using ELISA and plasmonic patch-enhanced fluorescence assay. (G) Table summarizing the age, sex, diabetic condition, estimated glomerular filtration rate (eGFR), and measured (by the plasmonic patch-enhanced method) urinary concentrations of KIM-1 and NGAL in urine samples from 11 patients or healthy volunteers.

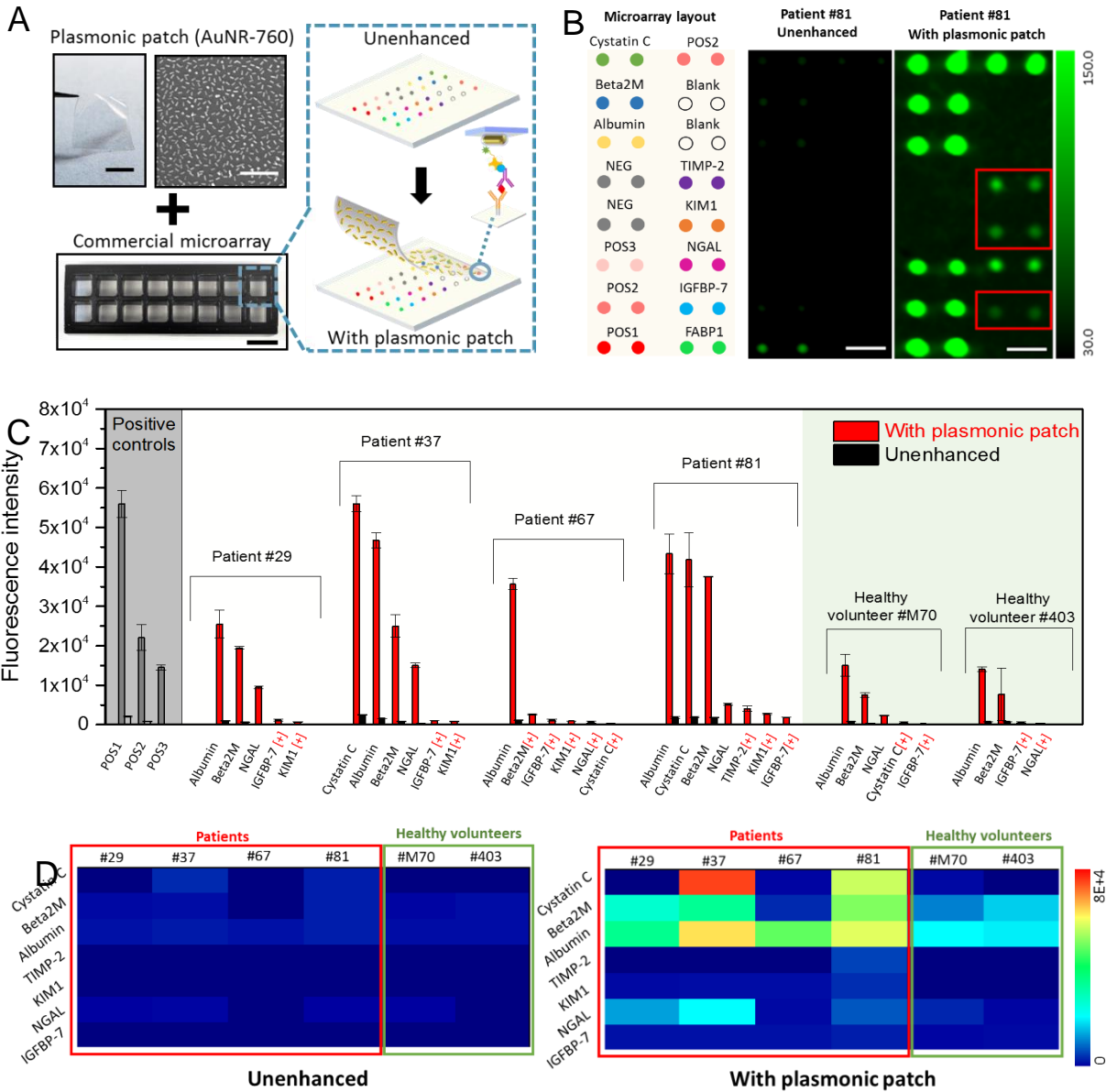


Figure 3. 6 (A) Illustration showing the application of a plasmonic patch to enhance the bioanalytical parameters of a protein microarray. Left: Photograph depicting the plasmonic patch employed for enhancing the fluorescence of a protein microarray (scale bar represents 5 mm), SEM image demonstrating the uniform absorption of AuNR-760 on the PDMS surface (scale bar represents 500 nm), and photograph of a commercial protein microarray substrate with 16 sub-wells for simultaneous analysis of multiple samples (scale bar represents 1 cm). Right: Schematic showing the concept of a plasmonic patch-enhanced microarray, which enables a highly sensitive profiling of eight AKI and CKD biomarkers simultaneously. (B) Left: Schematic showing the layout of antibodies printed on the bottom of each sub-well. Middle: Unenhanced fluorescence intensity map representing the AKI and CKD protein biomarker profile of patient #81. Right: Fluorescence map generated after the application of the plasmonic patch (scale bar represents 400 μ m). (C) Quantitative measurements of fluorescence intensity corresponding to the concentrations of various biomarkers in the urine samples of four patients (ID: #81, #67, #37, and #29) and two self-described healthy volunteers (ID: #M70 and #403). [+] indicates biomarker detected only after the application of the plasmonic patch. POS spots in the microarray represent three distinct positive control signal intensities (POS1>POS2>POS3). (D) Fluorescence intensity heat map corresponding to the concentrations of kidney diseases biomarkers in the urine samples of four patients (ID: #81, #67, #37, and #29) and two healthy volunteers (ID: #M70 and #403) before (left) and after (right) the application of the plasmonic patch.

Chapter 4: Gold Nanorod Size-dependent Fluorescence Enhancement

4.1 Introduction

Fluorescence-based sensing and imaging methods are widely employed in biomedical research and clinical diagnostics. However, these methods generally suffer from poor sensitivity due to the feeble fluorescence signal of conventional molecular fluorophores, resulting in low signal-to-noise ratio. It is known that fluorescence emission from organic dyes and inorganic emitters can be significantly enhanced by the intense electromagnetic field around plasmonic nanostructures, known as plasmon-enhanced fluorescence (PEF).⁶⁴⁻⁶⁵ Enhancement in the emission of fluorophores in close proximity to plasmonic nanostructures is attributed to the enhanced electromagnetic field (local excitation field) at the surface of the plasmonic nanostructures and the decrease in the fluorescence lifetime due to the coupling between the excited fluorophores and the surface plasmons of the nanostructures.^{9, 23-31} To achieve high fluorescence enhancement efficiency, it is important to design and realize plasmonic nanostructures that exhibit high electromagnetic field enhancement at the surface. For example, coupled plasmonic nanoantennas such as bowtie nanoantennas fabricated by electron-beam lithography resulted in more than 1000-fold enhancement in fluorescence from single molecules.⁶⁶ Several other complex plasmonic nanoconstructs such as antenna-in-box, plasmonic patch antenna⁶⁷, and periodic gold arrays³²⁻³³ also offer large fluorescence enhancement owing to the intense electromagnetic field generated by plasmonic coupling. However, due to their complex design, these coupled plasmonic nanoconstructs are generally difficult to realize in a controllable and scalable manner.

In contrast, individual nanostructures, especially gold nanorods (AuNR), are attractive candidates

for PEF applications due to their simple and scalable synthesis procedures with well-controlled size and shape, long-term stability, as well as tunable localized surface plasmon resonance (LSPR) wavelength. However, commonly employed AuNRs (with a diameter of 10-20 nm and a length of 30-60 nm) exhibit relatively weak electromagnetic field compared to coupled nanostructures, therefore compromising their fluorescence enhancement efficacy. Here, we demonstrate that fluorescence enhancement efficiency of AuNR can be significantly improved (by up to 300%) by simply optimizing their dimensions (length and diameter). We found that the fluorescence enhancement efficiency increases dramatically with an increase in the size of the AuNRs up to an optimal dimension, followed by a decrease with further increase in size. AuNRs with optimal dimensions of around 130 nm in length and 40 nm in diameter resulted in nearly 120-fold enhancement in fluorescence intensity of a near infrared dye (800CW) placed in vicinity of the AuNR.

In this study, we have employed “plasmonic patch”, a thin elastomeric film adsorbed with AuNRs, as the material platform for determining the effect of the dimensions of AuNRs on the fluorescence enhancement. We demonstrate that the “plasmonic patch” comprised of AuNRs with optimal dimensions can be applied to various fluoroimmunoassays as an add-on step to improve their sensitivity without any modifications to the current procedures.⁶⁸ Compared to commonly employed AuNR, size-optimized AuNR resulted in nearly 100-fold improvement in the sensitivity of human IL-6 fluoroimmunoassay. Finally, we demonstrate the real-world application of the size-optimized AuNR plasmonic patch for simultaneously enhancing the sensitivity of a 10-plex human cytokine microarray.

4.2 Results and discussion

Plasmonic patch is comprised of a thin polydimethylsiloxane (PDMS) film (thickness of ~40 μm)

with AuNRs uniformly absorbed on the surface. The elastomeric nature of PDMS ensures the conformal contact of the AuNR (on the patch) with fluorescent species on the surface of interest (*e.g.* fluoroimmunoassay surfaces) (Figure 1A) to effectively enhance the emission of the fluorophores on the surface (Figure 1B, C, D). Prior to the systematic investigation of the effect of the size of AuNR on the fluorescence enhancement efficiency, it is important to minimize the potential interference arising from other contributing factors. It is known that an optimal distance between a fluorophore and the metal surface is critical to balance the two opposing effects, namely metal-induced fluorescence quenching and plasmon enhancement, to realize high fluorescence enhancement efficiency. Based on our previous work, the spacer layer thickness was maintained to be 3 nm across all the plasmonic patches with various AuNRs. Previous studies have also shown the importance of matching the AuNR LSPR wavelength with the absorbance/emission of the fluorophore to maximize the fluorescence enhancement efficiency. We first set out to determine the optimal LSPR wavelength of AuNRs for near infrared dye, 800CW, which is employed as the model fluorophore in this study.^{24, 44, 47, 69}

To investigate the effect of the LSPR wavelength on the fluorescence enhancement, we fabricated plasmonic patches using eight distinct AuNRs with longitudinal LSPR wavelength ranging from ~700 nm to 800 nm. The AuNR density of various plasmonic patches was adjusted to a similar level ($92 \pm 5/\mu\text{m}^2$), as depicted in the SEM images (Figure S1A a-h). To form a dielectric spacer layer on the AuNRs, two silane monomers, namely (3-aminopropyl)trimethoxysilane (APTMS) and trimethoxy(propyl)silane (TMPS), were copolymerized on the surface of AuNR. As mentioned above, the optimal thickness of the spacer layer was found to be ~3 nm based on our previ-

ous study.⁶⁸ To test the fluorescence enhancement efficacy, plasmonic patches modified with various AuNRs were transferred onto the bottom of polystyrene wells (of standard 96-well plate), uniformly coated with 800CW. The LSPR wavelength of the plasmonic patch after its transfer to the 96-well plate surface showed a gradual red shift due to the increase in the effective refractive index of the medium surrounding the AuNRs (Figure S1B). Highest fluorescence enhancement (nearly 45-fold) was obtained for patches comprised of AuNR with LSPR wavelength around 758 nm and 774 nm (Figure S1C and D). After the transfer to the 800CW coated surface, the LSPR wavelength of the plasmonic patch comprised of AuNR-758 nm and AuNR-774 nm showed a large overlap between the plasmon extinction band and the absorption/emission bands of 800CW (Figure S1E), which resulted in their high fluorescence enhancement efficiency compared to other nanostructures. Therefore, AuNR with LSPR wavelength around 760 nm were employed in subsequent studies.

Next, we set out to investigate the size effect of the AuNR on the fluorescence enhancement efficiency. We synthesized AuNRs of different dimensions with LSPR wavelength of 760 ± 5 nm (Figure 2A, C). As synthesized AuNR exhibited similar aspect ratio (length/diameter) of around 3.2 (Figure 2B). AuNR density on each plasmonic patch was fixed to $50\pm 6/\mu\text{m}^2$, as evidenced by SEM images (Figure 3A). To form a dielectric spacer layer of similar thickness on the AuNRs, same amount of APTMS and TMPS were copolymerized on the surface of AuNR. Plasmonic patches were then transferred onto the bottom of standard 96-well plate coated with 800CW. After adding the plasmonic patches onto the bottom of polystyrene wells, the LSPR wavelength exhibited a large overlap with the absorption/emission of 800CW (Figure 3B). Fluorescence enhancement factor increased rapidly with an increase in the AuNR size and reached a maximum for

AuNRs with a length of 110 nm (Figure 3C and D). Further increase in the length resulted in a decrease in the fluorescence enhancement factor. Nearly 120-fold fluorescence enhancement was observed for patches comprised of AuNR-113×38nm (Figure 3C and D).

To understand the size-dependent enhancement phenomenon, we performed finite-difference time-domain (FDTD) simulations that revealed the electromagnetic field intensity around AuNRs of different sizes (Figure 3E). Electromagnetic field intensity at 3 nm (accounting for the polymer spacer layer) from their surface was found to rapidly increase with an increase in the size of the AuNR and reached the maximum value for AuNR with a length of 110 nm. Further increase in the length of the AuNR resulted in a decrease in the electromagnetic field intensity (Figure 3F). The AuNR size-dependent electromagnetic field intensity deduced from the FDTD simulations showed excellent agreement with the experimentally observed size-dependent fluorescence enhancement. It is known that for smaller AuNRs, electron-surface scattering dominates the plasmon damping, while radiation damping rapidly increases with the volume of the AuNR and becomes dominant factor for larger nanorods.⁷⁰⁻⁷¹ As the size of the AuNR increases, the lightning rod effect, which results in a strong electromagnetic field enhancement at the AuNR end caps, becomes weaker due to the decrease in the local curvature.⁷² Collectively, these factors determine the optimal dimensions of AuNR for attaining the maximal field enhancement at the surface of the AuNR.

Next, we evaluated the effect of the density of these plasmonic nanostructures (on PDMS film) on the fluorescence enhancement efficiency. We have fabricated plasmonic patches with different densities of AuNRs with a length of 130 nm and diameter of 40 nm by increasing the concentration of the AuNR solution deposited on the PDMS film (Figure S2). SEM images depict plasmonic

patches with AuNR density of $12.0 \pm 2.6/\mu\text{m}^2$, $14.2 \pm 3.1/\mu\text{m}^2$, $25.3 \pm 2.2/\mu\text{m}^2$, $47.3 \pm 2.8/\mu\text{m}^2$, $55.4 \pm 2.8/\mu\text{m}^2$ and $57.8 \pm 3.7/\mu\text{m}^2$ (Figure 4A). Correspondingly, the plasmonic extinction intensity of the patches showed a gradual increase with an increase of the density of AuNR (Figure 4B). These plasmonic patches were transferred onto the bottom of standard 96-well plate coated with 800CW. We observed a density dependent-fluorescence enhancement (Figure 4C). The fluorescence enhancement factor was found to increase with an increase in the density of the AuNRs on the plasmonic patch and essentially plateaued for densities higher than $\sim 48/\mu\text{m}^2$ (Figure 4C, D). Increasing the density of the large AuNRs (130×40 nm) beyond $60/\mu\text{m}^2$ was found to be difficult. Similar saturation of the fluorescence enhancement factor was also observed for smaller AuNRs with the increase of the AuNR density on the patch (57×18 nm) (Figure S3).

To understand the saturation of the fluorescence enhancement factor with increasing AuNR density, we have employed FDTD simulations (Figure 4 E to H). It is known that metal nanostructures at the LSPR wavelength can absorb and scatter significantly more light than directly incident on them.⁷³⁻⁷⁴ Local time-averaged Poynting vector field around the AuNR at the longitudinal LSPR wavelength, which represents the optical power flow, was deduced using FDTD simulations (Figure 4F-H). Based on the calculated extinction spectrum, the extinction cross-section of a single AuNR (with length of 130 and diameter of 40 nm) at the longitudinal LSPR wavelength was determined to be $55,510 \text{ nm}^2$,⁷⁵ which indicates that $\sim 18 \text{ AuNRs}/\mu\text{m}^2$ are sufficient to absorb and confine most of the incident light. In the FDTD simulation, the electric field of the incident plane wave was set to be parallel to the long-axis of the AuNR (Figure 4F). However, since the AuNRs on the plasmonic patch are randomly orientated with respect to the polarization of the incident beam, experimentally determined density of AuNR ($40\text{-}50 \text{ AuNR}/\mu\text{m}^2$) for saturation of the fluorescence enhancement factor was slightly higher than that estimated from the FDTD calculations

(18 AuNR/ μm^2).

Following the optimization of the AuNR size effect as well as its density on the plasmonic patch, we set out to test the applicability (aspect ratio~ 3.25, AuNR-130 \times 40 nm, density~ 55.6 \pm 2.7/ μm^2) in improving the bioanalytical parameters (*i.e.* sensitivity, limit-of-detection, dynamic range) of a conventional fluoroimmunoassay. IL-6 was employed as the target protein biomarker, which acts as both anti-inflammatory and proinflammatory cytokine⁷⁶. Recent studies suggested that salivary and serum IL-6 (together with other cytokines) hold promise as biomarkers for oral squamous cell carcinoma (OSCC).⁷⁷⁻⁷⁹ In contrast to other cancer biomarkers, such as prostate-specific antigen (PSA), the concentration of IL-6 concentration in serum (both healthy and diseased state) are around 1,000-fold lower.⁸⁰ IL-6 level in healthy human serum ranges from a few fg/ml to about 6 pg/mL.⁸¹ In pathological condition, it can be present at higher concentrations.

Here, we postulated that adding plasmonic patch with optimal AuNR dimensions as a fluorescence signal enhancer in an IL-6 fluoroimmunoassay would significantly improve the bioanalytical parameters (e.g. sensitivity, dynamic range) due to the large fluorescence enhancement offered by the AuNR size-optimized plasmonic patch. In accordance with the standard workflow of ELISA, 96-well plate was used to perform this assay, which involves (i) immobilization of IL-6 capture antibody (ii) capture of the IL-6 by the immobilized antibody; (iii) binding of the biotinylated detection antibody to the captured IL-6; (iv) binding of a fluorophore (800CW)-labeled streptavidin to the biotinylated detection antibody. Finally, plasmonic patch was simply added onto the top of the immunosandwich as the new, last step. (Figure 5A).

To investigate the improvement in sensitivity and dynamic range of the fluoroimmunoassay, serial dilutions of IL-6 of known concentrations (0.006 to 6000 pg/ml in 1% BSA) as well as blank

control were employed as standards. The fluorescence images obtained before applying the plasmonic patch showed extremely weak signal with a limit-of-detection ~ 600 pg/ml (Figure 5B). The fluorescence intensity was significantly enhanced after applying plasmonic patches comprised of AuNR-57 \times 18nm and AuNR-130 \times 40 nm (Figure 5 C, D, and S4). Notably, the LOD (5σ) of the plasmon-enhanced IL-6 assay was calculated to be ~ 60 fg/ml (~ 3 fM) using plasmonic patch comprised of AuNR-130 \times 30nm, which is ~ 100 times lower compared to the LOD obtained using the sub-optimal plasmonic patch comprised of AuNR-57 \times 18nm (~ 6 pg/ml). More importantly, the LOD obtained with optimal plasmonic patch (60 fg/ml, 3 fM) is nearly 100-fold lower than gold standard ELISA (R&D systems, DY206), which relies on enzymatic amplification of colorimetric signal. In addition to the enhanced sensitivity, plasmonic patch-enhanced fluoroimmunoassay showed significantly larger dynamic range (from 60 fg/ml to 6 ng/ml) compared to that of vendor-specified ELISA (R&D systems, DY206). These results further validate the importance of optimizing the plasmonic nanostructures, and by extension plasmonic patch, for various bioanalytical applications.

Finally, we applied the plasmonic patch comprised of AuNRs with optimal dimensions on a quantitative protein microarray to test the feasibility of using plasmonic patch to simultaneously enhance the limit-of-detection of multiple protein biomarkers. Here, human inflammation microarray for 10 cytokines were employed and the capture antibody for each cytokine together with the positive controls are arrayed in quadruplicate on the glass slide with a feature diameter of 150 μ m (Figure 6A). To determine the limit-of-detection for each cytokine in the microarray, the array specific cytokine standards, whose concentration has been predetermined, were employed. Next, biotin-labeled detection antibody cocktail was added to recognize a different epitope of the cytokine, followed by the addition of the streptavidin-800CW fluorophore. Finally, plasmonic patch

(with large AuNR-130×40 nm) was applied on the microarray. The fluorescence map of the microarray revealed a large enhancement in the fluorescence signal for all the target analytes at different concentrations after the addition of plasmonic patch on the microarray (Figure 6B). We noted a significant improvement in the limit-of-detection for all the 10 cytokines (Figure 6C and S5). Notably, limit-of-detection of IL-6 was lowered from 259.48 pg/ml to 9.16 pg/ml, indicating an almost 28-fold improvement in the sensitivity by adding plasmonic patch (Figure 6D, E). In addition to the improved sensitivity for each cytokine, the coefficient of variation (CV) of the fluorescent signal after plasmonic patch was smaller compared to the non-enhanced fluorescence microarray (Figure 6D, E, S5). This can be attributed to the significantly enhanced fluorescence signal, which is much higher than the interference noise level from background as well as the fluorescence detector.

4.3 Conclusions

To summarize, we have systematically studied the effect of the size of the AuNRs on their fluorescence enhancement efficiency. We found that in addition to the LSPR wavelength of the plasmonic nanostructures, their absolute dimensions are critical for maximizing the fluorescence enhancement obtained using plasmonic patch. The optimal dimensions of the AuNRs determined using FDTD simulations for attaining maximum electromagnetic field enhancement showed excellent agreement with experimentally determined dimensions of the AuNRs that exhibited highest fluorescence enhancement. Compared to the unenhanced fluoroimmunoassay and the gold standard ELISA, the AuNR size optimized plasmonic patch-enhanced fluoroimmunoassay exhibited nearly 10,000-fold and 100-fold lower limit-of-detection, respectively. High sensitivity and large dynamic range combined with the use of established bioassay platform (e.g., 96-well plates, multiplex microarrays, standard affinity reagents, read-out devices) and work-flow makes the plasmon

enhanced fluoroimmunoassays highly attractive for research and clinical applications.

4.4 Experimental section

Materials

Polydimethylsiloxane (PDMS), cetyltrimethylammonium bromide (CTAB), ascorbic acid, chloroauric acid, sodium borohydride, tris(hydroxymethyl)amino methane (tris), poly(styrene sulfonate) (PSS) ($M_w = 100,000 \text{ g/mol}$), (3-Aminopropyl)trimethoxysilane (APTMS), and trimethoxypropylsilane (TMPS) were purchased from Sigma Aldrich (St. Louis, MO). Silver nitrate was purchased from VWR International. IL-6 ELISA kit (DY 206) was purchased from R&D systems (Minneapolis, MN). Concentrated phosphate buffered saline (PBS) was purchased from Omnipur. All chemicals have been used as received with no further purification.

Synthesis of gold nanorods (AuNRs)

AuNRs were synthesized using a seed-mediated approach⁸². Seed solution was prepared by adding 0.6 ml of an ice-cold sodium borohydride solution (10 mM) into 10 ml of CTAB (0.1 M) and chloroauric acid ($2.5 \times 10^{-4} \text{ M}$) solution under vigorous stirring at 25 °C. The color of the seed solution changed from yellow to brown. For synthesizing AuNRs with different wavelengths, growth solutions were prepared by mixing 38 ml of CTAB (0.1 M), 0.25 ml (or 0.3, 0.35, 0.4, 0.45, 0.5, 0.55 and 0.6 ml for different LSPR wavelengths) of silver nitrate (10 mM), 2.0 ml of chloroauric acid (10 mM) and 0.22 ml of ascorbic acid (0.1 M) in that order. Then 48 μl of freshly prepared seed solution was added into the growth solution and this solution was kept in the dark for overnight to obtain AuNRs with different LSPR wavelengths.

For synthesizing AuNRs with different sizes, growth solution was prepared by mixing 38 ml of CTAB (0.1 M), 0.25 ml (or 0.30, 0.35, 0.40, 0.45, 0.50, 0.55 and 0.6 ml for different sizes) of silver nitrate (10 mM), 2.0 ml of chloroauric acid (10 mM), 0.22 ml ascorbic acid (0.1 M) and 0.8 ml HCl (1.0 M) consecutively. Subsequently, 0.2 μ l (or 0.4, 2.5, 5, 10, 25, 30 and 48 μ l for different sizes) of freshly prepared seed solution was added into the growth solution and this solution was kept in the dark for overnight to obtain AuNRs with different size. Finally, the AuNR was washed by centrifugation and redispersed in nanopure water to achieve a final extinction of 2.0.

Plasmonic patch preparation

Sylgard 186 (Dow Corning) polydimethylsiloxane prepolymer was mixed with curing agent at a 10:1 (polymer to curing agent) ratio. This mixture was spin coated at the speed of 3000 rpm for 30 seconds on a 35 mm diameter polystyrene petri dish. The PDMS film was then cured at 60°C for 12 hours. In order to facilitate the adsorption of AuNR on PDMS, the PDMS film was first treated by oxygen plasma for 3 mins, followed by treatment with 2 ml of 0.2% aqueous poly(styrene sulfonate) (PSS) for 20 mins (this step facilitates the adsorption of AuNR on PDMS film through electrostatic interactions between positively charged AuNR and negatively charged PSS). Then, 1ml of AuNR solution (described above) was centrifuged and redispersed into 1.5 ml of nanopure water. For synthesizing the plasmonic patch AuNR-130 \times 40nm with decreasing density of AuNR, 2.0 ml, 1.5 ml, 1.0 ml, 0.5 ml, 0.25 ml and 0.125 ml of AuNR solution were centrifuged and redispersed into 1.5 ml of nanopure water. Subsequently, the PSS-treated PDMS film was incubated with the above mentioned 1.5 ml AuNR solution for 15 hours in the dark. Finally, PDMS films was rinsed with nanopure water to remove weakly bound AuNRs and blow-dried under a stream of nitrogen.

Polymer spacer on plasmonic patch

In order to optimize the distance between AuNR surface and fluorophores, a thin layer of polysiloxane was formed on the surface of the AuNR. For the purpose, 8 μl of APTMS and 0.25 μl of TMPS were added into 3 ml of phosphate buffered saline (1X PBS). Then the plasmonic patch was incubated in this solution for 2 hours at room temperature. After 2 hours, the plasmonic patch was rinsed with PBS and nanopure water and blow-dried with under a steam of nitrogen.

Plasmonic patch enhanced fluoroimmunoassay

Plasmonic patch enhanced fluoroimmunoassay was implemented using 96-well plates with plastic bottom. The plate was first incubated with IL-6 capture antibody (2 $\mu\text{g}/\text{ml}$ in PBS) for overnight followed with 1.5-hour blocking using 3% BSA. 100 μl of standard solutions with different IL-6 concentrations were then added into appropriate wells. The plate was sealed and then gently shaken for 2.5 hours at room temperature. The solution was then discarded, and the wells were washed 4 times with washing buffer (1X PBS with 0.05% Tween 20). Subsequently, 100 μl of biotinylated antibody solution (50ng/ml) was added into each well and incubated for 2 hours at room temperature. After washing, 100 μl 800CW-labeled streptavidin (50 ng/ml) was added to each well followed by 20 min incubation. The plate was washed 3 times each with washing buffer followed with nanopure water. Finally, the plasmonic patch was transferred onto each well of the 96-well plate, followed by the addition of a reflective layer on the top. The plate was incubated in 40 degree for 20 min to allow the evaporation of any liquid. LICOR Odyssey CLx scanner was used to scan the 96-well plate.

Plasmonic patch enhanced fluorescence microarray

Commercialized protein quantitative microarray kit was purchased from RayBiotech (Quantibody® Human Inflammation Array 1, QAH-INF-1). Antibodies were printed on a glass slide with 16 subarrays available per slide. The slide was blocked by blocking buffer (in kit) for 30 mins. Standard samples with various cytokine concentrations and blank control sample were prepared and were added into each sub-well of the microarray chip followed by a two-hour incubation at room temperature. The chip was then washed thoroughly with wash buffer (in kit). Next, 70 µl of biotin-conjugated anti-cytokines cocktail (in kit) were added to each subarray and the chip was incubated at room temperature with gentle shaking. After two hours, the chip was washed and 70 µl of streptavidin-800CW (100 ng ml⁻¹ in blocking buffer) was added and the plate was incubated under dark conditions for 20 mins. The chip was washed thoroughly with wash buffer then nanopure water and blow dried under nitrogen gas. The glass chip was scanned by Azure Sapphire imager using 800 nm channel. Finally, plasmonic patch of AuNR-760 was cut into 1×1 cm² and applied on the top of each subarray. The chip was rescanned using the same settings.

4.5 Figures

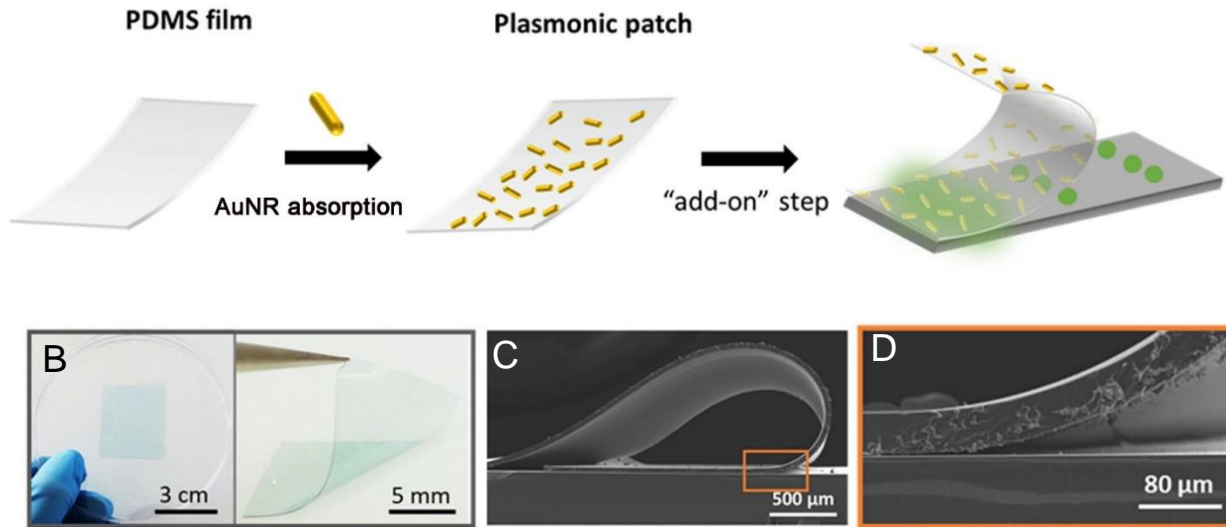


Figure 4. 1 (A) Schematic representation of the simple “add-on” process to enhance the fluorescence emission based on an elastomeric plasmonic patch. (B) Photographs of plasmonic patch comprised of gold nanorods (AuNRs). (C) SEM image of the plasmonic patch showing the high flexibility. (D) Zoom-in SEM image of the interface between the plasmonic patch and the silicon substrate showing the high conformability.

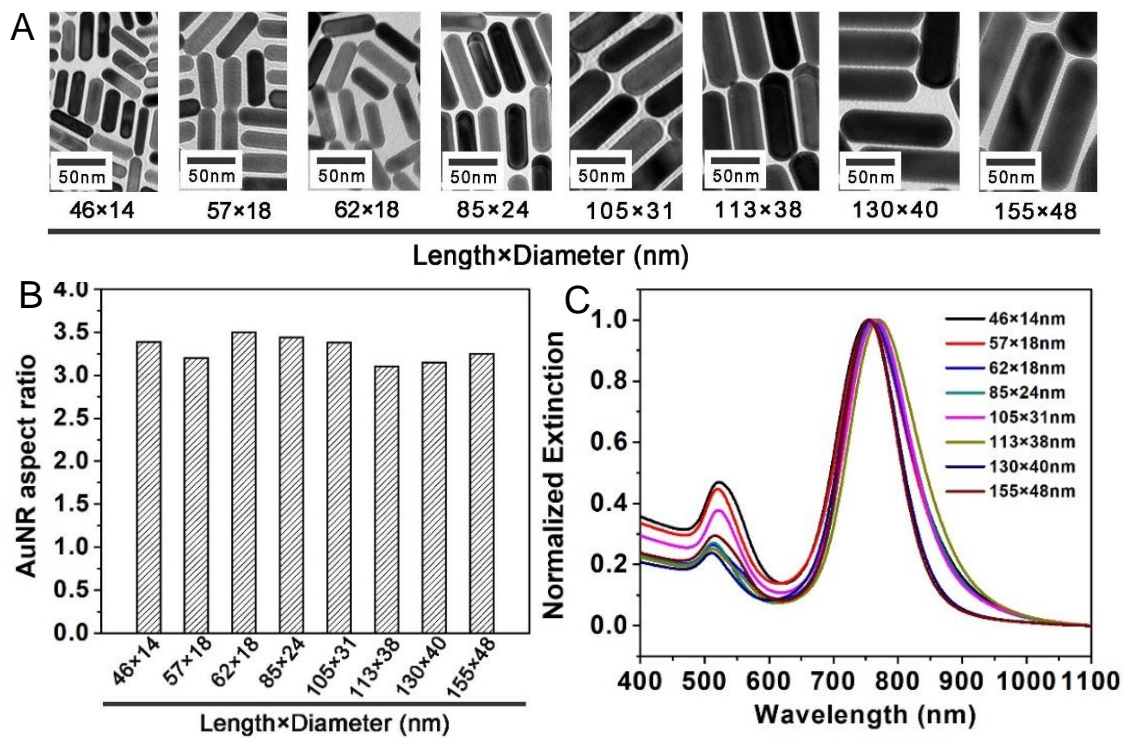


Figure 4. 2 (A) TEM images of AuNRs with increasing size (length x diameter) (B) Aspect ratio of the AuNRs shown (A). (c) Normalized extinction spectra of the aqueous solutions of AuNRs, showing similar LSPR wavelength.

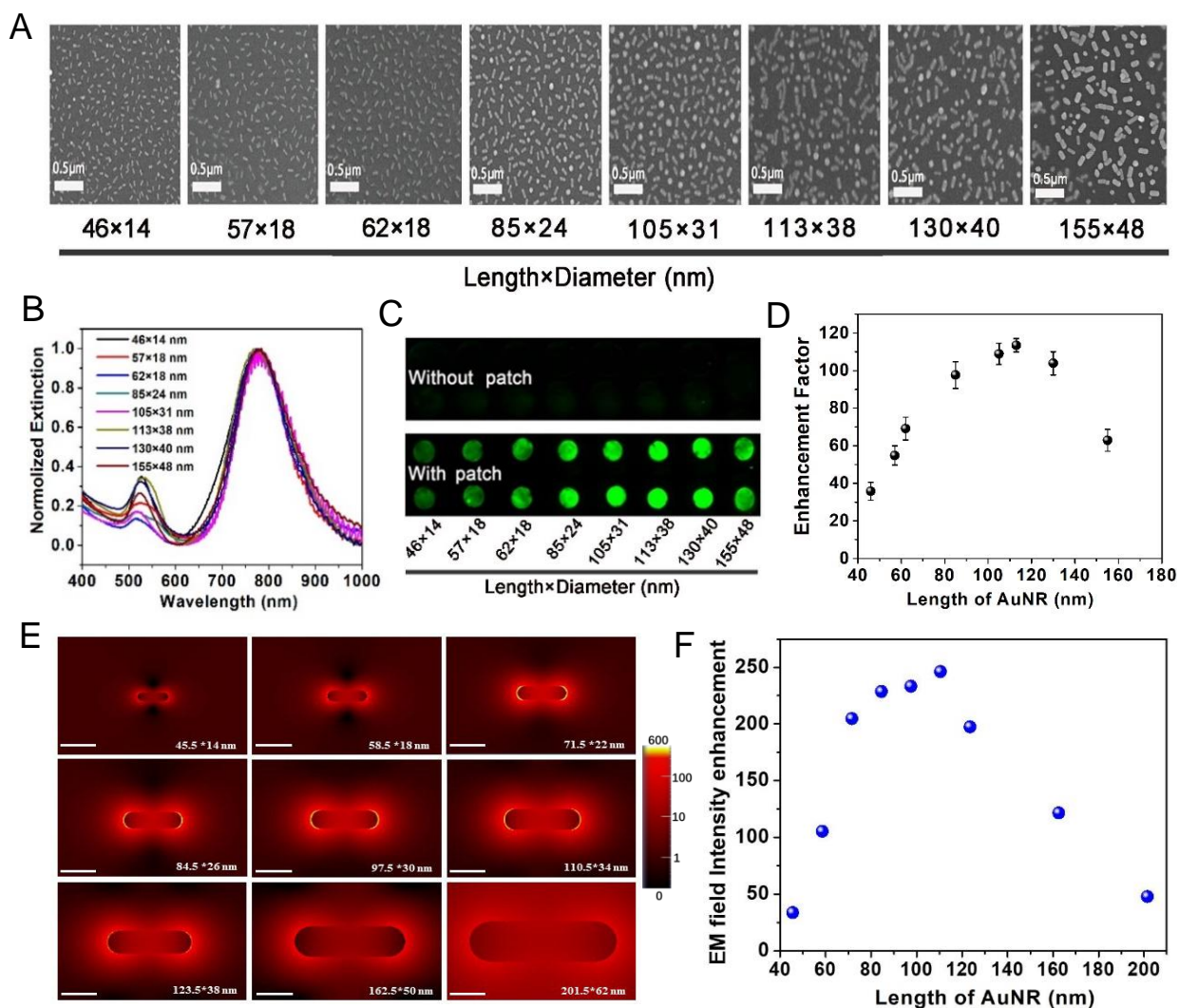


Figure 4. 3 (A) SEM images of the plasmonic patch revealing similar density of different size AuNRs on PDMS (from left to right: AuNR-46×18nm, AuNR-57×18nm, AuNR-62×18nm, AuNR-85×24nm, AuNR-105×31nm, AuNR-113×38nm, AuNR-130×40nm and AuNR-155×48nm). (B) Vis-NIR extinction spectra of the plasmonic patches comprised of AuNRs with different dimensions after being transferred to 96-well plate, which exhibit a slight red shift compared to the LSPR wavelength in aqueous solutions. (C) The fluorescence map and (D) calculated enhancement factors of emission of 800CW using the plasmonic patches with AuNR of different sizes. (E) Finite-difference time-domain (FDTD) simulation, showing electromagnetic field around AuNRs with different sizes (Scale bar represents 50 nm). (F) Plot showing the electromagnetic field intensity enhancement for AuNRs of different dimensions (from length 46 nm to 200 nm).

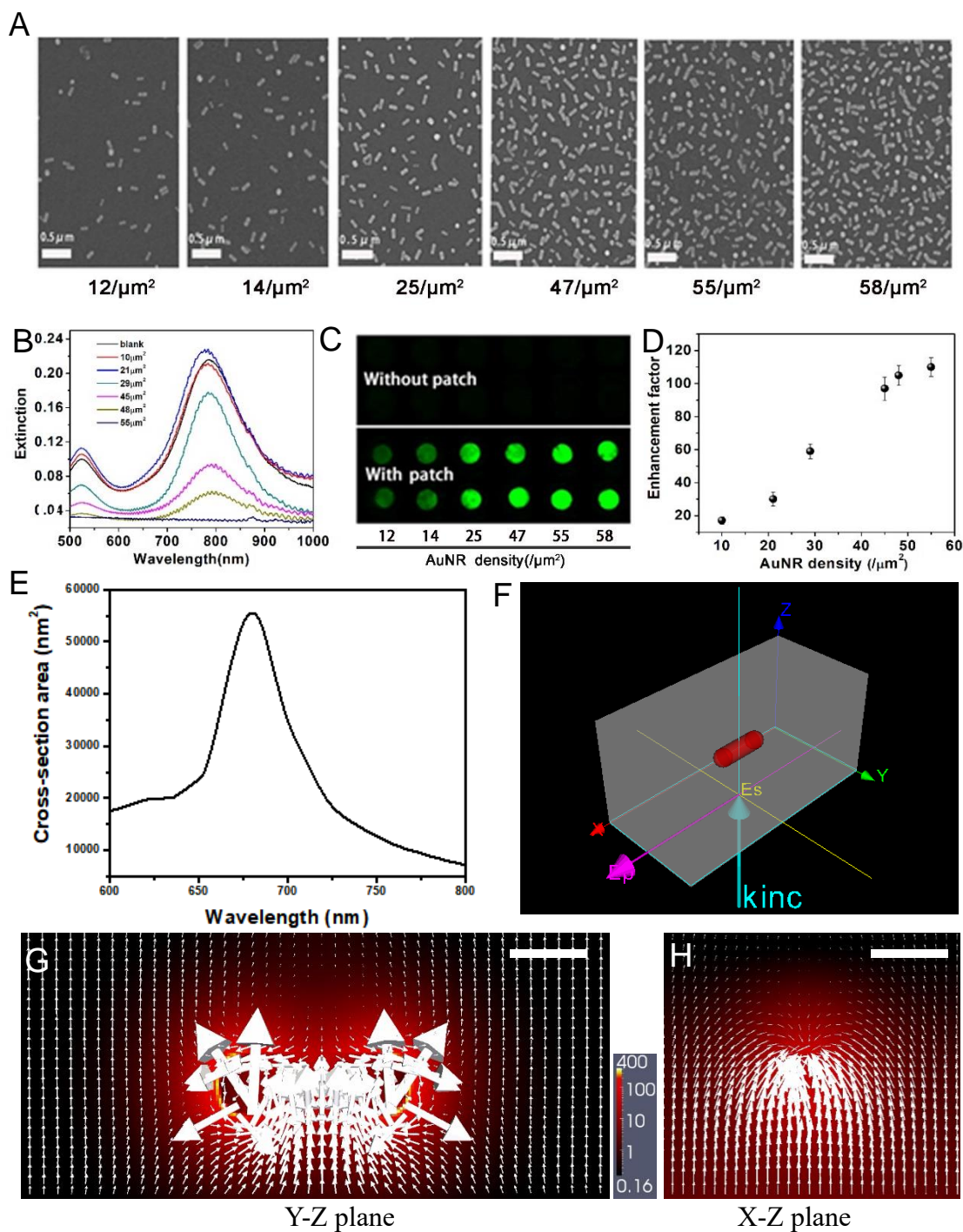


Figure 4. (A) SEM images of the plasmonic patch AuNR-130×40nm with increasing density of AuNR. (B) Extinction spectra of plasmonic patches of AuNR-130×40nm with different AuNR densities after transferring them to 96 well plate. (C) Fluorescence maps and (D) plot showing the fluorescence enhancement efficacy of plasmonic patches with different AuNR density. (E) Simulated spectra of AuNR-130×40 nm with incident light polarized along the long-axis of the AuNR. (F) Illustration showing the finite-difference time-domain (FDTD) simulation of AuNR 130×40 nm, (G) (H) Distribution of electric field intensity (background) and Poynting vector (white arrows) in Y-Z plane and X-Z plane (Scale bars represent 50 nm).

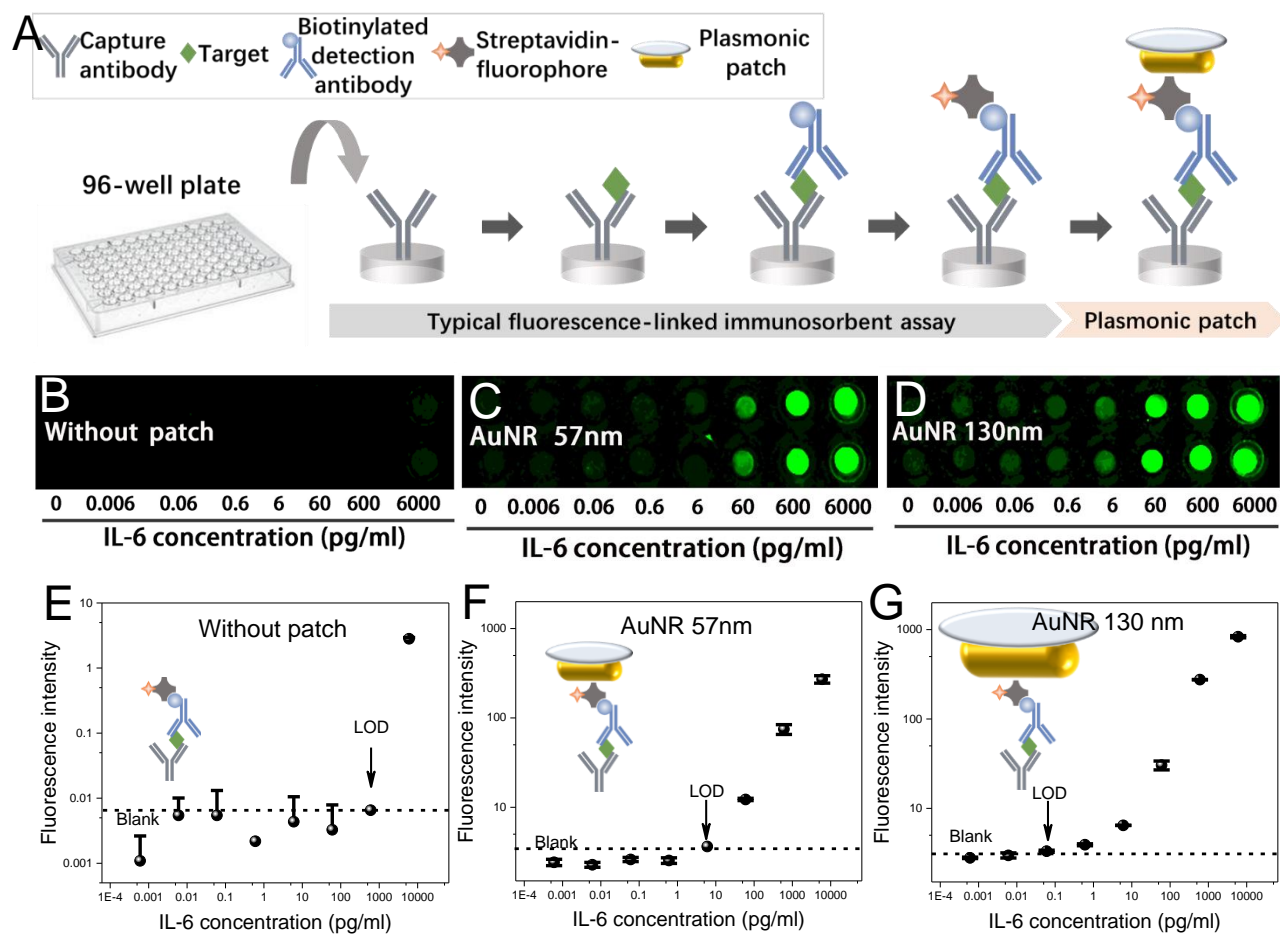


Figure 4. 5 (A) Schematic showing the steps involved in plasmonic patch-enhanced IL-6 fluoroimmunoassay implemented on a plastic bottom 96-well plate. Fluorescence map of (B) unenhanced IL-6 fluoroimmunoassay (C) AuNR-57nm (57×18 nm) enhanced, and (D) AuNR-130 nm (130×40 nm) enhanced IL-6 fluoroimmunoassay. Plot showing the IL-6 dose dose-response curve of (E) conventional IL-6 fluoroimmunoassay (F) AuNR-57 nm (57×18 nm) enhanced, and (G) AuNR-130 nm (130×40 nm) enhanced IL-6 fluoroimmunoassay.

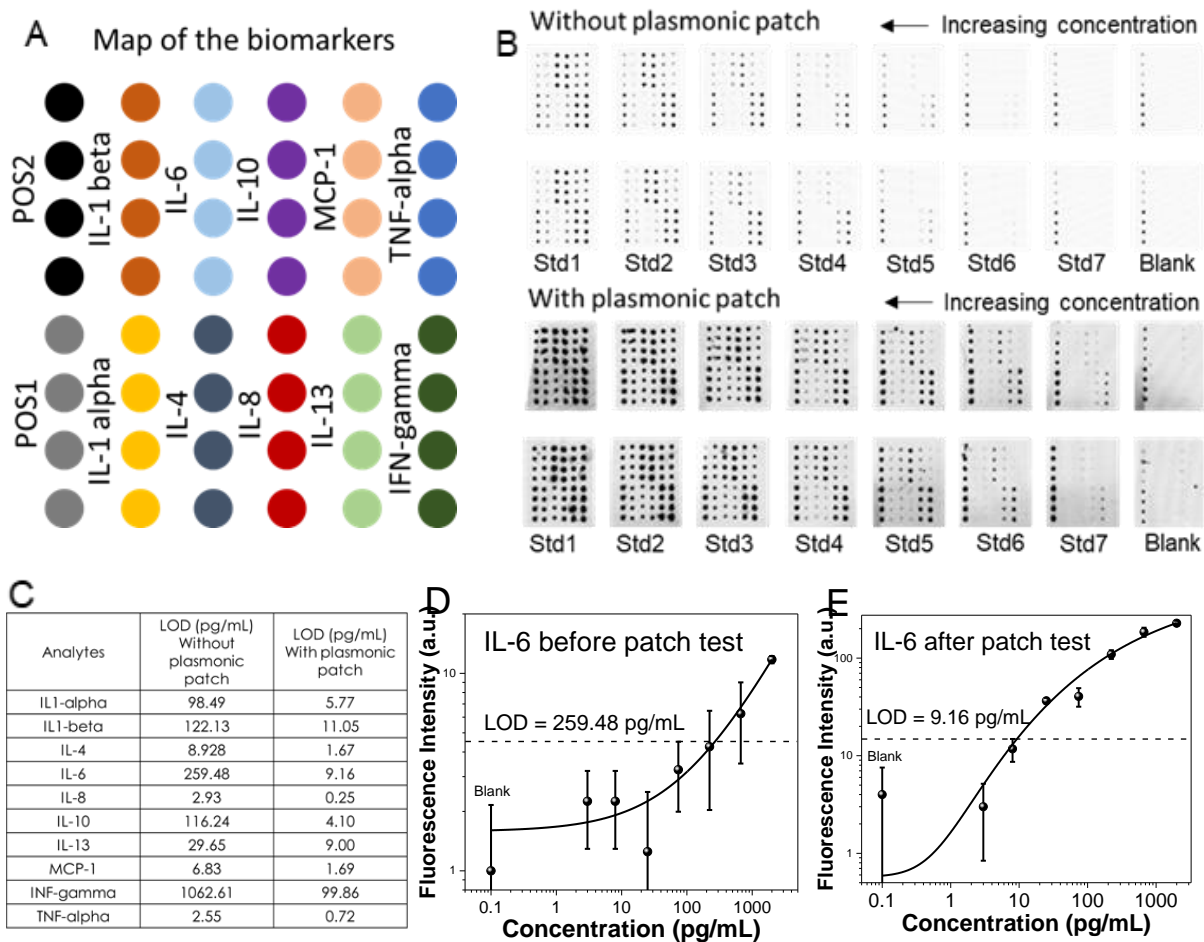


Figure 4. 6 Quantitative measurement of multiplexed microarray of 10 human cytokines using size optimized plasmonic patch. (A) Layout of the antibodies corresponding to the cytokines on the quantitative microarray. Each type of antibody is printed in quadruplicate on the glass substrate. (B) Fluorescence map of the 10-plex microarray under various analytes concentrations. Top: without adding plasmonic-patch. Bottom: with plasmonic-patch enhancement. (C) Limit-of-detection of each cytokine before and after addition of plasmonic-patch. Standard curves of IL-6 (D) before and (E) after applying plasmonic-patch.

Chapter 5: Ultrabright Plasmonic-fluor as a Cross-platform Nanolabel for Femtomolar Detection of Bioanalytes

5.1 Introduction

Relevant concentrations of biomolecules or biomarkers related to diseases such as cancer, heart disease, inflammation, and neurological disorders can range in many orders of magnitude from $\mu\text{g/ml}$ levels to sub-fg/ml, some of which possibly still remain unidentified due to the lack of sensitive bioanalytical tools.⁸³⁻⁸⁹ It is also highly desirable to utilize small sample volume for multiplexed detection within precious biofluids such as breath condensates, ocular fluids, cerebrospinal fluid, or serum from neonates or small animal models, which necessitates sample dilutions, further lowering the concentration. As the cornerstone of biomedical science and clinical research, fluorescence-based bioanalytical methods are widely employed in the detection, quantification and imaging of a broad range of bioanalytes.^{26-28, 90} Several methods, such as enhancing antibody affinity⁹¹, reducing the background fluorescence⁹², promoting mass transfer⁹³, and increasing the substrate surface area^{26, 93}, have been explored to improve the sensitivity of fluoroimmunoassays. However, weak fluorescence signal and the associated poor signal-to-noise ratio of the fluorescence label remains a persistent challenge, limiting the ultimate sensitivity of current fluorescence-based assays.^{27, 94-96}

Extensive efforts have been dedicated in creating bright fluorescence signal that involves the conversion of a single molecular event into thousands (or more) of fluorophores in a localized “enzyme-free” manner.⁹⁷⁻¹⁰³ Achieving ultrabright nanostructures by simply packing a large number of fluorophores into a nanoscale volume is extremely challenging due to the aggregation induced

self-quenching of fluorophores at high local concentration, limiting the fluorophore loading and consequently their brightness.^{100, 104} One solution to prevent the formation of non-emissive H-aggregates is to engineer the inter-fluorophore distance and orientation, for example, by modifying the fluorophore with bulky side groups¹⁰⁵⁻¹⁰⁶ or using charged dyes with hydrophobic counterions⁹⁷. However, the loading is still limited to tens or hundreds of fluorophores per nanoparticle in these cases. Fluorescent nanoparticles based on Förster resonance energy transfer (FRET) represents an attractive method that can harvest incident light and transfer it to adjacent energy acceptors. However, limited by the Förster radius (typically much shorter than the radius of nanostructure, which hinders the efficient energy transfer from a whole nanoparticle to the energy acceptor) and self-quenching of donors at high local concentration, efficient FRET system (1000-fold brighter than single fluorophore) was not demonstrated until recently.^{102, 107} Again, this method is only applicable to charged fluorophores and broad application of these nanostructures in fluorescence-based bioanalytical and bioimaging techniques has not been demonstrated.¹⁰²

Here, we introduce a highly stable and extremely bright fluorescent nanoconstruct, termed “plasmonic-fluor”, which exhibits up to 6700 (\pm 900)-fold brighter signal compared to the corresponding single near infrared (NIR) fluorophore (800CW) and vastly outperforms existing nanoengineered fluorescent structures.⁹⁷⁻¹⁰³ This novel nanoconstruct integrates plasmon-enhanced fluorescence, universal bio-linker element, and “BSA surface blocking” strategy, enabling it to serve as a highly specific and cross-platform label in various fluorescence-based bioanalytical and imaging methodologies to dramatically enhance the signal-to-noise ratio. Harnessing the novel nanoconstruct (*i.e.* plasmonic-fluor), for the first time, we demonstrate the universal application of plasmon-enhanced fluorescence in vastly improving the sensitivity of a broad variety of bioanalytical

applications, such as fluorophore-linked immunosorbent assays (FLISA), multiplexed bead-based fluoroimmunoassay, high-throughput protein arrays, immunocytochemistry/immunofluorescence (ICC/IF), and flow cytometry.

5.2 Results and discussion

5.2.1 Fabrication of plasmonic-fluor.

“Plasmonic-fluor” is comprised of a plasmonic nanostructure (as fluorescence enhancer), a light emitter (e.g., fluorophores), spacer layer, and a universal biological recognition element (e.g. biotin) (Figure 1A). To assemble all of these functional components, we have employed bovine serum albumin (BSA) as a scaffold. As a key design element, BSA also serves as (i) a stabilizing agent, preventing the aggregation of the nanoconstructs; and (ii) a blocking agent, minimizing non-specific binding of the plasmonic-fluor to arbitrary surfaces and biomolecules, which is extremely important to achieve high signal-to-background ratios. BSA is covalently conjugated with fluorophores and biotin and subsequently coated around the plasmonic nanostructures to realize plasmonic-fluors. The synthesized plasmonic-fluor exhibited strong and specific affinity to streptavidin (a tetrameric biotin-binding protein), owing to the high affinity ($K_d \approx 10^{-14}$ mol/L) of biotin-streptavidin complex.¹⁰⁸ Streptavidin conjugated with a fluorophore is widely used in fluorescence-based bioanalytical techniques as a universal signal reporter. We hypothesized that following the binding of streptavidin, plasmonic-fluor can be introduced as an “add-on” step to enhance the fluorescence signal without entailing any change in the existing bioassay protocols (Figure 1B).

Gold nanorods (AuNRs) are employed as representative plasmonic nanoantennae owing to the facile tunability of their longitudinal localized surface plasmon resonance (LSPR) wavelength with aspect ratio and large electromagnetic field enhancement at their ends (see Supporting Information,

Figure S1).¹⁰⁹⁻¹¹¹ AuNRs (length 83.0 ± 8.0 nm; diameter 24.3 ± 1.8 nm) were modified with (3-mercaptopropyl)trimethoxysilane (MPTMS), which served as an interfacial layer for the copolymerization of two organosilane monomers, namely (3-aminopropyl)trimethoxysilane (APTMS) and trimethoxypropylsilane (TMPS) (Figure S2). In aqueous media, APTMS and TMPS undergo rapid hydrolysis and subsequent condensation around the MPTMS-modified AuNRs, yielding an amorphous copolymer network (Figure S2). The siloxane copolymer serves as a spacer layer between metal surface and the fluorophore to prevent fluorescence quenching (Figure 1D). This sol-gel approach enables facile control over the thickness of the spacer layer down to 1 nm, as evidenced by atomic force microscopy (AFM) (Figure S3). Modification of AuNRs with MPTMS and subsequent polymerization of APTMS/TMPS reduced the zeta potential of cetyl trimethylammonium bromide (CTAB)-capped AuNR from $+38.4 \pm 2.3$ mV to $+29\pm 2.6$ mV and $+25.8\pm 1.9$ mV, respectively, due to the partial replacement of the positively charged capping agent (CTAB) with less charged siloxane copolymer (Figure 1C).

Near infrared (NIR) fluorophore 800CW and biotin were conjugated to BSA through carbodiimide coupling chemistry to realize conjugates with protein/biotin/fluorophore ratio of 1: 8.7: 1.2 (Supporting information, Figure S4 and S5). Subsequently, the BSA-biotin-800CW conjugates are adsorbed on polysiloxane-coated AuNR through electrostatic, hydrophobic and hydrogen bonding interactions between BSA and the functional groups ($-\text{NH}_3^+$, $-\text{CH}_3$, $-\text{OH}$) of the polysiloxane layer to realize plasmonic-fluor-800CW. As formed plasmonic-fluor-800CW exhibited a negative charge (zeta potential -46.9 ± 0.5 mV at pH=10) due to abundant carboxylic acid groups in BSA with an isoelectric point of 4.7 (Figure 1C).¹¹² LSPR wavelength of AuNR exhibited a progressive red shift of 2.6 nm and 2.7 nm with the formation of polymer spacer layer and BSA-biotin-800CW

adsorption, respectively (Figure 1E). TEM images further confirmed the presence of a thin organic layer (polymer and BSA conjugate) around AuNR with an overall thickness of $\sim 6.3 \pm 1.4$ nm (Figure 1F).

Following the structural characterization of plasmonic-fluor-800CW, we set out to determine the brightness of the fluorescent nanoconstruct. The excited state fluorescence lifetimes of free 800CW (conjugated to BSA) and plasmonic-fluor-800CW were measured to be 0.74 ± 0.01 ns and 0.179 ± 0.001 ns, respectively, accounting to a 7-fold increase in the quantum yield (from $\sim 11\%$ to $\sim 79\%$, see supporting information for calculation) (Figure 2A, S6, S7).¹¹³ To further understand the brightness of plasmonic-fluor-800CW, we estimated the number of fluorophores conjugated to a single AuNR. Plasmonic-fluor-800CW at concentration of 76.2 pM (extinction of ~ 0.63) is comprised of ~ 16 nM 800CW (see supporting information for detailed calculation). Therefore, we can estimate that approximately 210 fluorophores are conjugated to a single AuNR. Notably, fluorescence intensity from 76.2 pM plasmonic-fluor-800CW (containing 16 nM 800CW) was found to be equivalent to the fluorescence intensity from 544 nM 800CW (measured based on Figure 2B). Therefore, it can be concluded that each 800CW is enhanced by nearly 30-fold due to the presence of plasmonic nanoantennas. The slope of fluorescence intensity vs. molar concentration of plasmonic-fluor-800CW is 6700 (± 900)-fold steeper than that of the conventional fluorophore (800CW) (Figure 2B, S8), suggesting that each plasmonic-fluor exhibits 6700 (± 900)-fold higher brightness than the corresponding fluorophore.^{98, 114} The observed intense emission can be attributed to the enhanced electromagnetic field (local excitation field) at the surface of the plasmonic nanostructures (Figure S1) and decrease in the fluorescence lifetime due to the coupling between excited fluorophores and surface plasmons of the nanostructures.^{9, 23-27, 29-31, 115}

We tested feasibility of using plasmonic-fluor-800CW as ultrabright fluorescent reporters by binding them to a substrate coated with streptavidin-800CW (see Methods section for detailed procedure, Figure S9). Remarkably, binding of plasmonic-fluor-800CW resulted in an average of 1200 (± 40)-fold increase in the ensemble fluorescence intensity compared to streptavidin-800CW (Figure 2C). Significant signal enhancement was achieved by using a relatively low concentration of the plasmonic-fluors (76 pM). To further validate the plasmonic enhancement of fluorescence, we employed “off-resonant” gold nanoparticle (AuNP) with similar surface area as the “on resonant” AuNR (7850 nm²/AuNP; 8064 nm²/AuNR) (Figure S10). The AuNPs exhibited LSPR wavelength around 530 nm, which was “off-resonant” with respect to the excitation laser (785 nm) and 800CW emission (800 nm) (Figure 2D). It is known that a large overlap between LSPR band of the plasmonic nanostructures and the excitation and emission bands of the fluorophores is critical for maximizing the fluorescence enhancement.⁴⁵ Not surprisingly, AuNP-plasmonic-fluor-800CW resulted in only 18-fold enhancement in the fluorescence intensity, which is ~ 70 -fold lower than that obtained with AuNR-plasmonic-fluor-800CW, confirming the plasmonically enhanced fluorescence (Figure 2D).

Our group and others have shown that an optimal distance between the metal surface and fluorophore is critical to maximize fluorescence enhancement by balancing the two opposing factors, namely, enhanced electromagnetic field and non-radiative energy transfer.^{35, 47-52} Fluorescence enhancement of plasmonic-fluor-800CW with different thicknesses of the dielectric spacer (MPTMS, APTMS, and TMPS) was investigated by binding them to a substrate coated with streptavidin-

800CW. The ensemble fluorescence enhancement factor (defined as the ratio of fluorescence intensities obtained after and before the addition of plasmonic-fluors on a surface coated with fluorophore-conjugated streptavidin) of the plasmonic-fluors without polymer spacer layer was found to be $\sim 146 \pm 81$. Enhancement efficiency progressively increased to $\sim 1200 (\pm 40)$ -fold with the increase of the spacer thickness (Figure 2E). Notably, the colloidal solution of plasmonic-fluor exhibited stable fluorescence signal after storage in the dark at 4°C for one month (Figure 2F). For further ease of storage, transportation, and handling, the plasmonic-fluors can be lyophilized and reconstituted as needed without noticeable degradation in the fluorescence signal (Figure 2F).

5.2.2 Plasmonic-fluor enhanced fluorescence-linked immunosorbent assay (p-FLISA) and multiplexed bead-based assay

Of the numerous applications of plasmonic-fluors, we first set out to demonstrate plasmon-enhanced fluorophore-linked immunosorbent assay (p-FLISA) implemented on a standard microtiter plate. Human interleukin 6 (IL-6), a pro-inflammatory cytokine, was employed as a representative protein biomarker. Conventional FLISA involves a standard sandwich format of capture antibody, analyte (IL-6), biotinylated detection antibody, followed by exposure to streptavidin-fluorophore (800CW in this study) (Figure 3A). In p-FLISA, plasmonic-fluor-800CW is introduced after the last step as the signal enhancer (Figure 3A). To determine the improvement in sensitivity and limit-of-detection ((LOD), defined as $\text{mean} + 3\sigma$ of the blank), serial dilutions of IL-6 of known concentration (6 ng/ml to 6 fg/ml, in 1% BSA buffered with phosphate buffered saline (PBS)) were employed as standards. Fluorescence signal obtained after applying the plasmonic-fluor-800CW revealed nearly 1440-fold enhancement in the ensemble fluorescence intensity compared to the conventional FLISA at the highest analyte concentration tested here (6 ng/ml) (Figure 3B, C, and S12). The LOD of conventional FLISA was calculated to be ~ 95 pg/ml (Figure 3D, S11,

and S12, polynomial fit). On the other hand, fluorescence signal with p-FLISA could be detected down to 20 fg/ml (~1 fM) (Figure 3E and S12, four-parameter logistic (4PL) fit), which represents a 4750-fold improvement in the LOD compared to conventional FLISA. Notably, plasmonic-fluor exhibited extremely high specificity (to streptavidin) and low non-specific binding to the interference biomolecules in the bioassays (Figure S14). We attribute this to the “BSA blocking” strategy of plasmonic-fluor, which is critical in enhancing the signal-to-background ratio. Scanning electron microscopy (SEM) images revealed an increase in the density of plasmonic-fluor-800CW at the bottom of the microtiter wells with increasing IL-6 concentration (Figure S15). Extremely low density of plasmonic-fluors was observed in the blank well, which was incubated with 1% BSA, again indicating the low non-specific binding of the plasmonic-fluors (Figure S15).

Remarkably, the LOD and lower limit of quantification ((LLOQ), defined as $\text{mean} + 10\sigma$ of the blank, ~82 fg/ml) of p-FLISA were found to be 189-fold and 120-fold lower than the “gold standard” enzyme-linked immunosorbent assay (ELISA), which involves enzymatic amplification of the colorimetric signal (Figure 3C, F, and S12). More importantly, p-FLISA exhibited a dynamic range (ratio between higher and lower limit of quantification) of five orders of magnitude, which is more than two-order-magnitude higher than that of ELISA. As a validation of the assay performance, we have tested healthy human serum samples and IL-6 spiked serum using p-FLISA. Serum samples were diluted by 10-fold so that only 10 μl of original sample was required for individual subjects. Concentrations of IL-6 in healthy individuals are normally in the range of 0.2-7.8 pg/ml.¹¹⁶ Increased level of IL-6 in serum can be indicative of systemic inflammatory, metabolic,

and physiological stimuli.¹¹⁶ Notably, among ELISA, FLISA and p-FLISA, only the latter technique was able to determine the IL-6 concentration in healthy individuals, which were measured to be 8.1 pg/ml, 1.8 pg/ml, and 2.8 pg/ml after dilution-fold correction (Figure 3G).

Harnessing the high sensitivity and large dynamic range, we demonstrate that p-FLISA can be employed as a powerful biomedical research tool to quantitatively analyze biomarkers in precious biofluids of extremely small volume (as low as 10 nanoliters), such as interstitial fluid (ISF). One of the existing challenges in ISF analysis is the inadequate amount of ISF that can be extracted using the existing techniques, making downstream proteomic and metabolomic analysis challenging.¹¹⁷ Here, we employed p-FLISA to measure the concentrations of a proinflammation cytokine (IL-6) in skin interstitial fluid obtained from mice immune-stimulated with lipopolysaccharide (LPS) and naïve mice (as controls). It is important to note that only an extremely small amount of ISF (less than 10 μ l) could be obtained from the entire skin from the back of the mice (\sim 6 cm²) (Figure S16A). To determine the smallest amount of sample required for p-FLISA and conventional ELISA, mouse ISF was diluted 100-fold, 1000-fold, 10,000-fold, and 100,000-fold (representing 1 μ l, 0.1 μ l, 0.01 μ l, and 0.001 μ l of ISF for each test zone, respectively) and assayed with both methods. The large dynamic range of p-FLISA enabled the detection and quantification of IL-6 concentrations in ISF samples at all the dilutions from immune-stimulated mouse (Figure S16B). Moreover, the high sensitivity of p-FLISA also enabled the detection and quantification of IL-6 concentrations in ISF from naïve mice, which was measured to be three orders of magnitude lower compared to immune-stimulated mice group (Figure S16C). Compared to p-FLISA, conventional ELISA (with \sim 100-fold inferior limit-of-detection of \sim 11.2 pg/ml) required 100-fold

larger sample volume. The IL-6 in immune-stimulated mouse ISF of high dilution (> 1000-fold) and in healthy mouse ISF cannot be detected using standard ELISA (Figure S16D).

To further demonstrate the translational potential of plasmonic-fluor in clinical diagnostic settings, we show that p-FLISA can significantly shorten the overall sample-to-answer time, making them attractive for point-of-care applications. In many pathological conditions such as acute kidney injury, myocardial infarction, and sepsis, shortening the time-to-treatment is critical to improve the clinical outcomes. The large enhancement in the fluorescence intensity and signal-to-noise ratio of p-FLISA allows us to significantly shorten the overall assay time to 20 minutes. The ultrafast p-FLISA (20-minute) exhibited the same sensitivity as the conventional ELISA (280-minute) (Figure S17A, B), in measuring the concentrations of urinary neutrophil gelatinase-associated lipocalin (NGAL), which can be elevated above normal level in patients with renal masses and kidney diseases such as acute kidney injury (AKI) and chronic kidney disease (CKD)⁵³⁻⁵⁴. The ultrafast p-FLISA was able to accurately quantify the urinary NGAL concentrations from all kidney patients with imaged renal masses and self-described healthy individuals and the assay revealed that NGAL concentrations in patients to be significantly higher (by more than 10-fold) compared to that of the healthy individuals (Figure S17C, D). Moreover, NGAL concentrations determined using 20-minute p-FLISA showed a good correlation (linear regression with $R^2=0.96$) with those acquired from the standard 280-minute ELISA, proving that the accuracy of the ultrafast assay is not compromised (Figure S17E). ELISA, when shortened to 20 minutes, showed significantly deteriorated performance, and cannot detect urinary NGAL concentrations in several patients or any of the healthy volunteers (Figure S17F).

In addition to the microtiter plate format, we have also investigated the application of plasmonic-fluors as ultrabright reporters in micro bead-based multiplexed fluoroimmunoassays, which utilize

a non-planar sampling surface. Luminex assay was employed as an example, which utilizes magnetic microbeads embedded with ratio-set fluorophores as barcode for each unique analyte (Figure 3H). The antibody conjugated microbead captures and facilitates the detection of the analyte in a typical sandwich format and is subsequently probed by streptavidin conjugated with phycoerythrin (PE), a bright fluorescent protein isolated from red algae or cyanobacteria. However, PE employed in Luminex assays is structurally unstable and prone to photobleaching.¹¹⁸ Here, Cy3, a highly stable fluorophore with absorption and emission at 554 nm and 568 nm respectively, similar to PE, was employed as a substitute. As discussed above, it is extremely important to choose plasmonic nanostructure with LSPR wavelength matching the excitation/emission of the fluorophore.⁴⁴⁻⁴⁵ To this end, we have employed AuNR@Ag nanocuboids with LSPR wavelength of 520 nm to fabricate plasmonic-fluor-Cy3 (Figure 3I, S18).¹¹⁹⁻¹²⁰ Notably, as synthesized plasmonic-fluor-Cy3 exhibited extremely high brightness and individual nanoconstructs can be easily identified under a common epifluorescence microscope (Figure S19).

We customized the Luminex assay to simultaneously detect mouse IL-6 and mouse tumor necrosis factor- α (TNF- α), which are important pro-inflammatory cytokines involved in cell signaling and immune modulation. The microbeads were incubated with a mixture of serial dilutions of TNF- α and IL-6, followed by the detection antibody cocktail, streptavidin-Cy3, and plasmonic-fluor-Cy3 (Figure 3H). The beads are subsequently read using a dual laser flow-based instrument (Luminex 200), with the classification laser (635 nm) deciphering the barcode of each bead and the reporter laser (532 nm) determining the intensity of the Cy3 fluorescence, which is in direct proportion to the amount of analyte bound (Figure 3H). SEM image of the microbead shows uniform binding of plasmonic-fluor-Cy3 with no sign of aggregation (Figure 3J). The binding of plasmonic-fluor-

Cy3 did not alter the size and shape of the bead (Figure S20) or the optical barcode signal (Figure S21). A significant increase in the microbead fluorescence intensity was observed after the binding of plasmonic-fluor-Cy3 (Figure 3K). The LODs of plasmon-enhanced mouse IL-6 and TNF- α assays were determined to be 56.6 fg/ml (2.7 fM) and 7.5 fg/ml (0.3 fM), respectively (Figure 3L, M, and S23). Compared to unenhanced counterpart (Figure 3L, M, S22, and S23), the plasmon-enhanced assay exhibited 143-fold and 814-fold lower LOD for mouse IL-6 and mouse TNF- α , respectively. Notably, the vendor-specified LOD (using PE-streptavidin) for mouse IL-6 (2.3 pg/ml) and mouse TNF- α (1.47 pg/ml) were noted to be 41-fold and 196-fold inferior to the plasmon-enhanced Luminex assay. In essence, plasmonic-fluors serve as a powerful platform technology to enhance the bioanalytical parameters (LOD, LLOQ, dynamic range) of various existing immunoassays without requiring tedious steps or any specialized instruments.

5.2.3 Plasmonic-fluor enhanced high throughput multiplexed proteomic array

Biomolecular (micro-)arrays based on fluorescence read-out is an important clinical and research tool, especially for simple, high-throughput and rapid proteomic and genetic analysis, allowing miniaturization of thousands of assays on one small piece of analytical substrate.¹²¹ Despite advantages such as high multiplexity, rapid screening, and low sample volume, this methodology suffers from low sensitivity (even inferior to ELISA), which hinders its widespread application.

We have investigated the applicability of plasmonic-fluors for enhancing the sensitivity of immuno-arrays. An array of antibodies to biomarkers of human kidney disease was employed as a representative example (Figure 4A). This array is comprised of 38 capture antibodies correspond-

ing to human kidney disease protein biomarkers, printed in duplicates on a microporous nitrocellulose membrane (Figure S26). Biotinylated IgGs and PBS were printed as reference positive control and negative control, respectively (Figure S26). A human urine sample from a patient with kidney disease was diluted 10-fold using blocking buffer, mixed with biotinylated detection antibody cocktail, and added onto the nitrocellulose membrane. After incubation, the membrane was exposed to streptavidin-800CW. Finally, plasmonic-fluor-800CW suspension is added on the array, incubated, and thoroughly rinsed to remove the unbound nanoconstructs (Figure 4A).

SEM images from the positive control region revealed a uniform distribution of plasmonic-fluors on membrane (including porous subsurface regions) (Figure 4B). Concurrently, no signal was detected from the negative control (Figure 4E: blue box) and plasmonic-fluors were not observed in the SEM images from these locations, indicating their minimal non-specific binding (Figure S27). Using conventional fluorophores, out of the 38 target protein biomarkers, only 26 were detectable, most of them exhibiting weak intensity (Figure 4C, D, F and S28). After addition of the plasmonic-fluor-800CW, the fluorescence signal intensity from each spot of the protein array increased significantly (Figure 4E, G, and S28), enabling the detection and relative quantification of all of the other targets that could not be detected by the conventional fluors (Figure 4G, [+] mark indicating biomarker detected only with plasmonic-fluors). Additionally, we have employed a commercially available 40-plex cytokine microarray as another validation for plasmonic-fluor, where significant improvement in the microarray sensitivity was observed as well (Figure S31).

It is known that the plasmonic nanostructures at the LSPR wavelength exhibit large extinction cross-section, which can be up to 5-6 orders of magnitude larger than light absorption of most

organic dyes.⁷⁵ This unique property of plasmonic nanostructures renders the possibility of utilizing plasmonic-fluors as multimodal bio-label.¹²² Indeed, the binding of plasmonic-fluor to the sensing domains resulted in analyte concentration-dependent color spots, which can be directly visualized by the naked eye (Figure 4H). The color intensity of each spot in a digital photograph, acquired using a smartphone camera under ambient light condition, was analyzed and compared to the corresponding fluorescence intensity (Figure 4I). We observed a good correlation between the two acquisition modes ($R^2=0.88$, Figure S32), which indicates the potential applicability of this nanoconstruct as a “visible label” in resource-limited settings to alleviate the reliance on a dedicated and expensive readout instrument.

5.2.4 Plasmonic-fluor enhanced immunocytochemistry/immunofluorescence (ICC/IF)

Immunocytochemistry based on immunofluorescence is a well-developed semi-quantitative method for analyzing the relative abundance, conformation, and subcellular localization of target antigens in cells. Again, this method lacks the sensitivity to distinguish low abundant biomolecules from the noise level due to the feeble fluorescence signal of conventional fluorophores. Autofluorescence, the natural emission of light by biological structures, further contributes to the overall low signal-to-noise ratio.

To test the applicability of plasmonic-fluor in ICC/IF, we employed ErbB2 (human epidermal growth factor receptor 2)-positive epithelial breast cancer cells (SK-BR-3) as a model cell line. The surface receptor ErbB2 was immuno-stained using standard approach (biotinylated ErbB2 primary antibody and streptavidin-800CW), followed by the addition of plasmonic-fluor-800CW (Figure 5A). ErbB2 primary antibody (1 mg/ml) was diluted to different concentrations

before incubation with cells. SEM images revealed the uniform distribution of plasmonic-fluors on the cell membrane (Figure S33). Confocal laser scanning microscopy (CLSM) images of the cells revealed up-to 100-fold higher fluorescence signal (background subtracted) after the addition of plasmonic-fluors (20 pM) (Figure 5A, B, S34 and S35), and the expression of ErbB2 receptors could be imaged even at 100,000-fold dilution of the primary antibody (10 ng/ml) (Figure 5A, S34). In stark contrast, the fluorescence signal could only be imaged at a 100-fold (typical dilution; 10 µg/ml) dilution of primary antibody using conventional fluorophores (Figure 5A). These results demonstrate not only the applicability of plasmonic-fluor in significantly reducing the amount of antibody (and consequent cost) required in ICC/IF but also the ability to image low-abundance biomarkers on the cell surface using plasmonic-fluors.

5.2.5 Plasmonic-fluor enhanced flow cytometry measurement

Flow cytometry is extensively employed in cell analysis to measure the expression and relative abundance of specific analytes on or within the cells at rates of thousand or more cells per second (Figure 5C). However, flow cytometry also suffers from significant challenges in terms of fluorescence signal-to-noise ratio due to the high speed of the target species as they cross the laser focus, limiting the time for fluorescence readout.¹²³ Again, background fluorescence (autofluorescence) from cells poses difficulty in delineating small changes in the expression levels of intra- and extracellular targets.

To test the ability of plasmonic-fluors to enhance the signal-to-noise ratio in flow cytometry-based cell analysis (Figure 5C), SK-BR-3 cell suspensions were incubated with ErbB2 primary antibody, streptavidin-680LT, followed by the addition of plasmonic-fluor-680LT. Subsequently, the labeled cells were collected by mild centrifugation (1000 rpm) with concomitant

removal of unbound plasmonic-fluors. To match the excitation laser and fluorophore emission, we have employed AuNRs with LSPR wavelength around 647 nm as the nanoantennae to create plasmonic-fluor-680LT (Figure S38). Specific binding of the plasmonic-fluor-680LT caused a significant change in the color of the cell pellet (Figure S39). The presence of plasmonic-fluors-680LT on the cell surface did not change the forward scatter or side scatter intensity (Figure S40), indicating that the cell size and granularity/complexity remained virtually unaltered after binding of the plasmonic-fluor-680LT. Flow cytogram of fluorescence vs. forward scatter (vertically offset for clarity) of SK-BR-3 cells revealed a more obvious separation of cell populations stained with plasmonic-fluor-680LT compared to that obtained with conventional fluorophores (Figure 5D). Histograms of cell fluorescence signals revealed up-to 60-fold higher intensity (background subtracted) using plasmonic-fluor-680LT compared to its conventional counterpart (Figure 5E). Fluorescence histogram revealed that the expression of ErbB2 on the cell surface can be detected even at 200,000-fold dilution of primary antibody (5 ng/ml) using plasmonic-fluor-680LT labeling (Figure 5F, G). On the other hand, conventional labeling required the antibody to be diluted less than 1000-fold (*i.e.* concentration > 0.5 $\mu\text{g/ml}$) to ensure a detectable increase in fluorescence signal compared to the background (blank) (Figure 5F, G).

To further validate the performance of plasmonic-fluors in delineating cell populations with small differences in surface receptor expression levels, we employed bone marrow-derived dendritic cells (BMDCs) as a model system in which the surface expression of receptors can be modulated using immunogenic stimulus. Dendritic cells after exposure to an immunogenic stimulus undergo activation and maturation, which leads to cytokine secretion and upregulation of maturation markers such as CD40, CD80, CD86, MHC I and MHC II. Here, BMDCs were isolated from

6-8 weeks old C57BL/6 mice and lipopolysaccharide (LPS) was employed as immunogenic stimulus to trigger the upregulation of CD80 and cytokine release in a dose-dependent manner. Subsequently, the cells were fixed and treated with biotinylated CD80 antibody. Finally, BMDCs were probed by conventional fluorophore (680LT) followed by plasmonic-fluor-680LT, and the fluorescence levels were compared using flow cytometer (Figure 6A).

Figure 6B, C show the fluorescence histograms corresponding to naïve and LPS (0.05 µg/ml)-stimulated BMDCs obtained using conventional fluors (680LT, Figure 6B) and plasmonic-fluor-680LT (Figure 6C). Clearly, plasmonic-fluor stained BMDCs exhibited a significant fluorescence difference between activated (blue) and naïve (red) cell populations (Figure 6B, C, S43). LPS dose-dependent (0 to 0.05 µg/ml) stimulation of BMDCs was further investigated, where a steep increase in the mean fluorescence intensity was observed using plasmonic-fluor-680LT followed by plateau at higher LPS dose (Figure 6D, S44), indicating an increase in the expression of CD80. BMDCs stained with conventional fluorophore, however, exhibited a shallow fluorescence increase with LPS dose, which was obscured by the high fluorescence background (Figure 6D, and S4

4). Moreover, the secretion levels of pro-inflammatory cytokines (TNF- α and IL-12) exhibited an increasing trend with the increase of LPS concentration (Figure 6E, S45). This further confirmed the dose-dependent activation and maturation of BMDCs as well as the specificity and accuracy of plasmonic-fluor in differentiating the minute changes in the cell surface maturation markers.

5.3 Conclusions

Harnessing plasmon-enhanced fluorescence, we have designed and synthesized extremely bright nanoconstructs as fluorescence reporter. In addition to the improved bioanalytical parameters, plasmonic-fluors can potentially simplify the readout instrumentation, decrease the required sample volume, shorten the overall assay time, and enable bioassays to be implemented with minimal effort and reduced cost. Through a series of experiments, we have demonstrated that plasmonic-fluors are highly customizable in terms of the excitation/emission wavelength over the entire visible and near infrared range and can be applied in microtiter plates, on porous membranes, on microbeads, and cells. The cross-platform signal amplification approach introduced here is a disease-, biomarker-, and application-agnostic ubiquitously-applicable fundamental and enabling biomedical technology to immediately improve the sensitivity of existing bioanalytical methodologies in an easy-to-implement and cost-effective manner.

5.4. Figures

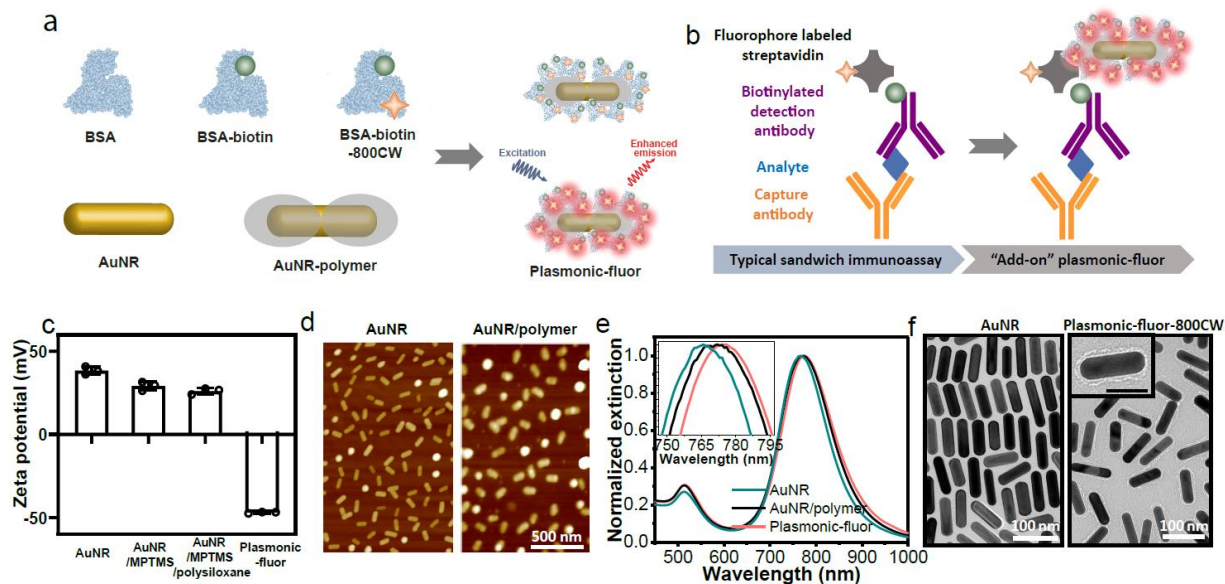


Figure 5. 1 Plasmonic-fluor synthesis and material characterization. (A) Schematic illustration showing the structure of “plasmonic-fluor”, which consists of a plasmonically-active core (*e.g.* gold nanorod (AuNR)), a polymer shell as spacer layer, light emitters, and a universal biorecognition element (biotin). BSA is employed as a key design element to assemble all components into the functional nanoconstruct and to resist non-specific binding. (B) Working principle of plasmonic-fluor as an “add-on” biolabel to enhance the fluorescence intensity and consequent signal-to-noise ratio of fluorescence-based assays, without changing the existing assay workflow. (C) Zeta potential of AuNR, AuNR/MPTMS, AuNR/MPTMS/polysiloxane (AuNR/polymer), and the plasmonic-fluor-800CW (AuNR/polymer/BSA-biotin-800CW). Error bar represents s.d. ($n=3$ repeated tests). (D) AFM images showing the AuNR before and after coating with polymer. (E) Vis-NIR extinction spectra of AuNR, AuNR/polymer, and plasmonic-fluor, showing a progressive red shift in the LSPR wavelength after each step. (F) TEM images of bare AuNR and plasmonic-fluor-800CW.

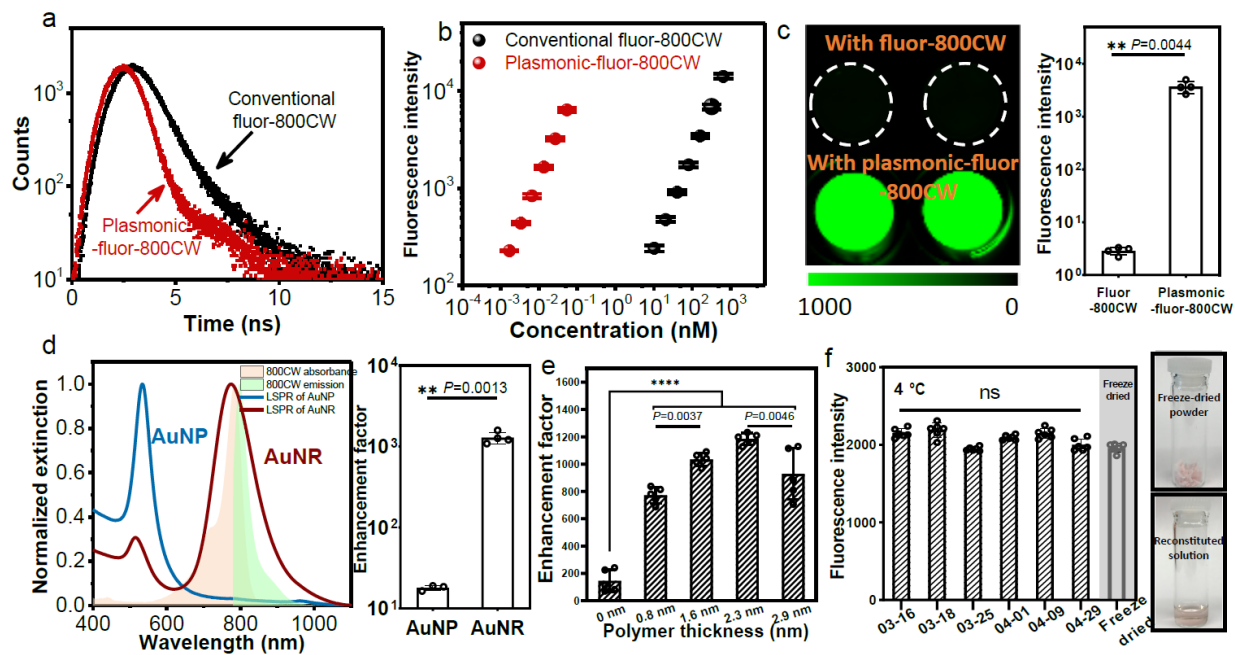


Figure 5. 2 Plasmon-enhanced fluorescence and colloidal stability of plasmonic-fluors. (A) Excited state lifetime measurements of conventional fluor (BSA-biotin-800CW) and plasmonic-fluor-800CW (AuNR/polymer/BSA-biotin-800CW) showing a significant decrease in the lifetime of 800CW after adsorption on AuNR. (B) Fluorescence intensity of conventional fluor-800CW and plasmonic-fluor-800CW at their different molar concentrations. The difference in the slopes of two curves indicates that a single plasmonic-fluor-800CW is as bright as 6700 (\pm 900) fluorophores. Error bar represents s.d. ($n=3$ repeated tests). (C) Fluorescence intensity of 800CW-streptavidin followed by the specific binding of plasmonic-fluor-800CW through biotin-streptavidin interaction, showing an average of 1200 (\pm 40)-fold increase in fluorescence intensity. Error bar represents s.d. ($n=4$ independent tests). Data statistically significant P value= 0.0044, $** P < 0.01$ by two-tailed unpaired t-test with Welch's correction. (D) Left: LSPR wavelength of gold nanoparticles (AuNPs) and AuNRs with similar surface area. Plot also shows the absorption and emission spectra of 800CW. Right: Fluorescence enhancement factor upon binding of "off-resonant" AuNP-plasmonic-fluor-800CW and "on-resonant" AuNR-plasmonic-fluor-800CW to 800CW-streptavidin. Error bar represents s.d. ($n \geq 3$ independent tests). Data statistically significant P value= 0.0013, $** P < 0.01$ by two-tailed unpaired t-test with Welch's correction. (E) Fluorescence enhancement factor obtained using plasmonic-fluor-800CW with different polymer spacer thickness. Error bar represents s.d. ($n=5$ independent tests). $**** P < 0.0001$ and $** P < 0.01$ by one-way ANOVA with Tukey's post test. (F) Left: plot showing the stability of plasmonic-fluor suspension stored at 4°C and reconstituted from lyophilized powder. Error bar represents s.d. ($n=6$ repeated tests). NS: not significant. P value > 0.9999 by one-way ANOVA with Tukey's post test. Right: Photographs depicting the lyophilized powder of plasmonic-fluor before and after reconstitution.

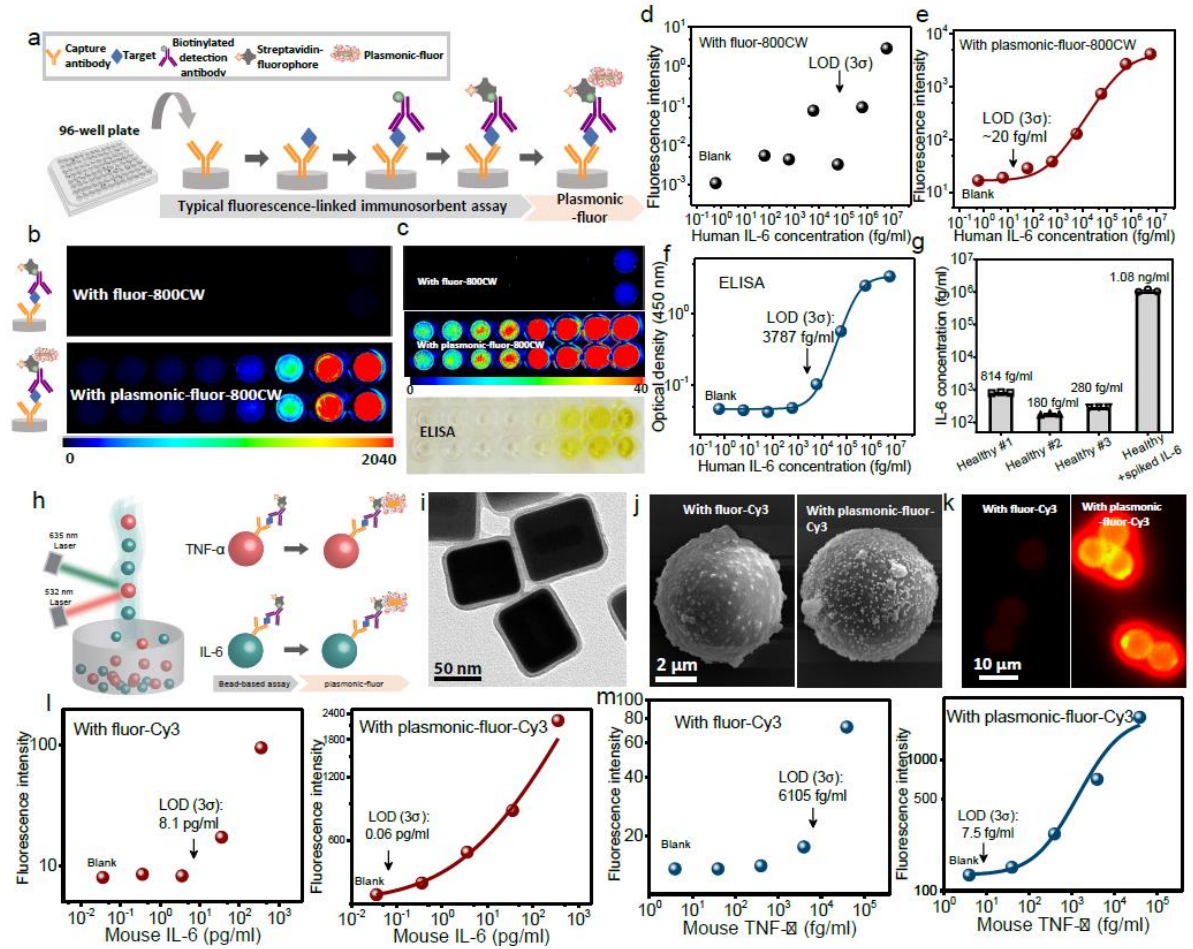


Figure 5. 3 Plasmonic-fluor enhanced fluorophore-linked immunosorbent assay (FLISA) and multiplexed bead-based immunoassay. (A) Schematic showing the concept of conventional FLISA (800CW) and plasmonic-fluor-800CW enhanced FLISA (p-FLISA), implemented in a standard 96-well plate. P-FLISA assay does not require any change in the routine workflow except adding the plasmonic-fluor as the new, last step. (B) Fluorescence intensity maps of human IL-6 FLISA and p-FLISA at various analyte concentrations. (C) Fluorescence intensity maps (with zoomed-in scale bar) of human IL-6 FLISA and p-FLISA and photograph of colorimetric signal of “gold standard” human IL-6 ELISA. Plots showing human IL-6 dose-dependent fluorescence intensity from (D) conventional FLISA and (E) p-FLISA. Compared to conventional FLISA, p-FLISA exhibits 4750-fold improvement in the limit-of-detection (LOD) and more than three-order-magnitude larger dynamic range. (F) Plot showing the standard curve of human IL-6 ELISA. Compared to ELISA, p-FLISA exhibited 189-fold lower LOD and more than two-order-magnitude larger dynamic range. (G) IL-6 concentrations in human serum samples (diluted by 10-fold) measured using p-FLISA. Error bars represent s.d. ($n=3$ repeated tests). (H) Schematic illustration showing the concept of using plasmonic-fluor-Cy3 to enhance the sensitivity of bead-based immunoassay (*e.g.*, Luminex assay). (I) TEM image of plasmonic-fluor-Cy3 utilizing AuNR@Ag as the plasmonic nanoantenna. (J) SEM and (K) fluorescence images of microbead(s) before and after being probed with plasmonic-fluor-Cy3. (L) Mouse IL-6 and (M) mouse TNF- α standard curves obtained before (left) and after (right) applying plasmonic-fluor-Cy3. All standard curves are performed independently on different days with different batches of plasmonic-fluors at least three times (data included in supporting information).

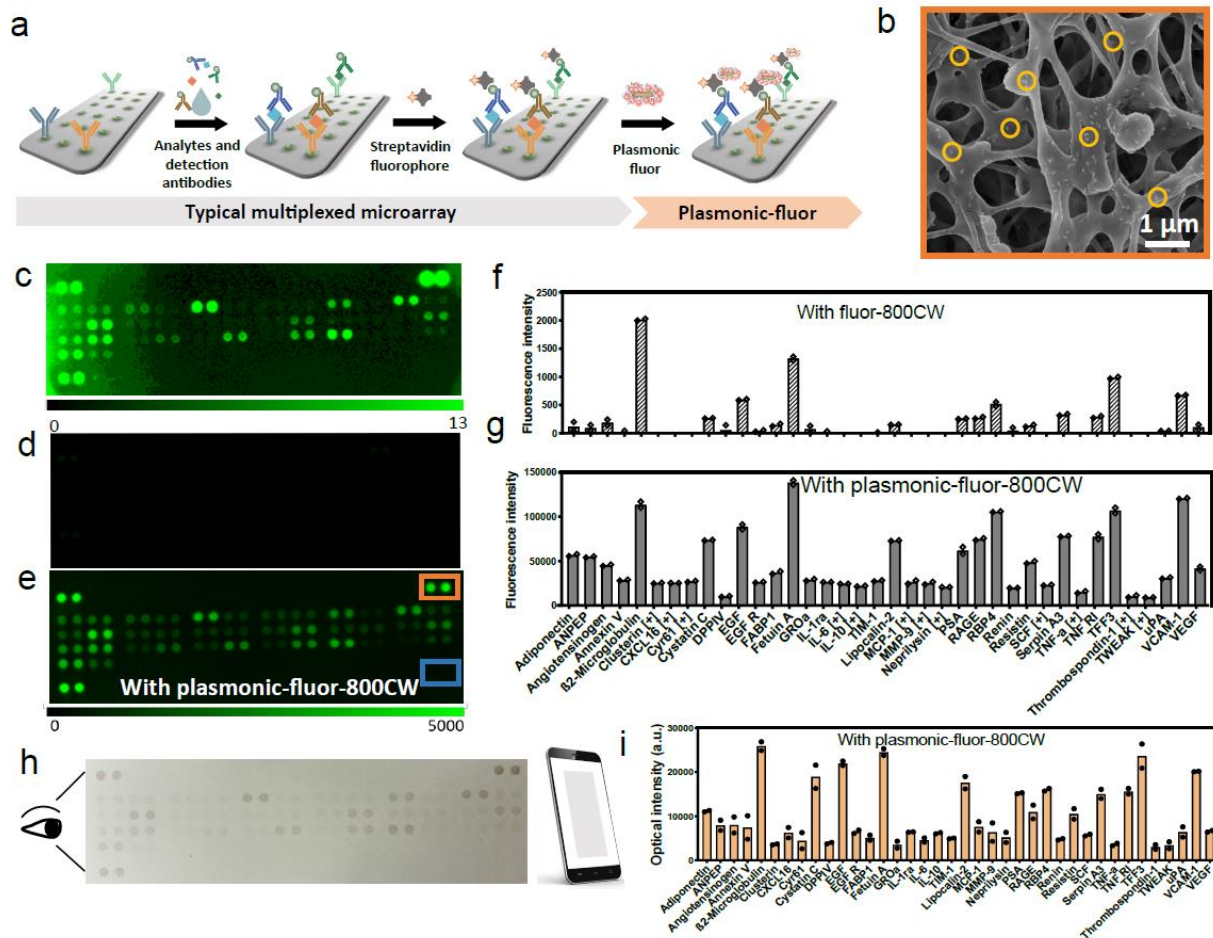


Figure 5. 4 Plasmonic-fluor enhanced high-throughput proteome profiler array. (A) Illustration showing the application of plasmonic-fluor-800CW to enhance the bioanalytical parameters of multiplexed proteome profiler for human kidney disease biomarkers implemented on a nitrocellulose membrane. (B) SEM image showing the uniform distribution of plasmonic-fluor-800CW (a few highlighted by the yellow circles) on and in subsurface regions of the nitrocellulose membrane. Fluorescence intensity map representing kidney disease protein biomarker profile of a kidney disease patient obtained (C, D) using conventional fluorophores (streptavidin-800CW) and (E) after the addition of plasmonic-fluor-800CW (note the difference in fluorescence intensity scale bar). Fluorescence intensity corresponding to the concentrations of various urinary biomarkers (F) before (typical assay using conventional fluorophore) and (G) after the addition of plasmonic-fluor-800CW. [+] indicates biomarkers detected only with plasmonic-fluor-800CW. (H) Photograph (acquired by mobile phone) showing the color change of the nitrocellulose membrane with urine sample from kidney disease patient after the addition of plasmonic-fluor-800CW. (I) Histogram showing the optical intensity of the mobile phone acquired photograph corresponding to each analyte in the patient urine sample. All error bars represent s.d. (n=2 repeated tests). Experiment was repeated three times independently on different days with different batches of plasmonic-fluors and the data is shown in supporting information.

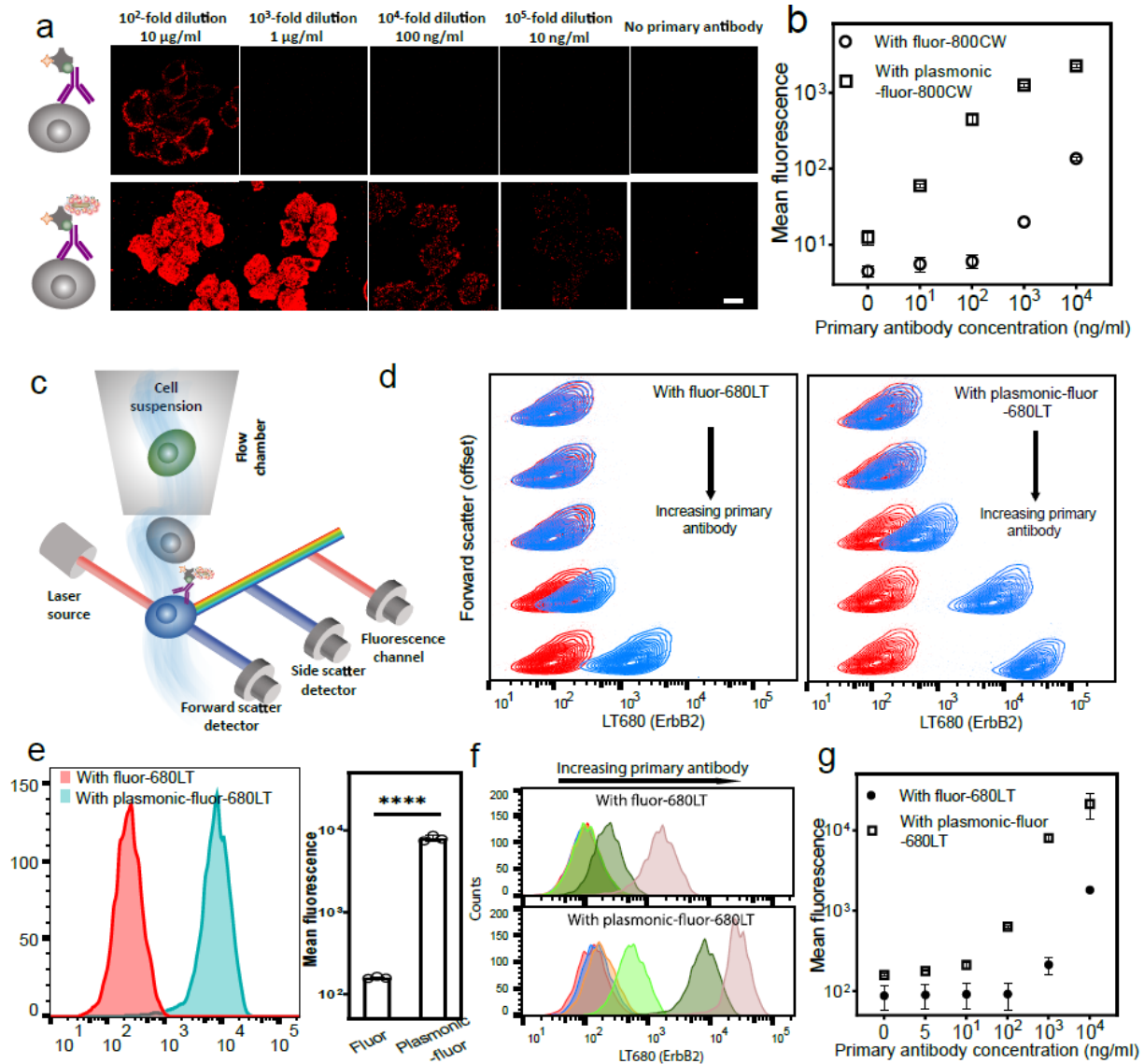


Figure 5. 5 Plasmonic-fluor enhanced immunocytochemistry and flow cytometry. (A) Confocal laser scanning microscopy (CLSM) images of breast cancer cells (SK-BR-3) probed with conventional fluor (800CW, top row) and plasmonic-fluor-800CW (bottom row) at different concentrations of ErbB2 primary antibody. Scale bar represents 10 μm. (B) Plot showing the fluorescence intensity of SK-BR-3 cells stained with conventional fluor and plasmonic-fluor-800CW. Error bars represent s.d. (over three different locations). (C) Schematic showing flow cytometry of ErbB2-stained SK-BR-3 cells probed by conventional fluor (680LT) followed with plasmonic-fluor-680LT. (D) Flow contour plot (with outliers) of fluorescence vs. forward scatter (vertically offset for clarity) of SK-BR-3 cells probed using different concentrations of ErbB2 primary antibody (Red: control group without adding primary antibody. Blue: cells treated with different dilutions of primary antibody). Cells are stained with conventional fluor (680LT, left plot) followed by the addition of plasmonic-fluor-680LT (right plot). (E) Fluorescence histogram of SK-BR-3 cells probed using conventional fluor (680LT) followed by the addition of plasmonic-fluor-680LT (at 10³-fold dilution of primary antibody). Error bars represent s.d. (n=3 independent tests). *****p* < 0.0001 by two-tailed unpaired t-test with Welch's correction. (F) Histogram showing fluorescence for SK-BR-3 cells before (top) and after (bottom) the addition of plasmonic-fluor-680LT. Red: no primary antibody; blue: 2×10⁵-fold dilution; orange: 10⁵-fold dilution; light green: 10⁴-fold dilution; green: 10³-fold dilution; rose: 10²-fold dilution of the stock solution provided by the vendor. (G)

Plot showing the mean fluorescence intensity obtained from flow cytometry at different primary antibody concentrations. Error bars represent s.d. (n=3 independent tests). All experiments were repeated three times independently on different days with different batches of plasmonic-fluors and the data is shown in supporting information.

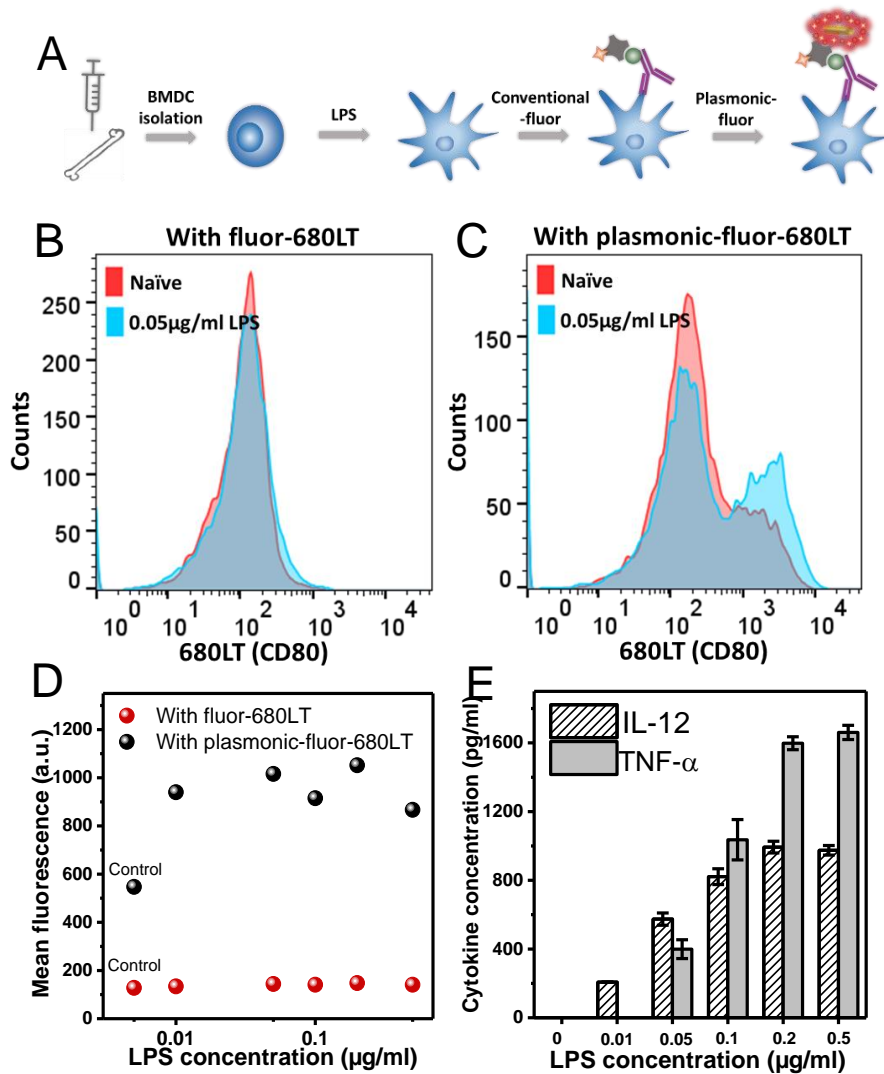


Figure 5. 6 Flow cytometry measurement of BMDC maturation maker probed by conventional fluor (680LT) and plasmonic-fluor-680LT. (A) Schematic illustration showing bone marrow derived dendritic cells (BMDCs) treated with the immuno-stimulant (lipopolysaccharide (LPS)). The small changes of maturation markers (CD80) expression after stimulation are detected by immunofluorescence staining followed by addition of plasmonic-fluor-680LT. Fluorescence intensity distribution corresponding to naïve (control) and LPS-stimulated BMDCs obtained using (B) conventional fluors (680LT) and (C) plasmonic-fluor-680LT. (D) Plot showing mean fluorescence intensity of BMDCs (corresponding to the expression level of CD80) after stimulation with different amounts of LPS. (E) Secretion levels of pro-inflammatory cytokines (TNF- α and IL-12), which confirmed the dose-dependent activation and maturation of BMDCs. Error bar represents s.d. (n=2 repeated tests). Experiment was repeated three times independently on different days with different batches of plasmonic-fluors and the data is shown in supporting information.

Chapter 6: Environmental Stability of Plasmonic Biosensors based on Natural vs. Artificial Antibody

6.1 Introduction

Accessible and affordable healthcare needs in developing countries have motivated the development of biodiagnostic devices that can be deployed in resource-limited settings. Owing to the label-free detection, high sensitivity, simple operation, and optical read-out, plasmonic biosensors based on the refractive index sensitivity of localized surface plasmon resonance (LSPR) of metal nanoparticles are considered to be highly attractive for point-of-care (POC) devices.^{9, 124-125} LSPR involves the collective oscillation of dielectrically confined conduction electrons, which results in a number of unique optical properties such as large absorption and scattering cross-sections and large enhancement of electromagnetic field surrounding metal nanostructures.¹²⁴ LSPR wavelength of noble metal nanostructures is extremely sensitive to the refractive index of the surrounding medium, and is therefore able to transduce a biomolecular binding event into a measurable shift in the LSPR wavelength.^{2, 10, 126-128}

While there has been phenomenal advances in the design and implementation of plasmonic biosensors, such as rational design of highly sensitive plasmonic nanotransducers and the development of hand-held read-out devices, the real-world translation of this class of biosensors to resource-limited settings is still hindered by the poor thermal, chemical, and environmental stability of the natural antibodies, which are the most commonly employed biorecognition elements.¹²⁹⁻¹³¹ Apart from the high cost associated with natural antibodies, biosensors relying on antibodies re-

quire stringent control of environmental conditions to maintain the structure and function (biorecognition) of the antibodies employed as biorecognition elements. Cold chain, a temperature-controlled supply chain, is typically employed to transport and store the biochips and biodiagnostic reagents. However, such expensive logistics (*i.e.*, cold chain transport and refrigerated storage is not feasible in remote areas with very limited infrastructure such as electricity and fresh water), poses a lethal challenge to the real-world deployment of biosensors relying on natural antibodies. Thus, there is an urgent need for materials and technologies that can facilitate the wide deployment of biosensors in resource-constrained areas.^{40, 129, 132}

The development of molecularly imprinted polymer (MIP) has raised promising perspectives in the design and development of sensing and separation systems that utilize artificial antibodies as recognition elements instead of natural antibodies.¹³³⁻¹³⁷ MIP involves the polymerization of functional monomers in the presence of template species, typically the target analytes. After removing the templates, the polymer is left with binding pockets that possess complementary shape and chemical functionality to template species. This binding pocket is expected to serve as an artificial antibody by providing covalent and non-covalent interactions (*e.g.*, electrostatic, hydrogen bonding, van der Waals, and hydrophobic interactions) for specific binding of the target biomolecule. Liu and co-workers have investigated the stability of molecularly imprinted microprobe and showed that it exhibited excellent stability (binding capability) even after 2-month storage under ambient conditions.¹³⁶ We have demonstrated the implementation of MIP on plasmonic nanostructures such as gold nanorods and nanocages for the label-free detection of various bioanalytes.³⁴⁻³⁵ More recently, we have demonstrated methods (PEGylation of non-cavity regions and rationale choice of functional monomers) to improve the sensitivity and selectivity of the plasmonic biosen-

sors based on these artificial antibodies.^{34-35, 138} While all of these earlier efforts establish plasmonic biosensors based on artificial antibodies as a viable platform for POC and resource-limited settings, there have been no reports that systematically investigate the stability of artificial antibodies in comparison to their natural counterparts.

In this study, we compare the stability of artificial and natural antibodies using plasmonic nanostructures as model transducers. We demonstrate that artificial antibody-based plasmonic biosensors exhibit prolonged shelf-life and excellent thermal and pH stability compared to their natural counterparts. The remarkable stability of artificial antibodies eliminates the need for cold chain transportation and refrigerated storage and handling of the biosensors. The clinical application of artificial antibody-based biosensors subjected to extreme environmental conditions is demonstrated using kidney injury molecule-1 (KIM-1), a representative urinary biomarker for acute kidney injury (AKI) and chronic kidney disease (CKD).

Compared with solid plasmonic nanostructures, hollow structures such as gold nanocages, nanoshells, nanoframes, and nanorattles (AuNRT) exhibit a much higher refractive index sensitivity. The higher refractive index sensitivity makes them excellent candidates as plasmonic nanotransducers.¹³⁹ Here, gold nanorattle (AuNRT), a hollow core-shell nanostructure made of gold nanosphere core and porous gold shell, was used as plasmonic nanotransducer.¹²⁰ AuNRT synthesis involves the galvanic replacement of silver with gold in Au@Ag core-shell nanocubes.^{120,}¹³⁸ The LSPR wavelength of AuNRT was highly tunable and could be controlled by the amount of Au precursor (HAuCl_4) added to the Au@Ag nanocube suspension. TEM images of AuNRT revealed the yolk-shell nanocube structures with sharp corners (Figure 1A). The edge length and side wall thickness of AuNRT were measured to be 38.4 ± 1.7 nm ($n > 30$) and 3.8 ± 0.4 nm ($n > 30$)

respectively, which signify the narrow size distribution of the AuNRT. UV-vis extinction spectrum of aqueous suspension of the AuNRT exhibited an LSPR wavelength of ~650 nm (Figure 1B).

6.2 Results and discussion:

Molecular imprinting on the surface of the AuNRTs involves multiple steps as illustrated in Figure 2A.³⁴ As a proof-of-concept, we first employ hemoglobin (Hb) as the model template protein. AuNRTs are first modified with p-aminothiophenol (p-ATP) and glutaraldehyde (GA), which serve as molecular linkers to bind protein template hemoglobin (Hb) to the surface of AuNRT by forming a reversible imine bond. Subsequently, organosilane monomers (TMPS and APTMS) are copolymerized around the AuNRT conjugated with Hb. We have employed silane-based monomers as they offer distinct advantages: (i) a wide variety of organosilanes with different functional groups are readily available providing a variety of non-covalent interactions between the template and the functional monomer; (ii) the polymerization is relatively simple and can be well-controlled to realize either surface or bulk imprinting; (iii) owing to the non-covalent (weak) interactions of the polymer network and the template molecules, the removal of the biomolecules after the polymerization is relatively easy; (iv) the polymerization can be performed in aqueous medium, preserving the native state of the biomolecules being employed as templates during the polymerization; and (v) more importantly, the imprints in polysiloxanes are stable compared to those in soft gels such as polyacrylamide that are prone to swelling and loss of recognition ability.¹⁴⁰

During the copolymerization process, the methoxy group of TMPS and APTMS undergo a rapid hydrolysis and subsequent condensation to form a thin layer of polysiloxane network connected

by the siloxane bonds, leaving functional end groups ($-\text{NH}_3^+$, $-\text{OH}$, $-\text{CH}_3$) interacting with hemoglobin through electrostatic, hydrogen bonding, and hydrophobic interactions. The template hemoglobin is subsequently removed from the polymer matrix by exposure to sodium dodecyl sulfate (SDS) and oxalic acid. Finally, AuNRT is left with a thin layer of siloxane copolymer with molecular cavities (imprints), which possess complementary shape and chemical functionality to hemoglobin (template and target). Each step is monitored by obtaining UV-vis spectrum of AuNRT. We noticed a progressive red shift in the LSPR wavelength (~ 18 nm in total) of the AuNRT along the imprinting process (formation of molecular linker layer, immobilization of Hb, and polymerization) and a subsequent blue shift (~ 5.5 nm) after the template release (Figure 2B and Figure S1). The sensitivity of the artificial antibody-based biosensor was monitored by measuring the LSPR shift after exposing the biochip to analyte solution containing different concentrations of Hb. The LSPR shift of artificial antibody-based biosensor exhibited monotonic increase with increase in Hb concentration. The LSPR shift essentially plateaued at concentrations higher than $1 \mu\text{g/ml}$ indicating that the recognition elements have been essentially saturated with the target analytes (Figure 2C). We employed the saturation concentration of hemoglobin ($1 \mu\text{g/ml}$) for the quantification of the bioactivity of the artificial antibody in the following experiments.

As mentioned above, we compared the stability of plasmonic biosensor based on artificial antibodies with that of natural antibodies. In the case of natural antibody-based LSPR biosensor, commercially available polyclonal anti-hemoglobin antibody was employed as the biorecognition element. The anti-hemoglobin antibody was first conjugated with thiol-PEG-COOH (MW=5000) using carbodiimide coupling chemistry and then covalently conjugated to the AuNRT surface through the SH-Au linkage (Figure 3A).¹¹ The successful conjugation of anti-Hb onto the AuNRT was evidenced by a ~ 6 nm red shift in the LSPR wavelength (Figure 3B). The bioconjugated

AuNRTs were immobilized on a glass substrate and exposed to different concentrations of Hb. Notably, the natural antibody-based biosensor (Figure 3C) exhibited a significantly higher LSPR shift and a lower limit of detection (1 ng/ml) compared to its artificial counterpart (Figure 2C). The higher sensitivity of the natural antibody biosensor could be attributed to the higher binding affinity of the natural antibody to the antigen compared to that of the artificial antibody.¹⁴¹ Considering the highest LSPR shift for natural antibody-based biosensor occurred at a concentration of 5 $\mu\text{g/ml}$, we have employed this concentration to quantify its retained activity in the subsequent experiments.

Next, we set out to test the stability of the natural and artificial antibodies after subjecting them to harsh storage conditions. To advance plasmonic biosensors to the real world, especially resource-limited settings, several environmental conditions must be considered. To understand the temporal stability (shelf-life) of the plasmonic biosensors under non-refrigerated storage conditions, we stored the plasmonic biochips (with natural and artificial recognition elements) for various time periods at room temperature ($\sim 25^\circ\text{C}$) in dry state. Subsequently, the biosensors were exposed to analyte solution and the LSPR shifts were measured. As noted above, Hb concentrations were 1 $\mu\text{g/ml}$ for artificial antibody and 5 $\mu\text{g/ml}$ for natural antibody (concentrations resulting in highest LSPR shift) based biosensors. The retained recognition capability was calculated as the percentage of the LSPR redshift upon binding of target protein to recognition element on the biochip after being challenged with various storage conditions (different storage period, temperature, and pH) compared with the redshift obtained from the same batch of freshly made substrate. Therefore, the retained biorecognition activity of biochip after subjecting to certain storage condition is expected to be linearly related to the observed LSPR shift. Different time intervals (1 day, 3 days, 1 week and 2 weeks) were selected to test the performance of artificial and natural antibody biosensors.

The retained recognition ability for natural antibody-based biosensor quickly dropped to 40% after storage for 24 hours and further decreased to less than 10% after storage for 7 days, implying a significant and rapid loss in the structure and recognition ability of the natural antibody under ambient storage conditions (Figure 4A). On the contrary, artificial antibody-based biosensors exhibited a stable LSPR response with fully retained recognition ability over two weeks of storage (Figure 4A). Notably, even after three months of storage, the artificial antibody-based biosensor exhibited nearly 85% recognition capability, signifying the remarkable stability of artificial antibodies compared to their natural counterparts (Figure S2).

We further tested the sensitivity of the biosensors based on natural and artificial antibodies stored for 7 days under different concentrations of Hb. For a wide range of Hb concentrations, the artificial antibody-based biosensor exhibited LSPR shifts closely matching a freshly prepared biosensor, indicating excellent preservation of the sensitivity (Figure 4B). In stark contrast, the LSPR shift of natural antibody-based biosensor at 5 ng/ml hemoglobin is almost completely (97%) lost after one-week storage (Figure S3). For lower concentrations, the natural antibody biosensor exhibited slight blue shifts, which might be due to the partial dissociation of antibody from the AuNRT surface. Based on these results, we conclude that although the plasmonic biosensors based on artificial antibodies exhibit inferior sensitivity compared to those based on natural antibodies, the biorecognition ability of artificial antibody-based biosensor after prolonged storage is far superior, making them better candidates for resource-limited settings.

To further investigate the stability of the antibodies, we stored the biosensors at various temperatures (from 4 to 40° C). As is common with most proteins, antibodies are expected to denature upon exposure to high temperature and thus lose their biorecognition capability due to the disruption of the secondary and tertiary structure. Both natural and artificial antibody-based biosensors

were sealed and stored at different temperatures for 14 hours. Subsequently, the biosensors were exposed to analyte (Hb) solutions (1 $\mu\text{g/ml}$ for artificial antibody, 5 $\mu\text{g/ml}$ for natural antibody) and LSPR shifts were measured. Retained recognition abilities were calculated in the same way as mentioned above. The artificial antibody-based plasmonic biochip showed a remarkable thermal stability with $\sim 100\%$ recognition ability for all temperatures tested (Figure 4C). The slightly higher LSPR shift ($\sim 10\%$) after storing the artificial antibodies at 30 and 40°C is due possibly to the annealing of the siloxane copolymer, which improves the binding affinity. Conversely, natural antibody lost nearly 50% of its biorecognition ability after storage at 10-40°C for 14 hours. Even storage under refrigerated condition (4°C) resulted in only 85% of the biorecognition ability compared to nearly 100% retained sensitivity of the biosensor based on artificial antibodies (Figure 4C). Overall, these results demonstrate the poor shelf-life stability of plasmonic biosensors based on natural antibody and highlight the advantages of the artificial recognition elements for plasmonic biosensors in resource-limited settings.

Besides the excellent thermal stability, artificial antibody-based biosensors also exhibited excellent stability against broad range of pH conditions. In resource-limited settings, pH of water used in the assay procedure is usually difficult to regulate compared to laboratory settings where deionized water or buffers with stabilized pH are employed for performing the bioassays. Furthermore, pH of the biofluids from patients, especially urine, is known to exhibit large variation (pH 4.5 to 8.5) depending on the diet and pathological conditions of the subjects. For investigating the stability of the biosensors against pH variations, the biosensors were exposed to solutions with different pH for 30 min (typical time period for washing steps) followed by exposure to the analyte solution. The artificial antibody exhibited nearly 100% recognition capability within the range from pH 3 to pH 7. Notably, natural antibody also exhibited nearly 95% retained activity after

exposure to pH 4 to 7 (Figure 4D). A significantly lower (~ 20%) activity was observed for the natural antibody-based biosensors exposed to pH 3, while artificial antibody still showed nearly 100% bioactivity under this condition.

Finally, we investigated the applicability of the artificial antibody as a biorecognition element for the detection of kidney injury molecule-1 (KIM-1), a clinically-relevant disease biomarker for acute kidney injury (AKI) and chronic kidney disease (CKD).¹⁴²⁻¹⁴³ AKI is characterized as a rapid and intensive decline of renal function, associated with high morbidity and mortality.¹⁴⁴ Nearly two million people die of AKI annually worldwide, and survivors have an enhanced risk of chronic kidney disease.¹⁴⁵ Early diagnosis and intervention in AKI could significantly improve the prognosis.¹⁴⁶ The current standard biomarker for AKI is serum creatinine, which peaks days after injury occurs. Among various urinary protein biomarkers for AKI, growing evidence shows that KIM-1 is superior for early detection of AKI, increasing within 24 hours of injury, well before serum creatinine, thereby enabling detection and potential intervention at a very early stage.^{54, 146}

The fabrication of KIM-1 artificial antibody-based biosensor is similar to that of Hb as described above except that KIM-1, instead of Hb, is used as the template protein in the molecular imprinting process. Due to the lower molecular weight of KIM-1 (Mw~30KDa) compared with Hb (Mw~64KDa), polymerization conditions were slightly modified to form a thinner layer of siloxane copolymer around the KIM-1 template, which subsequently ensured efficient release of the template proteins. The thickness of the polymer was controlled by the amount of monomer (APTMS and TMPS) added to the polymerization solution. UV-vis extinction spectra obtained after each step during the imprinting of KIM-1 revealed a continuous red shift of the LSPR wavelength (Figure 5A). Subsequently, template was released using a mixture of SDS and oxalic acid, resulting in a blue shift in the LSPR wavelength (step 3-4 in Figure 5B). The artificial antibody-

based biochips exhibited a monotonic increase in the LSPR shift with increasing concentrations of KIM-1 (Figure 5C). The detection limit was found to be 10 ng/ml (Figure 5C). We chose the saturation concentration (500 ng/ml) to investigate the stability of the plasmonic biochip. The biochip exhibited nearly 100% recognition ability after storage for three weeks at room temperature (Figure 5D). No significant loss of bioactivity was noted upon exposure to temperatures ranging from -20°C to 40°C for 14 hours (Figure 5E). The biosensor also exhibited remarkable stability against exposure to wide range of pH conditions (Figure 5F). Apart from the generality of the artificial antibody as the recognition element for various protein biomarkers, these results also demonstrate the excellent stability of a clinically-relevant artificial antibody-based biosensor for applications in point-of-care and resource-limited settings.

6.3 Conclusion:

In summary, we have demonstrated the excellent thermal, temporal, and chemical stability of the artificial antibody-based plasmonic biosensors. Compared to its natural counterpart, the artificial antibody-based biochip offers significantly superior recognition ability after being challenged with elevated temperatures, prolonged storage periods and a wide range of pH conditions (more than 90% retained activity). The superior stability of this class of sensors makes them excellent candidates in resource-limited settings such as at-home care, rural clinics, developing countries with low and moderate incomes and battlefield, where refrigeration and tight regulation of environmental conditions is not always possible. Furthermore, artificial antibodies for a new target analyte can be developed and tested more rapidly compared to natural antibodies, which is critical for

rapidly responding to public health emergencies (*e.g.*, infectious diseases) in resource-limited settings. Overall, we expect the high stability of the artificial antibody to greatly facilitate the application of plasmonic biosensors as simple, portable, sensitive, and stable on-chip biodiagnostics.

6.4 Experimental section:

Apparatus: Transmission electron microscopy (TEM) micrographs were recorded on a JEM-2100F (JEOL) field emission instrument operating at an accelerating voltage of 200 kV (JEOL USA, Inc). TEM sample was prepared by drying 2 μ L of twice centrifuged AuNRT solution on a carbon-coated TEM grid. Shimadzu 1800 spectrophotometer (Shimadzu, Kyoto, Japan) was employed to record the vis-NIR extinction spectrum of gold nanorattles during the molecular imprinting process and the binding of the target biomarkers.

Reagents: Cetyltrimethylammonium bromide (CTAB), MPTES ((3-Mercaptopropyl) triethoxysilane), hydrochloric acid (HCl, 1 M), ascorbic acid, silver nitrate (purity>99.99%), cetyltrimethylammonium chloride (CTAC), chloroauric acid (HAuCl₄), sodium borohydride (NaBH₄), 4-aminothiophenol (pATP), (3-aminopropyl)trimethoxysilane (APTMS), glutaraldehyde (GA), trimethoxy(propyl)silane (TMPS), hemoglobin (Mw=64.5 kDa) and polyclonal hemoglobin antibody were obtained from Sigma-Aldrich (St. Louis, USA). KIM-1 was purchased from Sino Biological (Beijing, China). 1-Ethyl-3-(3-dimethylaminopropyl) carbodiimide (EDC) and N-hydroxysuccinimide (NHS) were purchased from Thermo scientific (Waltham, MA, USA). SH-PEG-COOH (Mw=5000 g/mol) and SH-PEG-methoxy (Mw=5000 g/mol) were purchased from Jenkem Technology (Plano, TX, USA).

Synthesis of gold Nanorattle: The synthesis of gold nanorattles begins with the synthesis of gold nanospheres with a diameter of ~8 nm, which serve as the cores in the Au nanorattles.¹²⁰ Au nanospheres were made by the seed-mediated method.^{120, 147-148} To synthesize gold seeds, freshly prepared ice-cold sodium borohydride solution (10 mM, 0.6mL) was quickly injected to a mixture of chloroauric acid (10 mM, 0.25 mL) and CTAB (0.1 M, 9.75 mL) under vigorous stirring. The solution was further stirred for 10 minutes and then left undisturbed for one hour at room temperature. The growth solution was made by adding 4.5 mL ascorbic acid (100 mM) into a mixture of 6 mL chloroauric acid (0.5 mM) and 6 mL CTAC (0.2 M) under stirring. Next, the gold seed (0.3 mL) was quickly injected into the growth solution under vigorous stirring. The mixture was further stirred for 5 minutes and then kept undisturbed for 20 minutes at room temperature to form 8 nm gold nanospheres. The gold nanosphere solution was then centrifuged at 12,000 rpm for 1 hour and redispersed into a certain volume of nanopure water to achieve a final extinction of 1.2.

As synthesized gold nanospheres were then employed as the cores to direct the formation of silver nanocubes. This growth reaction was carried out at 60°C in a water bath. First, 0.2 mL gold nanosphere solution (extinction ~1.2) was mixed with 4.8 mL CTAC (20 mM). The mixture was then heated to 60°C in a water bath under stirring. After 20 minutes, 5 mL silver nitrate (2 mM), 2.5 mL CTAC (80 mM), and 2.5 mL ascorbic acid (100 mM) were injected into the mixture in sequence. The solution was kept under stirring in a dark environment at 60°C for 4 hours. After the reaction was complete, Au@Ag nanostructures were collected by centrifugation (10,000 rpm) and redispersed to 15 mL CTAC (50 mM).

Au@Ag suspension (15 mL) was heated on a hotplate with temperature set to 90 °C. Chloroauric acid (0.5 mM) was then injected (using a syringe pump) into the Au@Ag suspension at a rate of

0.5 mL/min under vigorous stirring. The injection of chloroauric acid was stopped when the localized surface plasmon resonance wavelength of the resulting nanostructures reached around 660 nm. The color of the suspension changed from yellow to dark blue, which indicated the formation of gold nanorattles. Finally, gold nanorattles were collected by centrifugation at 10,000 rpm and redispersed into 8 mL of nanopure water. The entire synthesis Au nanorattles was performed on the same day.

Absorption of Gold Nanorattles on Glass Surface: Glass substrates ($\sim 1 \times 2$ cm) were cleaned by immersing them into Piranha solution (150 mL concentrated sulfuric acid and 50 mL 30% hydrogen peroxide solution) for 40 minutes (Caution: Piranha solution is extremely dangerous and proper care needs to be executed in handling and disposal). The substrates were then rinsed thoroughly using copious amount of nanopure water and dried with nitrogen gas. Piranha cleaned glass substrates were incubated in freshly prepared MPTES ethanolic solution (1%) for one hour. After one hour, the substrates were washed extensively with ethanol followed by thorough rinsing with nanopure water. MPTES modified glass substrates were dried with nitrogen gas and used within one week. Before absorption of AuNRT on glass, AuNRT solution was centrifuged again to remove excess amount of CTAC. The pH of AuNRT solution was adjusted to 3.0 using 1M HCl. MPTES modified glass substrate was incubated with pH adjusted AuNRT solution for overnight to allow the absorption of AuNRT. The substrate was then rinsed with nanopure water and dried with nitrogen.

Molecular Imprinting of Hemoglobin: Glass substrate absorbed with AuNRT was rinsed with 100 mM aqueous solution of NaBH_4 for 10 minutes to remove CTAC from the gold surface. The substrate was then thoroughly rinsed with nanopure water and dried with nitrogen gas. 4 μL of pATP ethanolic solution (4 mM) and 4 μL of glutaraldehyde (25%) were mixed with 2 mL of 20

mM phosphate buffer (pH=8.0). The glass substrate with AuNRT was incubated in the mixture for 30 seconds and then rinsed twice with phosphate buffer. The substrate was subsequently incubated with 25 $\mu\text{g}/\text{mL}$ hemoglobin (in 20 mM phosphate buffer, pH=8.0) at 4 $^{\circ}\text{C}$ for 2.5 hours, followed by washing twice with phosphate buffer. To prepare silane-based solution for polymerization, 3 μL of TMPS and 3 μL of APTMS were added in sequence to 3 mL phosphate buffered saline (PBS, 1 \times), and the solution was thoroughly mixed by inversion. The glass substrate was incubated with the TMPS and APTMS solution for 3 minutes to allow the formation of the siloxane copolymer on the AuNRT, followed by rinsing twice with 1 \times PBS. Finally, the substrate was exposed to 2% aqueous sodium dodecyl sulfate (SDS) solution containing 10 mM oxalic acid (pH \sim 2.3) under gentle shaking for one hour to remove the template protein hemoglobin from the surface of AuNRT.

Molecular Imprinting of KIM-1: Process for KIM-1 imprinting is similar to Hb with small modifications. Briefly, after pATP and GA modification, the substrate was immersed into 5 $\mu\text{g}/\text{mL}$ of KIM-1 solution (in 20 mM phosphate buffer, pH=8.0), followed by washing twice with phosphate buffer. In the polymerization step, 1.5 μL of TMPS and 1.5 μL of APTMS were added to 3 mL of 1 \times PBS, and the polymerization time was adjusted to 1 minute.

AuNRT-anti-hemoglobin antibody (natural antibody) conjugates preparation: To a solution of SH-PEGCOOH in water (37.5 μL , 20 μM), EDC and NHS with the same molar ratio as SH-PEGCOOH were added followed by shaking for 1 h. The pH of the above reaction mixture was adjusted to 7.4 by adding 10 \times concentrated phosphate buffered saline (PBS), followed by the addition of anti-hemoglobin antibody (10 μL , 75 μM). The reaction mixture was incubated for 2 h, and then filtered to remove any byproduct during the reaction using centrifuge tube with 50 kDa filter. The final SH-PEG-antibody conjugates solution (0.75 μM) was obtained after washing with

PBS buffer (pH 7.4) twice. AuNRT-antibody conjugates solution was prepared by adding 50 μ l SH-PEG-antibody conjugates solution to 1 ml of AuNRT solution followed by incubation for 1 h. The AuNRT-anti-hemoglobin antibody conjugates were finally immobilized onto MPTES-modified glass.

6.5 Figures:

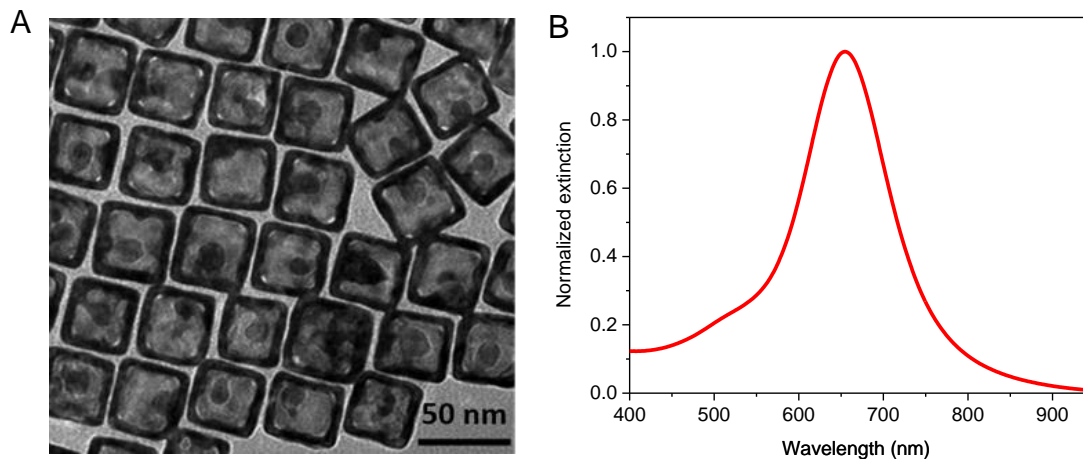


Figure 6. 1 (A) TEM image showing the core-shell structure of Au nanorattles (AuNRT) employed as the nanotransducers in plasmonic biosensors (B) Vis-NIR extinction spectrum of aqueous suspension of AuNRT.

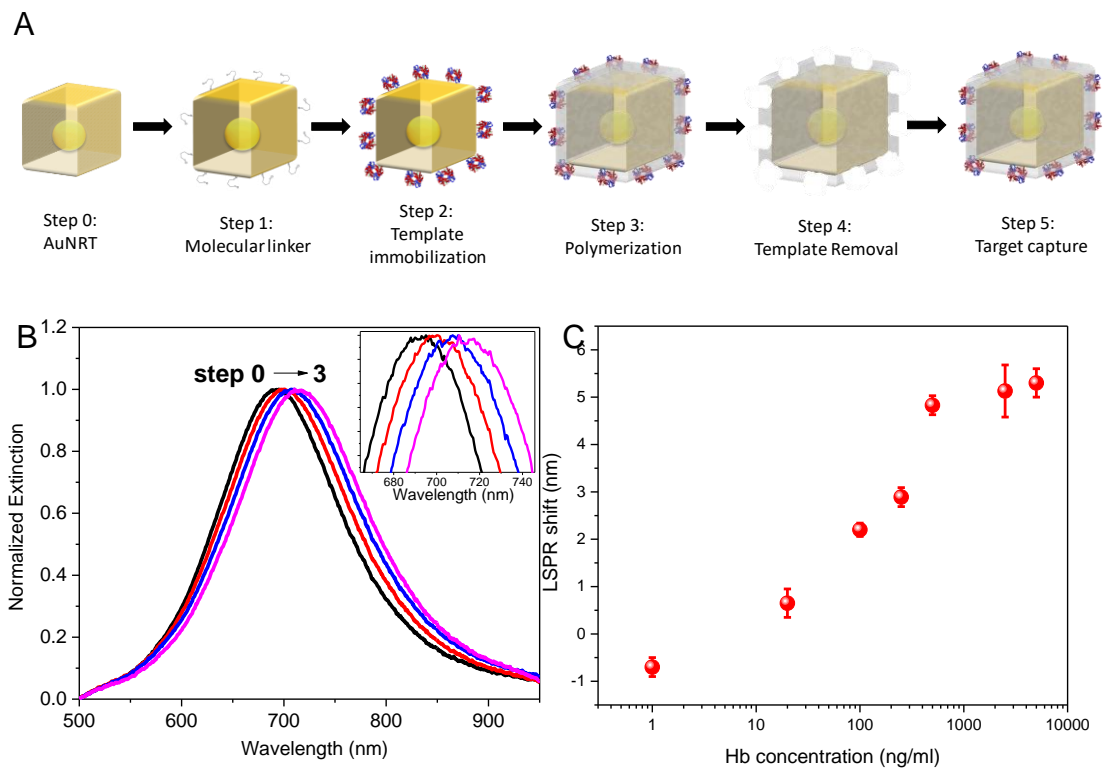


Figure 6. 2 (A) Schematic illustration showing the concept of plasmonic biosensor based on artificial antibodies as biorecognition elements. The artificial antibody is realized on AuNRT by molecular imprinting using siloxane copolymer (B) Vis-NIR extinction spectra of the AuNRT along the molecular imprinting process (inset shows zoom-in spectra highlighting the LSPR shift) (C) Plot showing the LSPR shift of AuNRT with artificial antibody (artificial anti-hemoglobin) after exposure to various concentrations of hemoglobin. Results are the mean \pm SD (n=3).

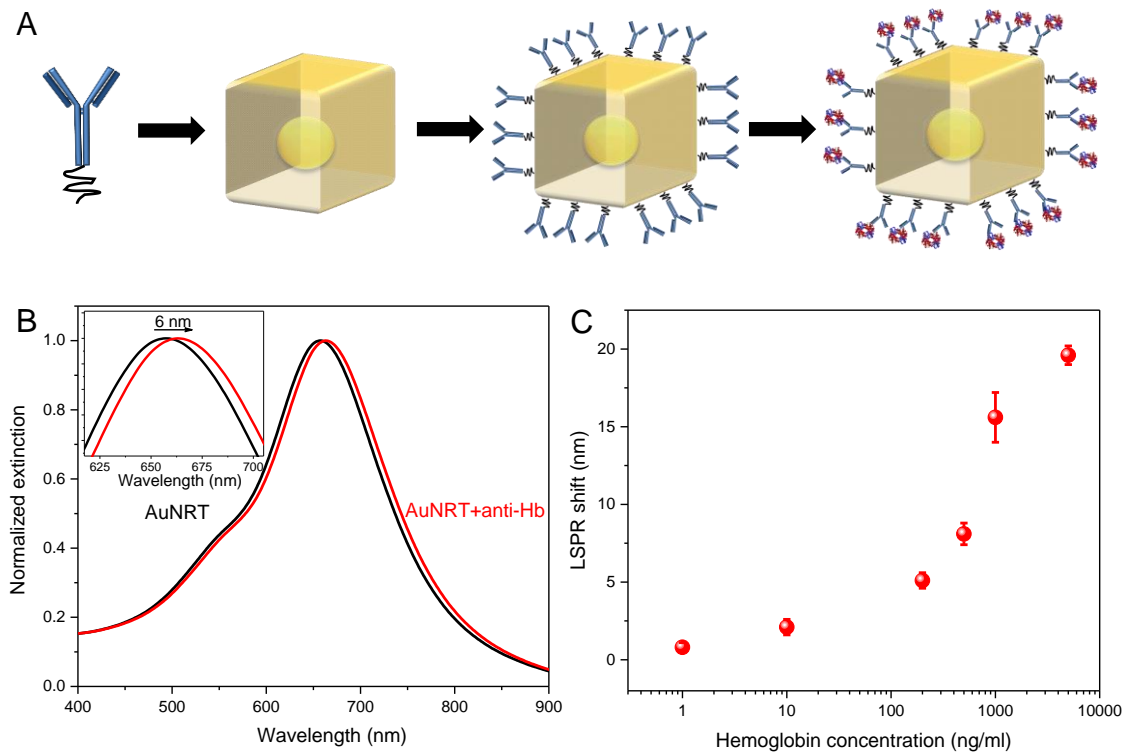


Figure 6. 3 (A) Schematic illustration representing the fabrication of plasmonic biosensor based on natural antibodies as recognition elements (B) Vis-NIR extinction spectra showing the LSPR shift of AuNRT after conjugation with natural anti-hemoglobin antibody (inset reveals the red shift in the LSPR wavelength to be 6 nm) (C) LSPR shift of plasmonic biosensor based on natural antibodies (anti-hemoglobin antibody) upon exposure to various concentrations of hemoglobin. Results are the mean \pm SD (n=3).

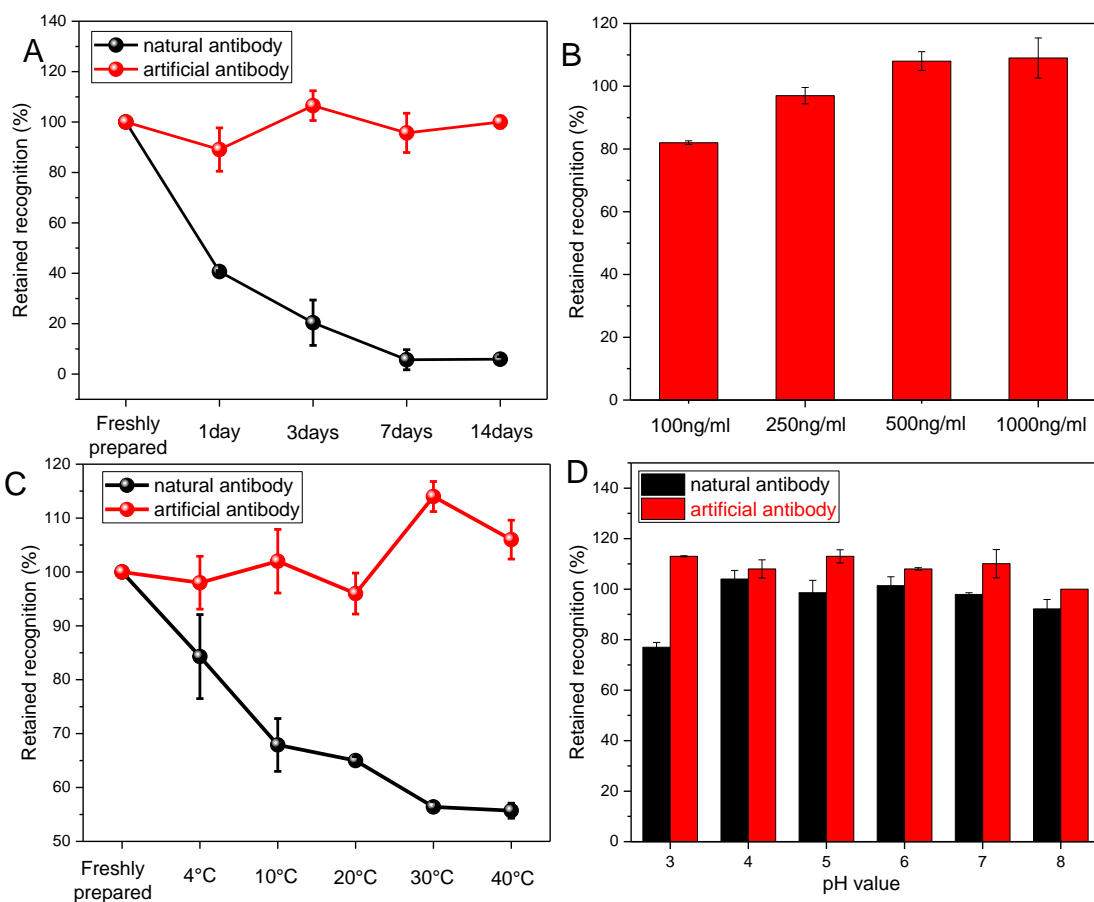


Figure 6. 4 (A) Retained recognition ability of natural and artificial antibody-based biosensor stored at room temperature for different durations. (B) Retained recognition of artificial antibody-based biosensor, as determined by exposure to various concentrations of the analyte (hemoglobin) solution, after storage at room temperature for one week (C) Retained recognition ability of natural and artificial antibody-based biosensors stored for 1 day at various temperatures and (D) Retained recognition ability of natural and artificial antibody-based biosensors after exposure to a wide range of pH conditions. Results are the mean \pm SD (n=3).

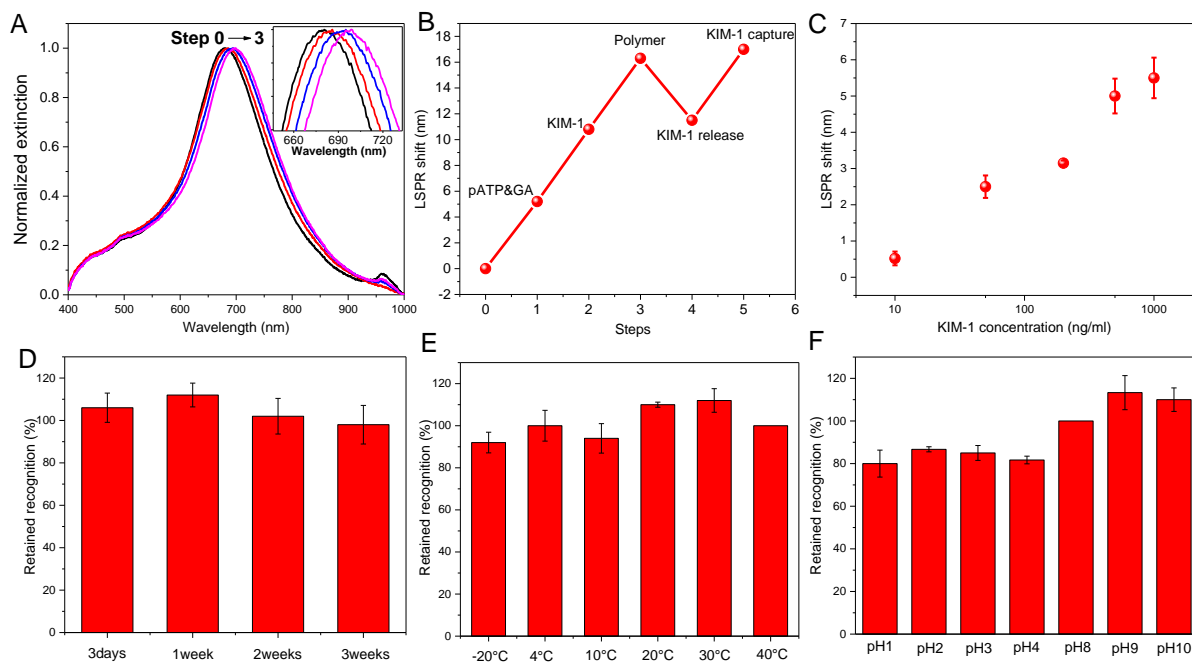


Figure 6. 5 (A) Vis-NIR extinction spectra of the AuNRT exhibiting a progressive red shift in the LSPR wavelength upon modification with pATP and GA, immobilization of KIM-1 and copolymerization of the silane monomers, (B) LSPR shift of AuNRT after each step along the formation of the artificial antibodies, template removal and template rebinding (C) LSPR shift of KIM-1-imprinted AuNRT upon exposure to various concentrations of KIM-1 solutions (D) Retained recognition ability of KIM-1 imprinted artificial antibody biosensor after storage at room temperature for different durations (E) at various temperatures for 1 day and (F) after exposure to a wide range of pH conditions. Results are the mean \pm SD (n=3).

Chapter 7: PEGylated Artificial Antibodies: Plasmonic Biosensors with Improved Selectivity

7.1 Introduction

Antibody-antigen interactions form the basis for numerous bioassays such as enzyme-linked immunosorbent assay (ELISA), Western blotting, and immunoprecipitation assay.¹⁴⁹⁻¹⁵¹ Although natural receptors (e.g., monoclonal antibodies) have excellent molecular recognition capabilities, their biological origin imposes several inherent limitations such as: (i) limited pH and temperature stability; (ii) loss of conformation and recognition functionality in non-aqueous media; (iii) high cost associated with raising and harvesting natural antibodies; and (iv) poor compatibility with micro and nanofabrication processes for efficient integration with various transduction platforms. These issues impose severe challenges in the translation of a number of biodiagnostic platforms to point-of-care and resource-limited settings^{129, 152}. Localized surface plasmon resonance (LSPR) wavelength of metal nanostructures is highly sensitive to the changes in the refractive index of the surrounding medium.¹⁵³⁻¹⁵⁴ Label-free biosensing platforms based on refractive index sensitivity of LSPR wavelength hold enormous potential to provide highly sensitive, cost-effective, on-chip, and point-of-care diagnostic tools.^{2, 155-156} However, most of the existing LSPR biosensors also rely on natural antibodies as biorecognition elements, making them prone to the abovementioned limitations.

Synthetic biorecognition elements or artificial antibodies based on molecular imprinting, which exhibit remarkable stability over a wide range of conditions (e.g., pH, temperature, solvent) are an attractive alternative to natural receptors.¹⁵⁷⁻¹⁶⁴ Artificial antibodies based on molecular imprinting

are produced by creating “binding or recognition sites” in a polymer network using target (bio)molecules as templates. The binding sites are achieved by (co-)polymerizing and cross-linking functional monomers around the template species. The template is subsequently removed by cleaving a predesigned reversible bond between the biomolecular template and the substrate. Upon removal of the template species, the polymer is left with cavities (*i.e.* binding sites), which are complementary in size, shape and chemical functionality to the template species. The imprinted binding sites can then be accessed by target analytes with the same size, shape, and chemical functionality as the template species. Recently, we have demonstrated plasmonic biosensors based on artificial antibodies using gold nanorods and nanocages as plasmonic nanotransducers.¹⁶⁵⁻

166

The sensitive (high binding affinity) and selective binding of the target molecules to the artificial receptor are the two most important criteria in creating an artificial antibody.¹⁶⁷⁻¹⁶⁹ A number of studies have focused on improving the binding affinity of the artificial antibodies through rational choice of the functional monomers and optimizing the polymerization conditions.¹⁷⁰⁻¹⁷¹ Yet another important factor that needs to be carefully considered in the design of artificial antibody-based biosensors is the non-specific binding of interfering species, which increases the noise floor of the biosensor and compromises the limit of detection. There have been only a few studies that focus on reducing the effect of non-specific binding by epitope imprinting or second polymerization.¹⁷²⁻¹⁷³ However, these methods are specific to the application and impose restrictions on the target protein or the polymerization material.

Polyethylene glycol (PEG) is a highly flexible hydrophilic polymer that is extensively used in biology and life sciences as a blocking agent to resist non-specific adsorption of proteins on implant surfaces and nanoparticles intended for biodetection, therapy and imaging.¹⁷⁴⁻¹⁷⁵ The protein-repelling effect of PEG owes to the low free energy at PEG–water interface, absence of hydrogen bonding and electrostatic interactions with proteins, and the high flexibility of PEG chains.¹⁷⁶ Although intensively studied and frequently used, to the best of our knowledge, there is no report describing the use of PEG in molecular imprinting to block the non-specific interaction. Here, we introduce a universal approach to minimize non-specific binding by blocking the non-recognition regions of the imprinted polymer with PEG before removing the template biomolecules. Successful grafting of the PEG chains on the surface of siloxane copolymer was confirmed using a series of surface characterization techniques. We demonstrate that PEG chains grafted to the non-cavity regions of imprinted polymer can greatly lower the non-specific binding of interfering proteins without perturbing the selectivity of the imprinted polymers.

7.2 Results and discussion

Hollow plasmonic nanostructures such Au nanoshells, nanocages, nanoframes and nanorattles exhibit significantly higher refractive index sensitivity compared to their solid counterparts, making them excellent choice as nanotransducers for plasmonic biosensors.¹⁷⁷ In this study, we have employed Au nanorattles (AuNRT) comprised of Au nanoparticle core and cubic and porous Au shell as nanotransducers and hemoglobin (Hb) employed as a model protein, which is the disease biomarker for hemoglobinuria. Hemoglobinuria occurs under a number of urinary tract cancers such as kidney, bladder or prostate cancers¹⁷⁸ and a wide variety of non-cancerous renal diseases in-

cluding, but not limited to, hemolytic uremic syndrome¹⁷⁹ and paroxysmal nocturnal hemoglobinuria¹⁸⁰. The concentration of hemoglobin in urine under pathological conditions can reach 600 ng/ml or more¹⁸¹. Realization of AuNRTs starts with synthesis of Au nanospheres (AuNS), which serve as seeds for Au@Ag nanocubes. AuNS were, in turn, synthesized using a seed-mediated method (see experimental section for details).¹⁸² Transmission electron microscopy (TEM) images revealed the narrow size distribution of AuNS with a diameter of 8.5 ± 0.6 nm (see SI, Figure S1). The Au@Ag nanocubes also exhibited a narrow size distribution with an edge length of 31.0 ± 1.1 nm ($n>50$). The AuNS cores were found to be at the center of each Au@Ag nanocube indicating the uniform overgrowth of Ag on the surface of the AuNS (Figure 1A). The AuNS@Ag nanocubes are dominated (100) facets due to the faster growth of Ag on the (111) facets of cuboctahedral Au nanoparticles.¹⁸³ Galvanic replacement reaction is an electrochemical reaction which involves the oxidation of one metal with lower reduction potential (which serves as a sacrificial template) by the ions of another metal with higher reduction potential.¹⁸⁴ We employed galvanic replacement reaction to synthesize AuNRT using Au@Ag nanocubes as templates. Addition of HAuCl₄ to Au@Ag nanocubes solution resulted in spontaneous galvanic replacement reaction and formation of AuNRT.^{185,186} The resultant AuNRT exhibited narrow size distribution with an edge length of 34.9 ± 1.6 nm ($n>50$) and side wall thickness of 3.9 ± 0.4 nm ($n>50$) (Figure 1B). Extinction spectrum revealed the dipolar LSPR wavelength of the Au@Ag nanocubes at 434 nm. . It has been established that the LSPR properties of the Au@Ag nanostructures are determined by the ratio of outer edge length to wall thickness. In principle, by controlling the volume of HAuCl₄ added, the LSPR peak position could be continuously shifted toward longer wavelength. In the present case, the LSPR wavelength was progressively tuned from 434nm to 694nm due to the continuous change

of the wall thickness (Figure 1C). Finally, AuNRTs with an LSPR wavelength of ~700 nm were employed in this study.

The molecular imprinting on AuNRT involved multiple steps as depicted in Figure 1D and 1E. First, p-aminothiophenol (p-ATP) and glutaraldehyde (GA) were employed as the linker to immobilize template Hb on AuNRT by forming a reversible imine bond. Trimethoxysilane (TMPS) and (3-aminopropyl) trimethoxysilane (APTMS) were then copolymerized in the presence of template protein around the AuNRT. The methoxy group of the two monomers underwent a rapid hydrolysis and subsequent condensation to form an amorphous polymer matrix, leaving functional end groups ($-\text{NH}_3^+$, $-\text{OH}$, $-\text{CH}_3$) interacting with the target protein through electrostatic, hydrogen bonding and hydrophobic interactions. Subsequently, bifunctional PEG (methoxy-PEG-silane) was covalently grafted to the free surface (*i.e.* regions not interacting with the template) of the siloxane copolymer. PEG chains were expected to shield various functional groups (NH_3^+ , $-\text{OH}$ and $-\text{CH}_3$) of siloxane copolymer, thus negating non-specific binding. The methoxysilane group of PEG underwent hydrolysis and then condensation with the reactive silanol (Si-OH) group present on the polymer surface to form a stable covalent siloxane bond (Si-O-Si) (Figure 1D). The target template protein was then removed by treating the molecular imprints with oxalic acid and sodium dodecyl sulfate (SDS), which broke the imine bond and overcame non-covalent interactions, respectively. Following the template protein removal, the AuNRT were left with siloxane copolymer coating with cavities complementary in shape and chemical functionality to the template protein. Each step described above was monitored by UV-vis extinction spectrum (described in detail later).

We have employed a series of surface characterization techniques to confirm the PEGylation of the molecular imprints. Chemical grafting of PEG chains to siloxane copolymer surface is expected to result in an increase in the refractive index of the dielectric medium surrounding AuNRT. The refractive index increase upon PEGylation is evidenced by ~2.5 nm red shift in LSPR wavelength of AuNRT (Figure 2A). PEG is known to be highly hydrophilic and grafting PEG chains to the siloxane copolymer was expected to result in improved hydrophilicity of the siloxane surface and a decrease in the contact angle of water. The contact angle of siloxane copolymer layer deposited on flat silicon substrate was found to progressively decrease with an increase in the reaction time (see Experimental for details, Figure S2). The decrease in the contact angle from ~98° to ~69° indicated the successful modification of siloxane surface with hydrophilic PEG chains. Fourier transform infrared (FTIR) spectrum of PEGylated siloxane copolymer exhibited strong bands at 1106 cm⁻¹ and 2948 cm⁻¹, corresponding to C-O-C stretching and -CH₂ stretching vibrations, respectively, which are also indicative of successful PEGylation of the surface (Figure 2B). Finally, X-ray photoelectron spectroscopy (XPS) was employed to monitor the changes in the chemical functionality at the surface of siloxane copolymer after PEGylation. Quantitative insight was obtained from C 1s peak by using curve fitting software to calculate the relative contribution of two peaks corresponding to C-C (282.5 eV) and C-O (283.1 eV) to the total carbon concentration. A significant increase in the ratio of areas under C-O peak and C-C peak from 0.36 to 0.68 confirmed the successful grafting of the PEG chains to siloxane copolymer surface (Figure 2C and D).¹⁸⁷

Now we turn our attention to the sensitivity of Hb plasmonic biosensor based on PEGylated molecular imprints. As noted above, PEG chains are grafted to the siloxane copolymer before removing the template biomolecules, which leaves the chemical functionality of the cavities intact (Figure 3A, i). Each step in the molecular imprinting process was monitored by following the LSPR shift of AuNRT (Figure 3A, ii). The accumulated red shift following various steps of imprinting process was found to be ~20 nm followed by a ~6 nm blue shift upon template protein extraction (Figure 3A, ii). The sensitivity of imprinted and PEGylated AuNRT was monitored by exposing them to different concentrations of Hb. For concentrations below 500 ng/ml, a monotonic increase in the LSPR shift of AuNRT was observed with increasing concentrations of Hb (Figure 3A, iii). The LSPR shift reached a plateau for concentrations higher than 500 ng/ml, indicating the saturation of the artificial antibodies with the target protein. To understand the influence of the PEGylation procedure, we have investigated the sensitivity of non-PEGylated imprinted AuNRT, which exhibited a similar trend *i.e.*, progressive increase in the LSPR shift followed by saturation for higher concentrations. However, non-PEGylated imprinted AuNRT exhibited slightly higher LSPR shift at the same concentration of Hb compared to PEGylated imprinted AuNRT (Figure 3A, iii). The higher LSPR shift of non-PEGylated AuNRT can be ascribed to the higher non-specific binding of the target protein to the non-cavity regions of siloxane copolymer with abundant functional groups.¹⁸⁸

Biorecognition of artificial antibodies is ascribed to complementarity of both shape and chemical functionality of the imprints to the target biomolecule.¹⁸⁹ As such, one should expect lower recognition and sensitivity if either one is perturbed or excluded. PEGylation of the siloxane copolymer layer after removing the template biomolecule should result in the passivation of both cavity and

non-cavity regions (Figure 3B, i). LSPR shifts after each imprinting step, including the PEGylation after template removal, are depicted in Figure 3B, ii. For the same concentration of the target biomolecule, the LSPR shift of fully PEGylated AuNRT was found to be significantly lower compared to AuNRT with only the non-cavity regions PEGylated (Figure 3B, iii). The significant decrease in the sensitivity of fully PEGylated AuNRT can be ascribed to (i) passivation of the entire surface with PEG chains that resist both specific (within the cavities) and non-specific binding (outside the cavities) of the proteins; and (ii) perturbation of the shape of the recognition cavities due to the grafting of the polymer chains within the cavities. The residual capturing ability and sensitivity of the cavity PEGylated plasmonic biosensor could be attributed to the partial preservation of cavity shape.

As yet another control experiment, we tested the sensitivity of AuNRT that underwent all molecular imprinting steps without template proteins and full PEGylation of the siloxane layer (Figure 3C, i). LSPR shifts after various fabrication steps are depicted in Figure 3C, ii. Notably, the PEGylation process resulted in a shift of around ~5 nm, which is considerably higher than the usual ~2.5 nm. It is known that the sensitivity of the plasmonic nanotransducer decays exponentially from the surface and the higher shift in the absence of template proteins is due to the proximity of the PEG chains to the plasmonic nanotransducer surface. An extremely small blue shift (less than 0.5 nm) was detected after exposure to oxalic acid and SDS (employed for template protein removal), indicating the absence of significant desorption of PEG chains from the siloxane copolymer surface under these conditions (Figure 3C, ii). Not surprisingly, in the absence of cavity and fully PEGylated state, the AuNRT exhibited very limited target capturing ability and the LSPR shift saturated at ~0.5 nm. Compared to AuNRT with PEGylated cavities, PEGylated AuNRT

with no cavities exhibited a huge decrease in the sensitivity and virtually complete loss of recognition capabilities. Taken together, these results clearly demonstrate the importance of complementary shape and chemical functionality of the molecular imprints for the capture of target proteins and in maximizing the sensitivity of plasmonic biosensors with artificial antibodies (Figure S3). These results also clearly highlight the importance of PEGylation of the siloxane copolymer layer before removing the template biomolecule.

We further investigated the ability of PEGylated artificial antibodies to resist non-specific binding using representative interfering proteins. LSPR shift of Hb imprinted AuNRT upon exposure to interfering proteins was employed to quantify the non-specific binding. Non-PEGylated and PEGylated AuNRT imprinted with Hb templates were exposed to bovine serum albumin (BSA) at a concentration of 10 $\mu\text{g/ml}$; a concentration equivalent to that of human serum albumin found in human urine (normal urine protein $<20 \mu\text{g/ml}$ ¹⁹⁰). While non-PEGylated AuNRTs with artificial antibodies exhibited a LSPR shift of $\sim 2.3 \text{ nm}$, PEGylated counterparts exhibited a LSPR shift of less than 0.3 nm (Figure 4A). The significantly lower LSPR shift of the PEGylated imprinted AuNRT indicates the excellent resistance to non-specific binding. Passivation of non-cavity regions using commercial blocking buffer (SuperBlock™) did not significantly improve the resistance to non-specific binding compared to non-PEGylated molecular imprints. In fact, we noted that the block proteins adsorbed on the non-cavity regions of the siloxane copolymer are dislodged from the surface during template extraction step (oxalic acid plus SDS washing) as evidenced by the large blue shift (17 nm) compared to template protein extraction (7 nm) after PEGylation (see SI, Figure S4).

To further demonstrate the improved selectivity, plasmonic biosensors based on PEGylated molecular imprints were exposed to two other urinary proteins, namely, human serum albumin (HSA) and myoglobin (Mb) at a concentration of 10 $\mu\text{g/ml}$. The two proteins exhibited different molecular weight and isoelectric points compared to Hb. As mentioned above, albumin is present in human urine. Myoglobin is a particularly challenging candidate as interfering protein for Hb imprints considering the smaller size of Mb (Mw ~ 17.5 KDa) compared to Hb (Mw ~ 64 KDa), which can readily access the imprint cavities but not normally present in urine. Additionally, myoglobin can be considered tantamount to a monomer of hemoglobin possessing similar secondary and tertiary structure to hemoglobin α and β subunits. Myoglobinuria is problematic in rhabdomyolysis due to a number of pathologic conditions and due to crush injury¹⁹¹. Concentrations of 10 $\mu\text{g/ml}$ myoglobin in urine are within the pathologic range contributing to kidney injury in humans¹⁹¹. Compared to non-PEGylated nanostructures, the PEGylated AuNRT imprinted with Hb, showed excellent resistance to (non-binding of) both HSA and Mb (Figure 4B). The LSPR shift corresponding to non-specific binding of HSA and Mb dropped from ~ 1.9 nm to ~ 0.2 nm and from ~ 1.5 nm to ~ 0.3 nm, respectively. Overall, the LSPR shift corresponding to the non-specific binding of interfering protein at a concentration of 10 $\mu\text{g/ml}$ was found to be nearly 20 times lower compared to that observed for Hb (target biomolecule) at a concentration of 1 $\mu\text{g/ml}$. To further evaluate non-specific binding, the LSPR caused by HSA was examined at several concentrations. The LSPR shift for HSA (non-specific) was found to be significantly lower compared to Hb (specific) over a broad concentration range (Figure 4C). In fact, at relatively low concentrations of HSA, we observed a small blue shift in the LSPR wavelength probably due to a small loss of organic

material (e.g., loosely crosslinked siloxane copolymer) during the incubation of the plasmonic chip in the interfering protein solution for extended durations (Figure 4C).

Finally, PEGylated and non-PEGylated AuNRT imprinted with Hb were exposed to artificial urine samples spiked with Hb (1 $\mu\text{g/ml}$). Both PEGylated and non-PEGylated AuNRT exhibited large LSRR shifts (~ 5 nm) indicating the successful recognition and capture of the target biomolecule. Conversely, when exposed to synthetic urine spiked with HSA, the non-PEGylated AuNRT exhibited a relatively large LSPR shift of ~ 2.5 nm compared to PEGylated AuNRT that exhibited a shift of ~ 0.5 nm (Figure 4D). The significantly lower LSPR shift of PEGylated AuNRT compared to non-PEGylated counterparts signifies the large reduction in the non-specific binding of albumin even from complex chemical matrix (*i.e.* synthetic urine), taking biosensors based on artificial antibodies closer to real-world applications.

7.3 Conclusions

To summarize, we demonstrated PEGylation of the non-recognition (*i.e.* non-cavity) regions of the molecular imprints as a highly efficient and broadly applicable method to reduce non-specific binding and significantly improve the selectivity of artificial antibodies. The LSPR shift of the PEGylated AuNRT was found to be nearly 10 times smaller than the non-PEGylated counterparts. Through a series of control experiments, we also demonstrated that the PEGylation process should precede template extraction to preserve the biorecognition capabilities of the molecular imprints. By simply changing the end functionality of the PEG chains, the approach demonstrated here can be broadly applied to a variety of monomers (e.g., acrylamides, acrylates) employed for molecular

imprinting. The method demonstrated here can further be broadly applied for molecularly imprinted polymers in chromatography, electrophoresis, drug delivery and biomimetic antibodies to improve the system's performance.

7.4 Figures

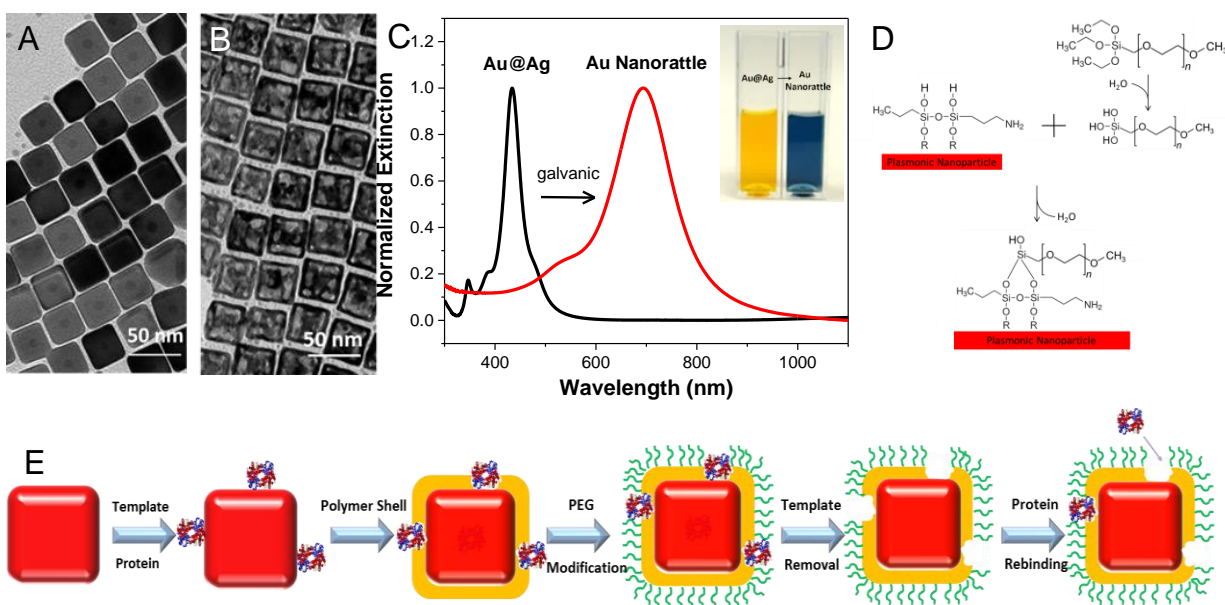


Figure 7. 1 TEM image of (A) Au@Ag nanocubes and (B) Au nanorattles. (C) Vis-NIR extinction spectra of aqueous suspension of Au@Ag nanocubes and Au nanorattles. Inset shows the photographs of the corresponding aqueous solutions (D) Schematic illustration of the chemical grafting of PEG chains to the siloxane copolymer surface (E) Schematic illustration showing the various steps involved in the formation and PEGylation of the artificial antibodies.

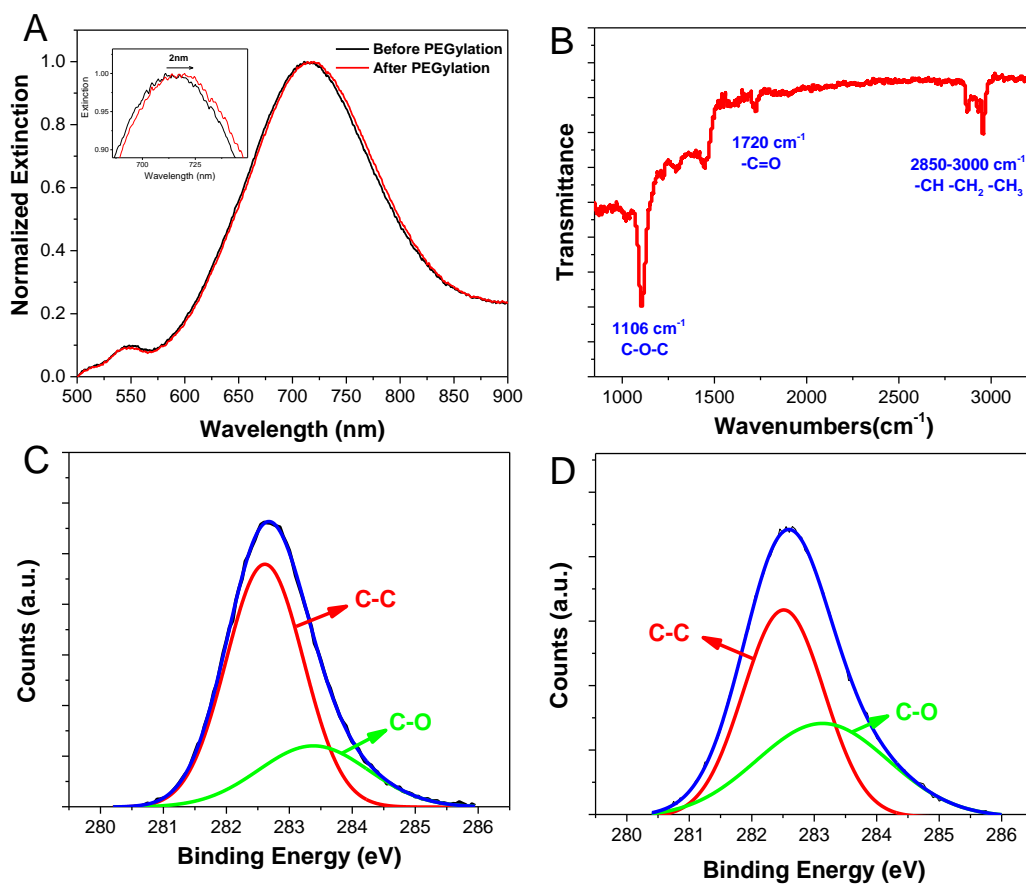


Figure 7. 2 (A) Extinction spectra of AuNRT before and after PEGylation of the siloxane copolymer surface before template extraction (Zoomed-in plot in the inset shows the ~ 2 nm red shift) (B) FTIR spectrum after PEGylation of the siloxane copolymer showing the characteristic bands corresponding to PEG. X-ray photoelectron spectra (C) before and (D) after PEGylation of the siloxane copolymer surface showing the dramatic increase in the C-O/C-C intensity ratio from 0.36 to 0.68

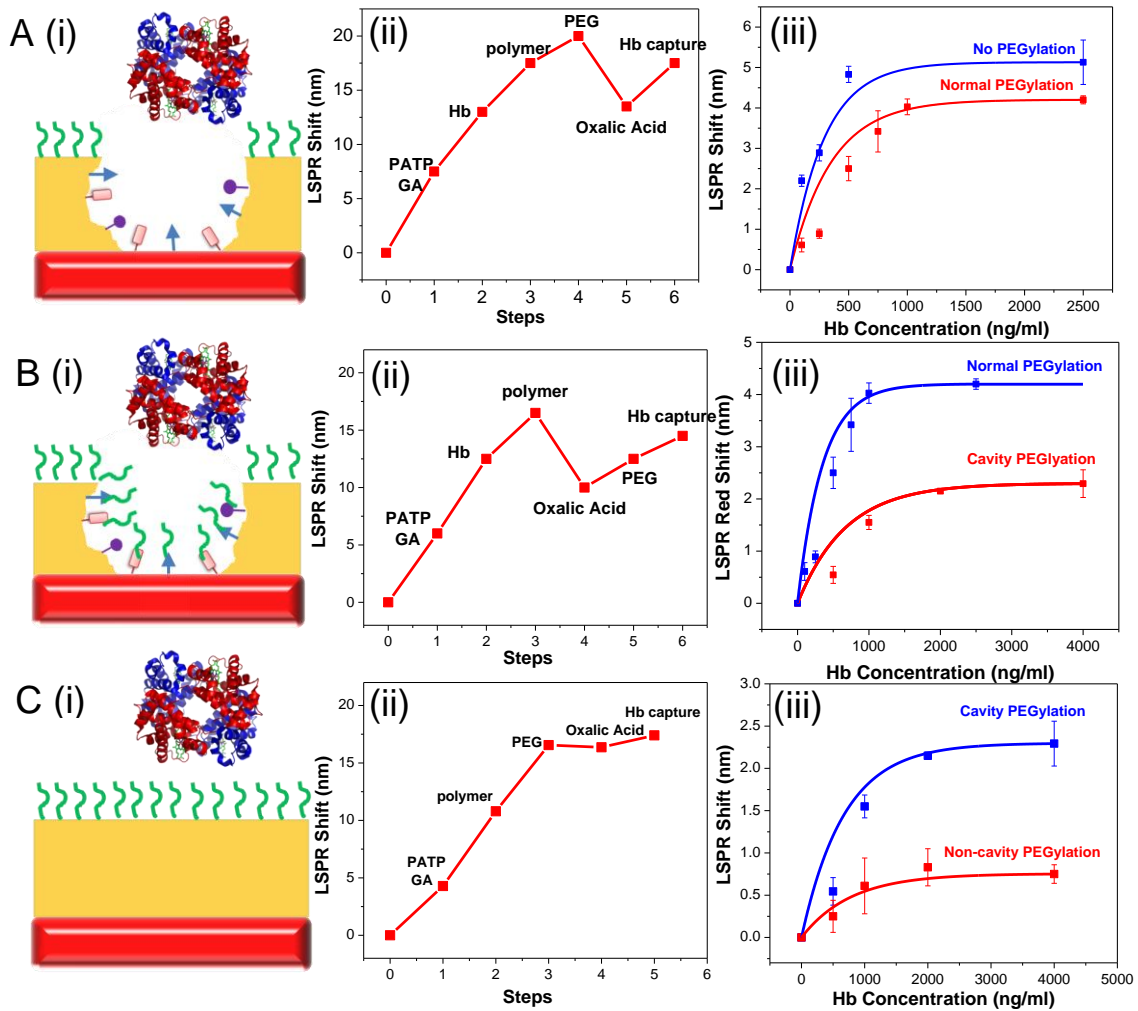


Figure 7. 3 (A) PEGylation of molecular imprinted polymer before template removal (i) schematic showing the PEGylated non-cavity regions (ii) LSPR shift of AuNRT after each step along the formation of the artificial antibodies, PEGylation, template removal and template rebinding (iii) Plot showing the LSPR shift for various concentrations of Hb (target biomarker) with and without PEGylation. (B) PEGylation of molecular imprinted polymer after template removal (i) schematic showing the PEGylated cavity and non-cavity regions (ii) LSPR shift of AuNRT after each step along the formation of the artificial antibodies, template removal, PEGylation, and template rebinding (iii) Plot showing the LSPR shift for various concentrations of Hb for artificial antibodies PEGylated before and after template removal (C) PEGylation of siloxane copolymer without template (i) schematic showing the PEGylated siloxane copolymer (ii) LSPR shift of AuNRT after each step along the formation of siloxane copolymer on AuNRT, PEGylation, and non-specific binding of proteins (iii) Plot showing the LSPR shift for various concentrations of Hb for PEGylated siloxane copolymer with and without recognition cavities.

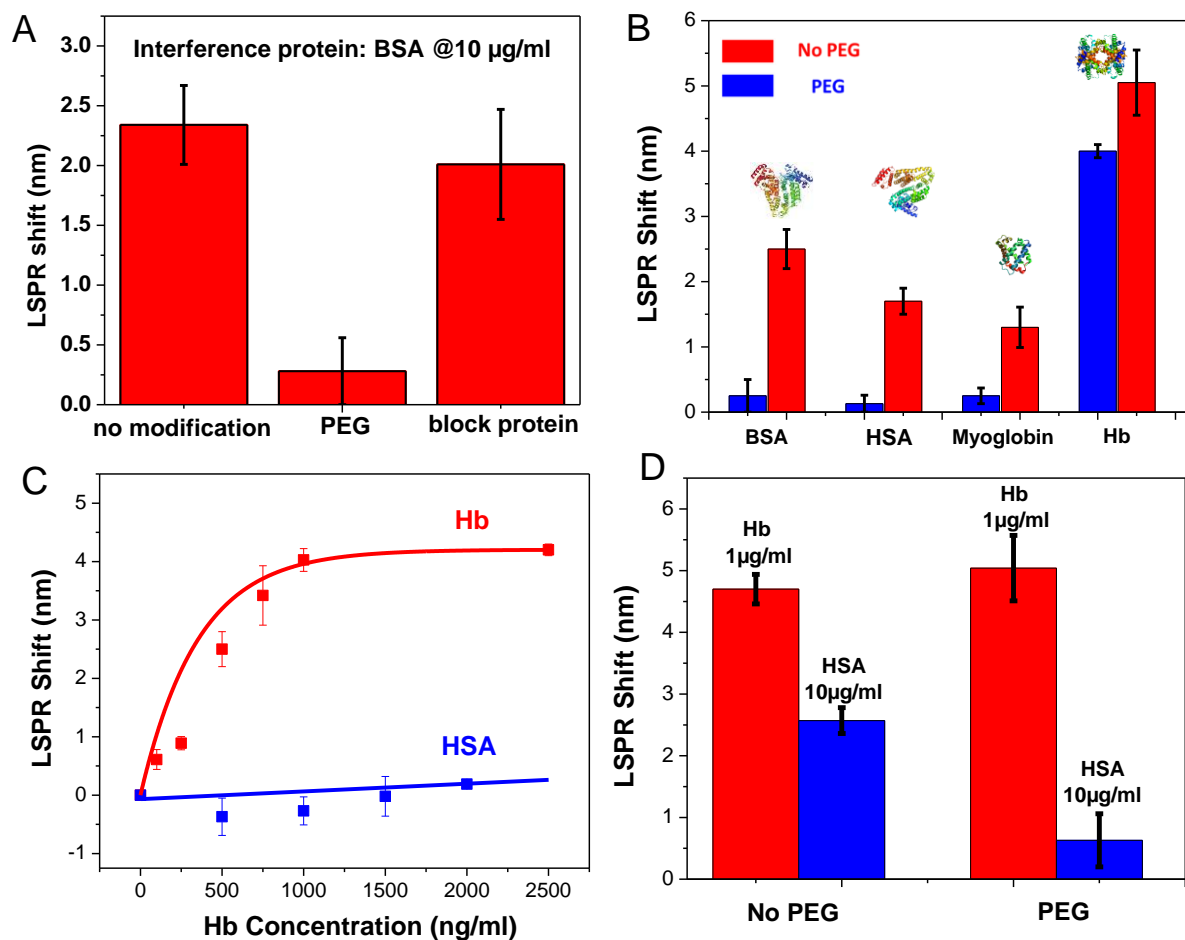


Figure 7. 4 (A) Efficiency of different blocking methods in resisting the non-specific adsorption of BSA (an interfering protein) on MIP (B) LSPR shift of PEGylated and non-PEGylated MIPs on AuNRT after exposure to various interfering proteins (blue and red column for PEGylated, no PEGylation, respectively) (C) LSPR shift vs. concentration of target (Hb) and interfering protein (HSA) depicting the excellent selectivity of the Hb-imprinted PEGylated artificial antibody (D) Improved selectivity of PEGylated plasmonic biosensor to target biomarker (Hb) from artificial urine spiked with Hb (1 µg/ml) and HSA (10 µg/ml).

Chapter 8: Aromatic functionality of target proteins influences monomer selection for creating artificial antibodies on plasmonic biosensors

8.1 Introduction

Localized surface plasmon resonance (LSPR), which involves the collective oscillation of dielectrically confined conduction electrons of metal nanostructures, is highly attractive for a number of applications including chemical and biological sensing, energy harvesting, bioimaging, and locoregional therapy.¹⁹²⁻¹⁹⁴ In particular, LSPR sensors based on the refractive index sensitivity of plasmonic nanostructures is considered to be highly attractive for on-chip and point-of-care diagnostics. Most early investigations related to plasmonic biosensors relied on natural antibodies as biorecognition elements, which exhibit excellent sensitivity and selectivity.^{9, 195} However, natural antibodies exhibit limited chemical, thermal and environmental stability, which makes them unsuitable for applications in point-of-care and resource-limited settings.¹⁹⁶⁻¹⁹⁷ For instance, natural antibodies would have to be repurchased with each new application which contributes to recurring cost. Additionally, natural antibodies lose their activity when stored at ambient or elevated temperatures.^{6, 7} We recently demonstrated plasmonic biosensors based on artificial antibodies achieved through molecular imprinting on the nanotransducer surface.¹⁹⁸⁻²⁰⁰ Artificial antibodies to a kidney injury biomarker had no change in analyte recognition over a pH range of 4.5 to 8.5 and specific gravity up to 1.03.⁹ Apart from significantly improving the stability and lowering the cost of the biosensors, use of artificial antibodies instead of the natural antibodies as biorecognition elements significantly shortens the bioassay development time as the synthetic imprinting approach can be rapidly applied to a broad class of biomolecules. For instance, it takes months to

generate and characterize a natural antibody be it polyclonal or monoclonal versus the just days to a week to prepare and characterize an artificial antibody. However, the sensitivity and selectivity of the existing artificial antibody-based plasmonic biosensors is typically lower compared to those based on natural antibodies. Overcoming the limited sensitivity and selectivity of the artificial antibody-based plasmonic biosensors is critical to translate this powerful class of biosensors to real-world clinical applications.

Artificial antibodies based on molecular imprinting rely on complementarity in size, shape and chemical functionality of the binding pocket to the target biomolecule.²⁰¹⁻²⁰² In a typical procedure, functional monomers are polymerized on the transducers in the presence of the template biomolecules. Subsequent removal of the template biomolecules leaves cavities that are complementary in size, shape and chemical functionality to the target biomolecules. The choice of the monomers bearing complementary functional groups to the imprinted species is of great importance in realizing highly selective recognition cavities after removing template biomolecules.²⁰³ Two different approaches have historically been explored for forming imprinted cavities, which rely on covalent and non-covalent interactions. Imprints relying on covalent interactions tend to exhibit slow binding and dissociation.²⁰⁴ Conversely, molecular imprints based on non-covalent interactions that exhibit faster binding and unbinding are more extensively employed for biodiagnostic applications. However, the non-covalent interactions between template biomolecules and polymer matrix tend to be weaker in aqueous media, thus lowering the target recognition capabilities of the imprints.²⁰¹ Since electrostatic, hydrogen bonding, and hydrophobic interactions are assumed to be the most prominent contacts between the imprint cavities and the target biomolecules, extensive efforts have been dedicated to strengthen these binding interactions to improve the sensitivity and specificity

of the artificial antibodies to specific analytes.²⁰⁵⁻²⁰⁸ Previously we employed two silane monomers, trimethoxypropylsilane (TMPS) and (3-aminopropyl) trimethoxysilane (APTMS), for molecular imprinting on plasmonic nanostructures.¹⁹⁸⁻¹⁹⁹ The siloxane copolymer is comprised of amine, methyl and hydroxyl groups that provide electrostatic, hydrophobic and hydrogen bonding interactions. Apart from silane monomers, a wide variety of other hydrophilic or hydrophobic monomers have been investigated to maximize the recognition capabilities of the artificial antibodies.²⁰⁹⁻²¹³

Although extensive efforts have been dedicated to the synthesis of artificial antibodies with high sensitivity and selectivity, most of these efforts are generic and the composition of the monomers is not often tailored to the target analyte. In this work, we have investigated the influence of the presence of an aromatic monomer, which provides aromatic electron donor-acceptor interactions, on the recognition capabilities of artificial antibodies. Refractive index sensitivity of plasmonic nanostructures is utilized to monitor various steps of the molecular imprinting process. We demonstrate that incorporation of an aromatic monomer significantly improves the sensitivity of artificial antibodies without sacrificing its selectivity.

8.2 Results and Discussion

Selective and sensitive recognition of target molecules by artificial antibodies can be achieved by optimizing the chemical functionality of the cavities in the polymer layer. As mentioned earlier, in addition to the size and shape complementarity, binding interactions between the walls of the cavities and the target biomolecules is critical in molecular imprinting^{11, 24}. Analogous to binding

interactions between protein and natural antibodies, the silane monomers bearing different functional groups interact with various chemical functionalities of the template protein and self-assemble during the formation of the polymer layer around the template protein. The concerted interactions between the chemical functional groups within the cavity and the target protein lead to sensitive and selective detection of the target biomolecules (Figure 1A). We hypothesize that inclusion of trimethoxyphenylsilane (TMPhS), an organic monomer with aromatic functionality, can facilitate aromatic interactions between the cavity and electron-deficient aromatic ring of target molecules.^{25, 26} The silane monomer with aromatic side chain is expected to result in aromatic interactions between the cavity and target biomolecule, thus improving the binding affinity and selectivity of the artificial recognition elements.^{8, 27-30} In order to verify this hypothesis, we synthesized and tested artificial antibodies with three sets of monomers using three different proteins with different amino acid contents as template biomolecules. We used the combination of two silane monomers, APTMS and TMPS, as Composition 1. Composition 2 is comprised of a third monomer, TMPhS. We then attempted to eliminate TMPS or APTMS in the three monomer mixture to determine the optimal combination of different organosilane monomers. Preliminary experiments indicated that the TMPhS and APTMS pair could form a uniform polymerization layer, named as Composition 3 (Figure 1A). However, polymerization could not be achieved with TMPhS and TMPS mixture and was not investigated further.

Gold nanorods (AuNRs) have been employed as plasmonic nanotransducers to probe the effect the monomer chemistry on the affinity and selectivity of the artificial antibodies. AuNRs were synthesized using a seed-mediated approach (see Experimental section for details). The TEM images revealed the diameter of AuNRs to be 13.6 ± 0.8 nm and the length to be 49.1 ± 2.8 nm, respectively

(Figures 1B and 1C). The vis-NIR extinction spectrum of AuNRs exhibited characteristic extinction bands corresponding to transverse (515 nm) and longitudinal (750 nm) plasmon resonances (Figure 1C). AuNRs are known to exhibit significantly higher refractive index sensitivity compared to spherical nanoparticles, making them better candidates for optical transduction of refractive index changes and plasmonic biosensors.^{31,32} Apart from higher refractive index sensitivity, yet another advantage of using AuNR is the large surface enhanced Raman scattering (SERS) activity of these nanostructures.^{33,34} We previously demonstrated that SERS can be employed to monitor various steps along the imprinting process including surface modification of AuNR to render amine functionality, template protein immobilization, polymerization (using APTMS and TMPS) and template removal.¹⁹⁸ In the present study, we employed SERS to monitor the successful incorporation of TPhS into the imprinted polymer layer. SERS spectra obtained from AuNR following the polymerization of TMPS and APTMS exhibited bands at 939 cm^{-1} and 1205 cm^{-1} assigned to rocking vibration and twisting vibration of CH_2 in APTMS. After addition of TPhS, the SERS spectra exhibited bands at 1003 cm^{-1} and 1031 cm^{-1} , corresponding to =C-H in-plane deformation modes and 1595 cm^{-1} corresponding to C=C stretching vibration in TPhS (Figure 2A and Figure 2B).²¹⁴ The SERS spectra confirm the successful incorporation of aromatic functionality into the molecular imprints formed after the inclusion of TPhS.

In this study, we have synthesized artificial antibodies for three proteins with different aromatic amino acid contents; lysozyme (8.8%), human hemoglobin (6.3%), and human PLIN2 (5.3%). We first describe the results using lysozyme as template and target protein. Refractive index sensitivity of LSPR wavelength of AuNRs (step 1, black spectra of Figure 3A) was employed to monitor each step along the molecular imprinting procedure, including formation of crosslinker layer with p-

aminothiophenol and glutaraldehyde (step 2 red spectra of Figure 3A), binding of template proteins (step 3, blue spectra of Figure 3A), copolymerization of monomers, (step 4, lavender spectra of Figure 3A). All spectra in Figure 3A were acquired in aqueous media. All of the spectra of Figure 3B were acquired in air and included step 4 (black spectra) the release of the template in step 5 (blue spectra); and the capture of target protein (red spectra). By limiting the red shift in the LSPR wavelength to ~ 3 nm during polymerization step 4, we maintained similar thickness of polymer layer for each monomer mixture. After treating with oxalic acid and sodium dodecyl sulfate, the template protein was removed by breaking the reversible imine bond and overcoming non-covalent interplays, respectively. Following the removal of the template protein, the AuNRs are left with polymer layer with cavities that are complementary in shape, size and chemical functionality to lysozyme. Figure 3C shows the entire molecular imprinting procedure and recapture of lysozyme (from phosphate buffered saline (PBS) spiked with lysozyme) using TMPS and APTMS (Composition 1) as the monomers for polymerization. The accumulated red shifts following completed steps of the imprinting process reached ~ 17 nm, while the blue shift corresponding to template protein removal was ~ 9 nm. After incubating in $5 \mu\text{g/ml}$ of lysozyme solution, a ~ 7.4 nm red shift in the LSPR wavelength indicated the successful recognition and rebinding of the target protein (Figure 3C).

The LSPR shift of AuNR imprinted with lysozyme with three different monomer compositions (Composition 1, 2 and 3 described above) exhibited a monotonic increase with increase in the concentration of lysozyme in the analyte solution (Figure 3D and 3E). Composition 2 showed significantly larger ($P=0.01$) LSPR shifts at each lysozyme concentration compared to that of the other two compositions. For the highest concentration tested here ($5 \mu\text{g/ml}$), the monomer mixture

comprised of TMPS and APTMS (Composition 1), exhibited a red shift of 7.3 ± 0.2 nm. In contrast, for the same concentration of lysozyme, the three monomer mixture (Composition 2) exhibited a red shift of 9.3 ± 0.3 nm, which represents a 40% improvement over Composition 1. This indicates that TPhS significantly improved the sensitivity of the plasmonic biosensor to the target protein, possibly through the aromatic electron donor-acceptor interactions. Conversely, the average LSPR shift with Composition 3 was found to be 6.2 ± 0.2 nm; nearly ~36% lower compared that in group of Composition 1 ($P=0.03$). The result clearly demonstrates that TPhS could not efficiently substitute for TMPS since the latter has hydroxyl and methyl functional groups that facilitate hydrogen bonding and hydrophobic interactions, respectively.³⁶ To investigate the selectivity of artificial antibodies, lysozyme imprinted AuNRs were separately challenged with either human or bovine serum albumin at a higher concentration ($20\ \mu\text{g/ml}$) compared to lysozyme ($5\ \mu\text{g/ml}$). The LSPR shifts of this non-template protein in Composition 1 2 and 3 ranged from 0.9 ± 0.2 nm to 1.5 ± 0.3 nm, respectively suggesting high selectivity of the artificial antibodies for the original template protein.

In order to further probe whether the fraction of aromatic amino acids in the target protein has a role in enhanced sensitivity with TPhS, we chose two other proteins and implemented molecular imprinting with Composition 1 and 2. PLIN2 is a protein with much larger molecular weight ($\text{MW}=49.3$ kDa) but significantly less aromatic amino acid content (5.3%) compared to lysozyme (8.8%). We controlled the thickness of the artificial antibody polymer layer by limiting the LSPR shift of AuNR during polymerization to ~3 nm (Figure S1A). LSPR shifts for each step along the molecular imprinting procedure are depicted in aqueous media (Figure S1A) or air (Figure S1B).

Figure 4A shows the LSPR shift of AuNR imprinted with PLIN2 upon exposure to different concentrations of PLIN2. The average sensitivity enhancement of LSPR shift for PLIN2 under Composition 2 compared to Composition 1 was found to be 19%. This sensitivity enhancement is smaller than the enhancement noted for lysozyme (40%). The reason for the lower sensitivity enhancement may be due to the lower content of aromatic amino acid content in PLIN2 compared to lysozyme, which results in fewer aromatic binding sites. The PLIN2 artificial antibodies prepared using Composition 1 and 2 exhibited excellent selectivity with LSPR shifts of only 0.9 ± 0.2 to 1.4 ± 0.2 nm upon exposure to either 20 $\mu\text{g/ml}$ of human or bovine serum albumin as an interfering protein. This further demonstrates the specificity of the antibodies to the template protein.

To further investigate the effect of aromatic amino acid content on the sensitivity and specificity of the artificial antibodies, one more protein was included in this study. Hemoglobin contains a higher aromatic amino acid content (6.9%) than PLIN2, while its molecular weight is quite close to the former (MW=64kDa). We again optimized the thickness of polymer layers by controlling LSPR shift to about 4 nm (Figure S1C) shown in aqueous media or air (Figure S1D). Upon exposure to 20 $\mu\text{g/ml}$ hemoglobin, AuNR imprinted with Composition 1 exhibited a red shift of 9.6 ± 0.3 nm (Figure 4C). The inclusion of TMPHS (*i.e.* Composition 2) significantly increased the LSPR shift to 11.2 ± 0.1 nm ($P=0.007$) for 20 $\mu\text{g/ml}$ of Hb. Overall, we note a ~26% enhancement in the sensitivity, which was 1.4 times higher than the sensitivity enhancement noted for PLIN2. This truly demonstrates that although the size of template may also influence sensitivity enhancement obtained by including TMPHS²¹⁵, the aromatic amino acid content in the protein played a dominant role in improving the sensitivity of artificial antibodies with aromatic electron donor-acceptor interactions facilitated by TMPHS. The artificial antibodies showed high selectivity as evidenced

by only ~1.0 nm LSPR shift upon exposure to either human or bovine serum albumin (20 $\mu\text{g/ml}$) (Figure 4D). This suggests that the incorporation of aromatic functionality in the artificial antibodies significantly improves the sensitivity but does not alter selectivity for the target protein.

The sensitivity of the artificial antibodies in this proof of concept study using gold nanorods is on the order of 20-100 nM. Previously we had shown that the sensitivity of the artificial antibodies for the same analyte could be decreased to the 1 nano molar range by using gold nanocages as the plasmonic nanotransducer.⁹ The sensitivity of DNA-driven, self-assembling nano pyramids with a Raman reporter or aptamer-based, surface-enhanced Raman scattering sensors can push the sensitivity of biomarker assays to a atto molar range.⁴⁰⁻⁴³ Basically, assays can be tailor made to measure biomarkers in concentration ranges of biologic importance with suitably functionalized transducers.

8.3 Conclusions

In summary, we investigated the role of aromatic interactions in the biorecognition capabilities of artificial antibodies using three model target proteins with different aromatic amino acid content. Artificial antibodies with aromatic functionality exhibited a significant, albeit protein-dependent, improvement in sensitivity. The sensitivity enhancement was found to be higher for proteins with higher aromatic amino acid content. Significantly, inclusion of aromatic interactions did not compromise the specificity of artificial recognition elements. Our results clearly highlight the need for fine tuning the composition of functional monomers employed for molecular imprinting. Enhancement in the sensitivity of plasmonic biosensors based on artificial antibodies through rational

choice of the functional monomer composition takes this plasmonic biosensing technology closer to real-world applications.

8.4 Experimental Section

Trimethoxyphenylsilane (TMPhS, 97%), trimethoxypropylsilane (TMPS, 97%), (3-aminopropyl) trimethoxysilane (APTMS, 99%), p-aminothiophenol (p-ATP), glutaraldehyde (Grade I, 25% in water), cetyltrimethylammonium bromide (CTAB), lysozyme, human serum albumin and hemoglobin (all lyophilized powders) were purchased from Sigma-Aldrich. Recombinant human Perilipin-2 (PLIN2) (liquid in 20mM Tris-HCl buffer, pH8.0) was purchased from Creative BioMart.

Gold Nanorod synthesis

Gold nanorods (AuNRs) were synthesized by using a seed-mediated method.^{38, 39} After sequentially adding 10ml of 0.1M CTAB, 2.5×10^{-4} M HAuCl₄ and 0.6 ml ice-cold 10mM sodium borohydride under vigorous magnetic stirring, the seed solution color changed to brown. Growth solution was prepared by adding 38 ml of 0.1 M CTAB, 0.4 ml of 10mM silver nitrate, 2 ml of 10 mM HAuCl₄, and 0.22 ml of 0.1 M ascorbic acid in order under gentle stirring. Then 0.6 ml seed solution was mixed into the above colorless solution and left undisturbed in the dark for 15 hours. The reaction solution turned to violet brown in the first hour. The AuNR solution was centrifuged twice at 8000rpm for 20 and 10 minutes respectively in order to remove excess CTAB. The particles were redispersed in nanopure water before modifying glass substrates. The AuNR showed

a narrow size distribution, whose average edge length was 49.1 ± 2.8 nm ($n > 50$) and side wall thickness was 13.6 ± 0.8 nm ($n > 50$) (Figure 1B, 1C). The spectral peak of the AuNR solution was 770 nm (Figure 1C).

Adsorption of Au nanorods on glass

Before coating with nanorods, piranha cleaned glass substrates were exposed to 1% (3-mercaptopropyl)triethoxysilane (MPTES) solution in ethanol for 1 hour and then rinsed with ethanol. The glass substrates were modified with nanorod solution for 3 hours. Finally the glass substrates were rinsed with water and thoroughly dried under a nitrogen stream.

Target protein imprinting procedure

The nanorod-modified glass substrates were immersed into a freshly prepared 2 ml phosphate buffer solution (pH 8.0) with 3 μ l of glutaraldehyde (25%) and 3 μ l of pATP (4mM in ethanol). The immersion time was controlled within 1 minute in order to achieve a polymer thickness of 3 nm providing a 2-3 nm LSPR shift¹⁹⁸. After rinsing with buffer gently, protein immobilization was performed by exposing samples in 10 μ g/ml lysozyme (MW=14.3kDa), 5 μ g/ml Human Recombinant Perilipin 2 (PLIN2; MW=49.3 kDa), or 25 μ g/ml hemoglobin (MW=64kDa) solution for 2 h at 4°C respectively. Preliminary studies had been performed by monitoring the red shift of the LSPR peak to saturate the activated nanorods with template protein and the time at 4°C to achieve saturation. After rinsing in the same phosphate buffer solution, the protein-immobilized glass substrates were incubated into 3 ml phosphate buffered saline (pH7.5) with mixtures of 10

μl TMPS and 10 μl APTMS (Composition 1); 5 μl TMPS, 5 μl APTMS and 0.5 μl TPhS (Composition 2); 10 μl APTMS and 1 μl TPhS, respectively (Composition 3). A 3-minute-reaction lead to a 3 to 4 nm LSPR red shift for synthesizing the artificial antibodies to lysozyme. Meanwhile, the reaction time was controlled within 10 minutes when detecting human recombinant perilipin 2 (PLIN2) and hemoglobin, resulting in a 4-5 nm LSPR red shifts at the polymerization step. After gently rinsing with phosphate buffer, the samples were kept in the buffer solution at 4°C overnight. The imprinted substrates were exposed to a mixed solution of 2% sodium dodecyl sulfate and 10mM oxalic acid for 1 hour for template release by breaking the reversible imine bond. After removal of the template, the AuNR were thus functionalized with complementary cavities with well-designed binding sites. Each step in the process was verified by monitoring the extinction spectrum.

Characterization techniques

The processes of AuNRs synthesis and molecular imprinting were monitored through extinction spectra using a Shimadzu UV-1800 spectrophotometer. Transmission electron micrograph images of the AuNRs were collected by a field emission transmission electron microscope (JEM-2100F, JEOL) at a voltage of 200 kV. The chemical composition of imprints were detected by surface enhanced Raman spectra obtained by using Renishaw inVia confocal Raman spectrometer installed on a Leica microscope with a 50X objective in a range of 100-3200 cm^{-1} .

Protein Binding Experiments

The molecularly imprinted (MIP) glass substrates were immersed in solutions of lysozyme, hemoglobin or PLIN2 (0.5 to 20 μ g/ml in phosphate buffered saline) for 4 hours at 4°C. Preliminary studies had been performed by monitoring the red shift in the LSPR peak to achieve analyte binding; usually 2 hours so this time was doubled. The substrates were then rinsed and dried under a stream of nitrogen prior to spectral analysis in air media. The cross binding experiments were performed by immersing imprinted sensors (MIP-lysozyme, MIP-PLIN2 and MIP-hemoglobin) in a solution with 20 μ g/ml human serum albumin for 4 hours at 4°C, rinsing and drying prior to spectral analysis.

Statistical Analysis

Significance between conditions was determined by Analyse-it for Excel 2010 (Analyse-it Software Ltd., Leeds, United Kingdom). Significance was defined as $P > 0.05$.

8.5 Figures

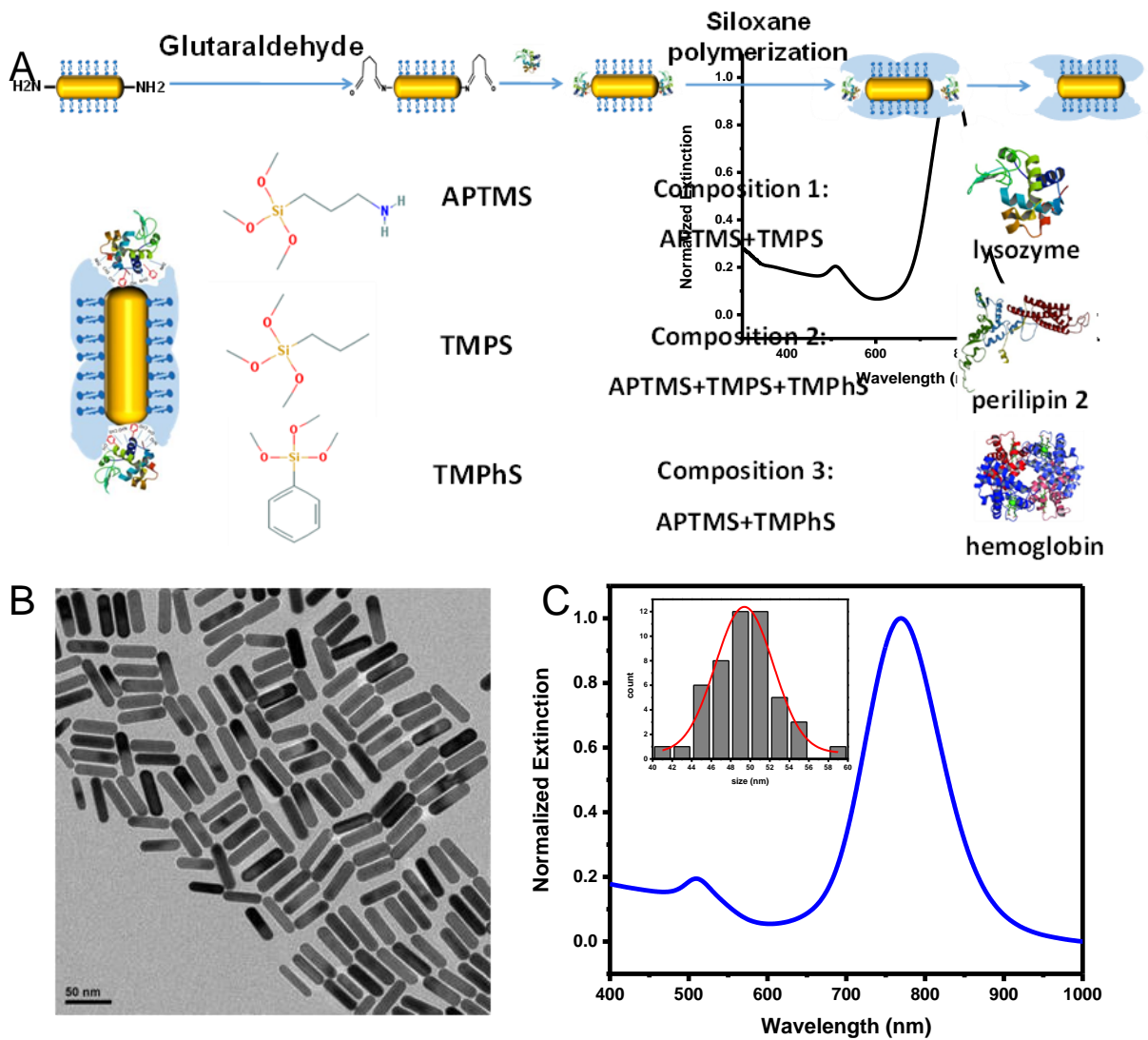


Figure 8. 1 (A) Schematic illustration showing the steps involved in molecular imprinting of gold nanorods with different monomers. (B) TEM image of gold nanorods (scale bar is 50nm). (C) Vis-NIR extinction spectra of aqueous suspension of gold nanorods. Inset shows the histogram of long axis length of gold nanorods obtained from TEM images.

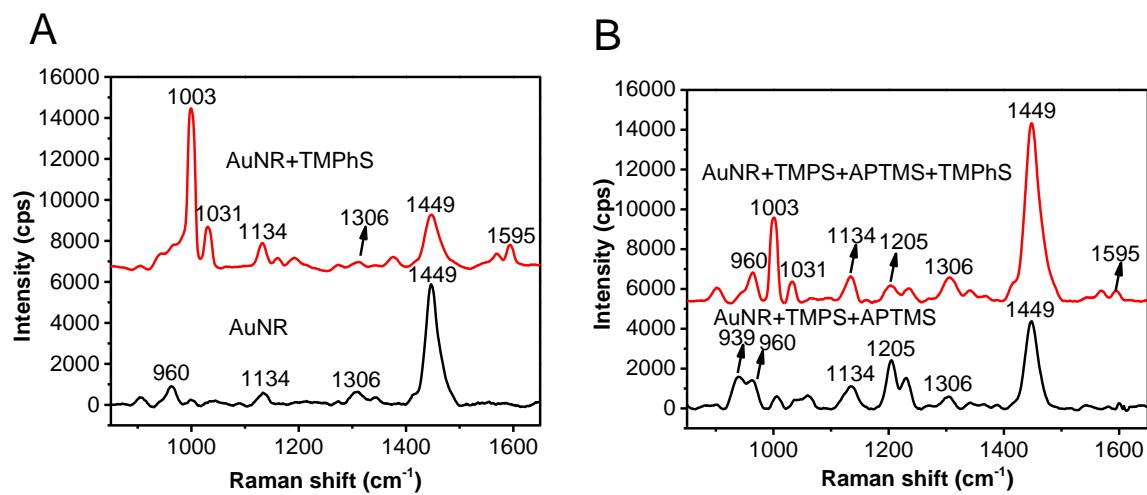


Figure 8. 2 (A) (B) Surface enhanced Raman scattering spectra with different amorphous polymers on gold nanorods reveal the Raman bands corresponding to trimethoxyphenylsilane.

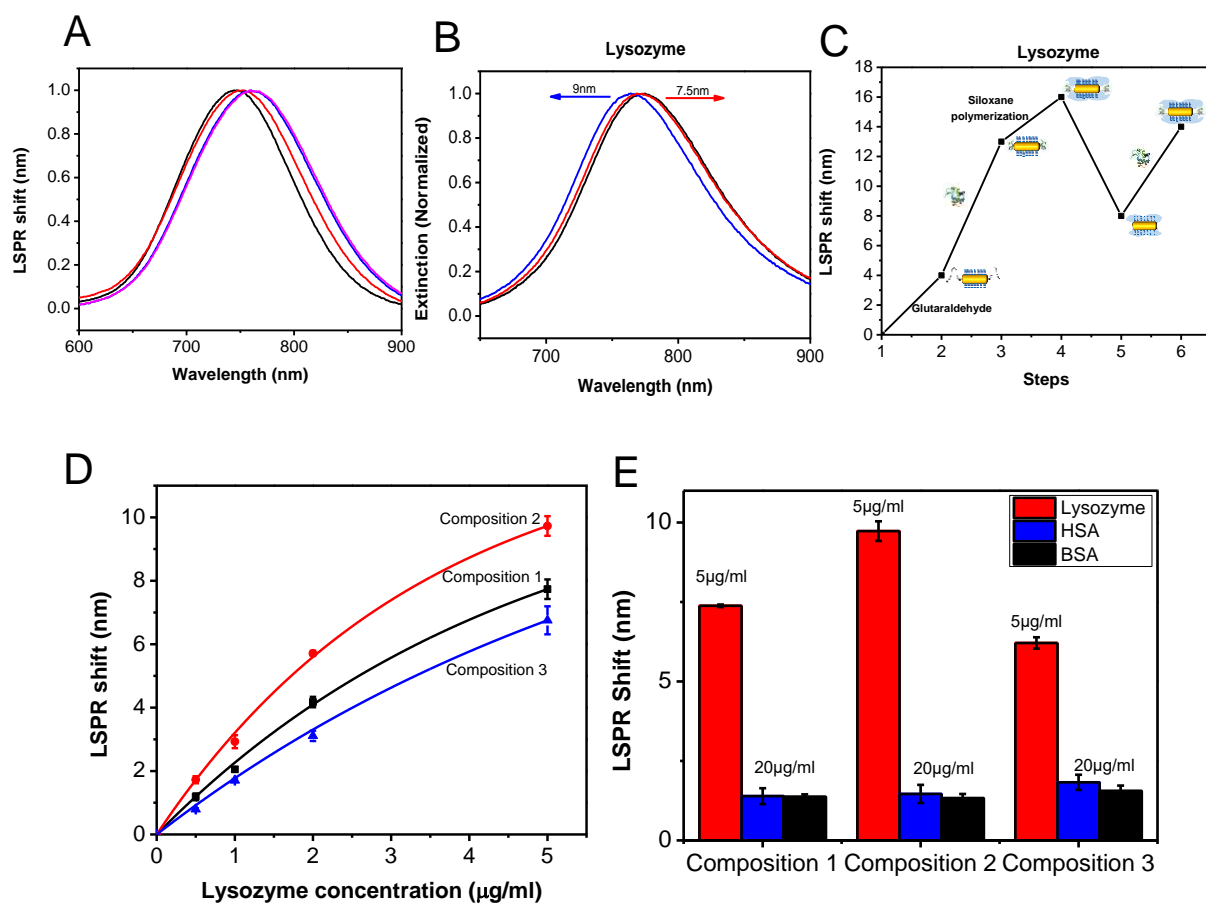


Figure 8. 3 (A) (B) (C) Extinction spectra and corresponding LSPR shift corresponding to each step in the molecular imprinting process when detecting 5 μ g/ml lysozyme. (A) spectra in aqueous media with step 1, black spectra; step 2, red spectra, step 3, blue spectra; and step 4, lavender spectra. (B) Spectra in air with step 4, black spectra, step 5, blue spectra and step 6, red spectra. (C) Summary of LSPR peak spectra shift at each step of the imprinting process. (D) Sensitivity of MIP-AuNR nanosensor expressed by the shift of LSPR wavelength when detecting lysozyme at different concentrations with polymers of different compositions. (E) Specificity of the lysozyme imprinted artificial antibody compared with interference protein (HSA or BSA) at distinct concentrations with polymers of different compositions.

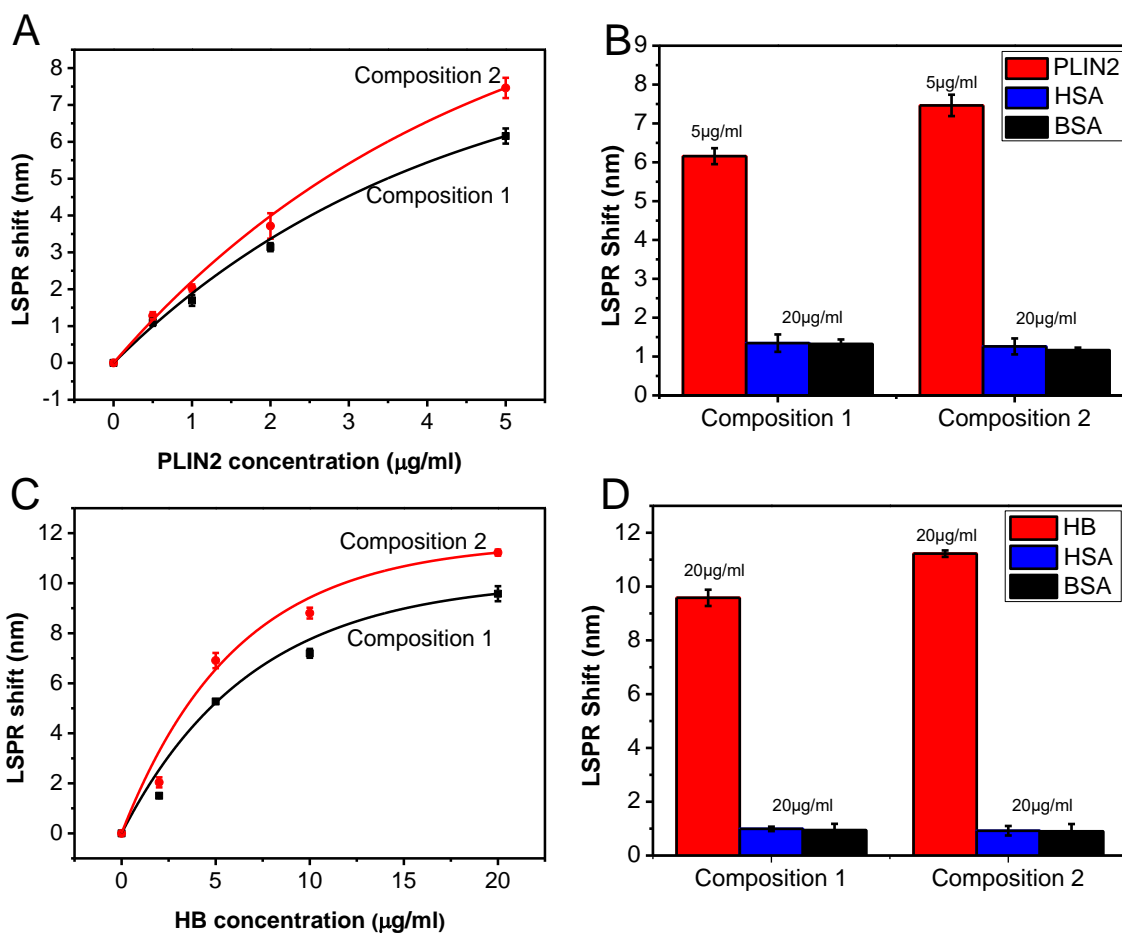


Figure 8. 4 (A) Sensitivity of MIP-AuNR nanosensor expressed by the shift of LSPR wavelength when detecting PLIN2 at different concentrations with polymers of different compositions. (B) Specificity of the PLIN2 imprinted artificial antibody compared with interference protein (HSA or BSA) at distinct concentrations with polymers of different compositions. (C) Sensitivity of MIP-AuNR nanosensor expressed by the shift of LSPR wavelength when detecting hemoglobin at different concentrations with polymers of different compositions. (D) LSPR shift of interference proteins (HSA or BSA) on hemoglobin imprinted plasmonic artificial antibody with polymers of different compositions.

Chapter 9: Conclusions

9.1 General conclusions

Harnessing the desirable properties of plasmonic materials, such as tunable LSPR wavelength, high refractive index sensitivity, and plasmon-enhanced fluorescence, we have established various sensing platforms for the ultrasensitive detection of biological markers, with special emphasis on their point-of-care applications. Specifically, this work : 1) greatly improved the efficiency of plasmon enhanced fluorescence and its broad utility through rational design of the structure of plasmonically-active nanomaterials, as well as their interaction with fluorophores and target biomolecules; 2) understand and engineer the interface between plasmonic nanostructure and target biomolecules to build stable and specific biorecognition elements for POC applications. Overall, this dissertation introduced novel material platforms and approaches for realizing ultrasensitive biodetection in POC settings.

Harnessing plasmon enhanced fluorescence, we have designed and built a simple and efficient material platform, namely “plasmonic patch”, that incorporates plasmonic nanomaterials with an elastomeric thin film to realize add-on fluorescence enhancer in fluoroimmunoassays. We have also systematically studied the effect of the size of the AuNRs on their fluorescence enhancement efficiency using plasmonic patch as material platform. We found that in addition to the LSPR wavelength of the plasmonic nanostructures, their absolute dimensions are critical for maximizing the fluorescence enhancement obtained using plasmonic patch. AuNR size optimized plasmonic patch-enhanced fluoroimmunoassay exhibited nearly lower limit-of-detection of biomarkers compared to unenhanced fluoroimmunoassay. High sensitivity and large dynamic range combined with the use of established bioassay platform (e.g., 96-well plates, multiplex microarrays, standard

affinity reagents, read-out devices) and work-flow makes the plasmon enhanced fluoroimmunoassays highly attractive for research and clinical applications.

As an extension of plasmonic patch, which is limited to application of planar surfaces, we have introduced a plasmonically-active ultrabright nanolabel, called “plasmonic fluor”, that is as bright as nearly 6500 organic fluorophores. Plasmonic-fluor is comprised of a plasmonic nanostructure (as fluorescence enhancer), a light emitter (e.g., any given molecular fluorophore or inorganic emitter), spacer layer, and a universal biological recognition element (e.g. biotin). This ultrabright “non-self-quenching” fluorescent nanoconstruct vastly outperformed previously reported fluorescent nanostructures in terms of brightness, specificity, colloidal stability, ease-of-use, and universal biofunctionality. Harnessing plasmonic-fluors, for the first time, we demonstrated that plasmon-enhanced fluorescence can be seamlessly integrated with a broad range of state-of-art bioanalytical technologies, including flow cytometry, immunocytochemistry, fluorophore-linked immunosorbent assay, and multiplexed bead-based immunoassays and immuno-arrays, to achieve more than 1000-fold improvement in the limit-of-detection, limit-of-quantification, and dynamic range.

In a different line of effort, we have systematically investigated the effect of composition and surface chemistry of artificial antibodies achieved through molecular imprinting on their biorecognition ability. We found that tailoring the composition of the “polymeric mold” to specific amino acid composition of the target proteins greatly enhances their binding affinity. Specifically, we have investigated the role of aromatic interactions in the biorecognition capabilities of artificial antibodies. Artificial antibodies with aromatic functionality exhibited a significant, albeit protein-dependent, improvement in sensitivity. The sensitivity enhancement was found to be higher for proteins with higher aromatic amino acid content. Significantly, inclusion of aromatic interactions

did not compromise the specificity of artificial recognition elements. We also found that plasmonic biosensors based on artificial antibody exhibit excellent thermal, temporal, and chemical stability compared to its natural counterpart. The superior stability of this class of sensors makes them excellent candidates in resource-limited settings such as at-home care, rural clinics, developing countries with low and moderate incomes and battlefield, where refrigeration and tight regulation of environmental conditions is not always possible.

Furthermore, we have improved the specificity and sensitivity of the plasmonic biosensor using artificial antibodies through innovative surface passivation methods. Specifically, we demonstrated PEGylation of the non-recognition (i.e. non-cavity) regions of the molecular imprints as a highly efficient and broadly applicable method to reduce non-specific binding and significantly improve the selectivity of artificial antibodies. The LSPR shift, or the specificity, of the PEGylated artificial antibody was found to be nearly 10 times smaller than the non-PEGylated counterparts. Enhancement in the sensitivity as well as its specificity of plasmonic biosensors based on artificial antibodies through rational design of its functional monomer composition and surface chemistry. Towards improving the sensitivity, we also introduced a LSPR signal amplification strategy based on the biomineralization of a MOF on the captured analyte proteins. The amplification relies on the differential ability of abiotic recognition elements and captured biomolecules to induce biomineralization of a MOF, leading to two-fold improvement in the sensitivity of artificial antibody-biosensor. We believe that various efforts made along this line can potentially take plasmonic biosensing technology closer to real-world applications.

9.2 Significance and outlook

In addition to the representative systems studied here, the design principles, material fabrication methods, approaches, and results can have far reaching implications to realize various plasmonically-active materials with applications ranging from biomedical and clinical research to diagnosis, such as fluorescence-activated cell sorting (FACS), lateral flow assays, single-cell analysis, and western blot. Especially, by integrating emerging biotechnology platforms such as expansion microscopy, portable read-out device (cell-phone based readers), with the plasmonically-active materials introduced in this work (e.g., plasmonic patch and plasmonic-fluor), ultrasensitive bioanalytical technologies that can be deployed in point-of-care and resource limited settings, such as rural developing areas can be realized.

Reference

1. Stern, E.; Vacic, A.; Rajan, N. K.; Criscione, J. M.; Park, J.; Ilic, B. R.; Mooney, D. J.; Reed, M. A.; Fahmy, T. M., Label-free biomarker detection from whole blood. *Nature nanotechnology* **2010**, *5* (2), 138.
2. Willets, K. A.; Van Duyne, R. P., Localized surface plasmon resonance spectroscopy and sensing. *Annu. Rev. Phys. Chem.* **2007**, *58*, 267-297.
3. Zhao, J.; Zhang, X.; Yonzon, C. R.; Haes, A. J.; Van Duyne, R. P., Localized surface plasmon resonance biosensors. **2006**.
4. Fu, Y.; Zhang, J.; Lakowicz, J. R., Plasmon-enhanced fluorescence from single fluorophores end-linked to gold nanorods. *Journal of the American Chemical Society* **2010**, *132* (16), 5540-5541.
5. Kneipp, K.; Wang, Y.; Kneipp, H.; Perelman, L. T.; Itzkan, I.; Dasari, R. R.; Feld, M. S., Single molecule detection using surface-enhanced Raman scattering (SERS). *Physical review letters* **1997**, *78* (9), 1667.
6. Osawa, M., Dynamic processes in electrochemical reactions studied by surface-enhanced infrared absorption spectroscopy (SEIRAS). *Bulletin of the Chemical Society of Japan* **1997**, *70* (12), 2861-2880.
7. Rosi, N. L.; Mirkin, C. A., Nanostructures in biodiagnostics. *Chemical reviews* **2005**, *105* (4), 1547-1562.
8. Maier, S. A.; Atwater, H. A., Plasmonics: Localization and guiding of electromagnetic energy in metal/dielectric structures. *Journal of applied physics* **2005**, *98* (1), 10.
9. Mayer, K. M.; Hafner, J. H., Localized Surface Plasmon Resonance Sensors. *Chemical Reviews* **2011**, *111* (6), 3828-3857.
10. Anker, J. N.; Hall, W. P.; Lyandres, O.; Shah, N. C.; Zhao, J.; Van Duyne, R. P., Biosensing with plasmonic nanosensors. *Nature materials* **2008**, *7* (6), 442.
11. Tian, L.; Morrissey, J. J.; Kattumenu, R.; Gandra, N.; Kharasch, E. D.; Singamaneni, S., Bioplasmonic paper as a platform for detection of kidney cancer biomarkers. *Analytical chemistry* **2012**, *84* (22), 9928-9934.
12. Sepúlveda, B.; Angelomé, P. C.; Lechuga, L. M.; Liz-Marzán, L. M., LSPR-based nanobiosensors. *nano today* **2009**, *4* (3), 244-251.
13. Novo, C.; Funston, A. M.; Gooding, A. K.; Mulvaney, P., Electrochemical charging of single gold nanorods. *Journal of the American Chemical Society* **2009**, *131* (41), 14664-14666.
14. Mayer, K. M.; Hao, F.; Lee, S.; Nordlander, P.; Hafner, J. H., A single molecule immunoassay by localized surface plasmon resonance. *nanotechnology* **2010**, *21* (25), 255503.
15. Hall, W. P.; Modica, J.; Anker, J.; Lin, Y.; Mrksich, M.; Van Duyne, R. P., A conformation- and ion-sensitive plasmonic biosensor. *Nano letters* **2011**, *11* (3), 1098-1105.
16. Bingham, J. M.; Anker, J. N.; Kreno, L. E.; Van Duyne, R. P., Gas sensing with high-resolution localized surface plasmon resonance spectroscopy. *Journal of the American Chemical Society* **2010**, *132* (49), 17358-17359.
17. Marinakos, S. M.; Chen, S.; Chilkoti, A., Plasmonic detection of a model analyte in serum by a gold nanorod sensor. *Analytical chemistry* **2007**, *79* (14), 5278-5283.
18. Nusz, G. J.; Marinakos, S. M.; Curry, A. C.; Dahlin, A.; Höök, F.; Wax, A.; Chilkoti, A., Label-free plasmonic detection of biomolecular binding by a single gold nanorod. *Analytical chemistry* **2008**, *80* (4), 984-989.
19. Olkhov, R. V.; Fowke, J. D.; Shaw, A. M., Whole serum BSA antibody screening using a label-free biophotonic nanoparticle array. *Analytical biochemistry* **2009**, *385* (2), 234-241.

20. Stadler, C.; Rexhepaj, E.; Singan, V. R.; Murphy, R. F.; Pepperkok, R.; Uhlén, M.; Simpson, J. C.; Lundberg, E., Immunofluorescence and fluorescent-protein tagging show high correlation for protein localization in mammalian cells. *Nature methods* **2013**, *10* (4), 315-323.
21. Brennan, D. J.; O'connor, D. P.; Rexhepaj, E.; Ponten, F.; Gallagher, W. M., Antibody-based proteomics: fast-tracking molecular diagnostics in oncology. *Nature Reviews Cancer* **2010**, *10* (9), 605-617.
22. Mancias, J. D.; Wang, X.; Gygi, S. P.; Harper, J. W.; Kimmelman, A. C., Quantitative proteomics identifies NCOA4 as the cargo receptor mediating ferritinophagy. *Nature* **2014**, *509* (7498), 105-109.
23. Flauraud, V.; Regmi, R.; Winkler, P. M.; Alexander, D. T.; Rigneault, H.; Van Hulst, N. F.; García-Parajo, M. F.; Wenger, J. r. m.; Brugger, J. r., In-plane plasmonic antenna arrays with surface nanogaps for giant fluorescence enhancement. *Nano Letters* **2017**, *17* (3), 1703-1710.
24. Tam, F.; Goodrich, G. P.; Johnson, B. R.; Halas, N. J., Plasmonic enhancement of molecular fluorescence. *Nano letters* **2007**, *7* (2), 496-501.
25. Kinkhabwala, A.; Yu, Z.; Fan, S.; Avlasevich, Y.; Müllen, K.; Moerner, W., Large single-molecule fluorescence enhancements produced by a bowtie nanoantenna. *Nature Photonics* **2009**, *3* (11), 654-657.
26. Tabakman, S. M.; Lau, L.; Robinson, J. T.; Price, J.; Sherlock, S. P.; Wang, H.; Zhang, B.; Chen, Z.; Tangsombatvisit, S.; Jarrell, J. A., Plasmonic substrates for multiplexed protein microarrays with femtomolar sensitivity and broad dynamic range. *Nature communications* **2011**, *2*, 466.
27. Zhang, B.; Kumar, R. B.; Dai, H.; Feldman, B. J., A plasmonic chip for biomarker discovery and diagnosis of type 1 diabetes. *Nature medicine* **2014**, *20* (8), 948-953.
28. Zhang, B.; Pinsky, B. A.; Ananta, J. S.; Zhao, S.; Arulkumar, S.; Wan, H.; Sahoo, M. K.; Abeynayake, J.; Waggoner, J. J.; Hopes, C., Diagnosis of Zika virus infection on a nanotechnology platform. *Nature Medicine* **2017**, *23* (5), 548-550.
29. Liu, B.; Li, Y.; Wan, H.; Wang, L.; Xu, W.; Zhu, S.; Liang, Y.; Zhang, B.; Lou, J.; Dai, H., High Performance, Multiplexed Lung Cancer Biomarker Detection on a Plasmonic Gold Chip. *Advanced Functional Materials* **2016**, *26* (44), 7994-8002.
30. Haes, A. J.; Chang, L.; Klein, W. L.; Van Duyne, R. P., Detection of a biomarker for Alzheimer's disease from synthetic and clinical samples using a nanoscale optical biosensor. *Journal of the American Chemical Society* **2005**, *127* (7), 2264-2271.
31. Bardhan, R.; Grady, N. K.; Cole, J. R.; Joshi, A.; Halas, N. J., Fluorescence enhancement by Au nanostructures: nanoshells and nanorods. *Acs Nano* **2009**, *3* (3), 744-752.
32. Pompa, P.; Martiradonna, L.; Della Torre, A.; Della Sala, F.; Manna, L.; De Vittorio, M.; Calabi, F.; Cingolani, R.; Rinaldi, R., Metal-enhanced fluorescence of colloidal nanocrystals with nanoscale control. *Nature nanotechnology* **2006**, *1* (2), 126-130.
33. Zhou, L.; Ding, F.; Chen, H.; Ding, W.; Zhang, W.; Chou, S. Y., Enhancement of immunoassay's fluorescence and detection sensitivity using three-dimensional plasmonic nano-antenna-dots array. *Analytical chemistry* **2012**, *84* (10), 4489-4495.
34. Abbas, A.; Tian, L.; Morrissey, J. J.; Kharasch, E. D.; Singamaneni, S., Hot Spot-Localized Artificial Antibodies for Label-Free Plasmonic Biosensing. *Advanced functional materials* **2013**, *23* (14), 1789-1797.
35. Tian, L.; Liu, K.-K.; Morrissey, J. J.; Gandra, N.; Kharasch, E. D.; Singamaneni, S., Gold nanocages with built-in artificial antibodies for label-free plasmonic biosensing. *J. Mater. Chem. B* **2014**, *2* (2), 167-170.

36. Woodbury, R. L.; Varnum, S. M.; Zangar, R. C., Elevated HGF levels in sera from breast cancer patients detected using a protein microarray ELISA. *Journal of proteome research* **2002**, *1* (3), 233-237.
37. Schweitzer, B.; Roberts, S.; Grimwade, B.; Shao, W.; Wang, M.; Fu, Q.; Shu, Q.; Laroche, I.; Zhou, Z.; Tchernev, V. T., Multiplexed protein profiling on microarrays by rolling-circle amplification. *Nature biotechnology* **2002**, *20* (4), 359-365.
38. Ali, M. M.; Li, F.; Zhang, Z.; Zhang, K.; Kang, D.-K.; Ankrum, J. A.; Le, X. C.; Zhao, W., Rolling circle amplification: a versatile tool for chemical biology, materials science and medicine. *Chemical Society Reviews* **2014**, *43* (10), 3324-3341.
39. Ganesh, N.; Zhang, W.; Mathias, P. C.; Chow, E.; Soares, J.; Malyarchuk, V.; Smith, A. D.; Cunningham, B. T., Enhanced fluorescence emission from quantum dots on a photonic crystal surface. *Nature nanotechnology* **2007**, *2* (8), 515-520.
40. Wang, C.; Tadepalli, S.; Luan, J.; Liu, K. K.; Morrissey, J. J.; Kharasch, E. D.; Naik, R. R.; Singamaneni, S., Metal-Organic Framework as a Protective Coating for Biodiagnostic Chips. *Advanced Materials* **2017**, *29* (7).
41. Liu, J.; Zong, G.; He, L.; Zhang, Y.; Liu, C.; Wang, L., Effects of fumed and mesoporous silica nanoparticles on the properties of sylgard 184 polydimethylsiloxane. *Micromachines* **2015**, *6* (7), 855-864.
42. Mannsfeld, S. C.; Tee, B. C.; Stoltenberg, R. M.; Chen, C. V. H.; Barman, S.; Muir, B. V.; Sokolov, A. N.; Reese, C.; Bao, Z., Highly sensitive flexible pressure sensors with microstructured rubber dielectric layers. *Nature materials* **2010**, *9* (10), 859-864.
43. Qin, D.; Xia, Y.; Whitesides, G. M., Soft lithography for micro-and nanoscale patterning. *Nature protocols* **2010**, *5* (3), 491-502.
44. Yuan, H.; Khatua, S.; Zijlstra, P.; Yorulmaz, M.; Orrit, M., Thousand-fold Enhancement of Single-Molecule Fluorescence Near a Single Gold Nanorod. *Angewandte Chemie International Edition* **2013**, *52* (4), 1217-1221.
45. Khatua, S.; Paulo, P. M.; Yuan, H.; Gupta, A.; Zijlstra, P.; Orrit, M., Resonant plasmonic enhancement of single-molecule fluorescence by individual gold nanorods. *ACS nano* **2014**, *8* (5), 4440-4449.
46. Gandra, N.; Portz, C.; Tian, L.; Tang, R.; Xu, B.; Achilefu, S.; Singamaneni, S., Probing Distance-Dependent Plasmon-Enhanced Near-Infrared Fluorescence Using Polyelectrolyte Multilayers as Dielectric Spacers. *Angewandte Chemie* **2014**, *126* (3), 885-889.
47. Abadeer, N. S.; Brennan, M. R.; Wilson, W. L.; Murphy, C. J., Distance and plasmon wavelength dependent fluorescence of molecules bound to silica-coated gold nanorods. *ACS nano* **2014**, *8* (8), 8392-8406.
48. Mishra, H.; Mali, B. L.; Karolin, J.; Dragan, A. I.; Geddes, C. D., Experimental and theoretical study of the distance dependence of metal-enhanced fluorescence, phosphorescence and delayed fluorescence in a single system. *Physical Chemistry Chemical Physics* **2013**, *15* (45), 19538-19544.
49. Yan, B.; Thubagere, A.; Premasiri, W. R.; Ziegler, L. D.; Dal Negro, L.; Reinhard, B. M., Engineered SERS substrates with multiscale signal enhancement: nanoparticle cluster arrays. *ACS Nano* **2009**, *3* (5), 1190-1202.
50. Pierre, M. C. S.; Haes, A. J., Purification implications on SERS activity of silica coated gold nanospheres. *Analytical chemistry* **2012**, *84* (18), 7906-7911.
51. Anger, P.; Bharadwaj, P.; Novotny, L., Enhancement and quenching of single-molecule fluorescence. *Physical review letters* **2006**, *96* (11), 113002.
52. Bardhan, R.; Grady, N. K.; Halas, N. J., Nanoscale Control of Near-Infrared Fluorescence Enhancement Using Au Nanoshells. *Small* **2008**, *4* (10), 1716-1722.

53. Mishra, J.; Dent, C.; Tarabishi, R.; Mitsnefes, M. M.; Ma, Q.; Kelly, C.; Ruff, S. M.; Zahedi, K.; Shao, M.; Bean, J., Neutrophil gelatinase-associated lipocalin (NGAL) as a biomarker for acute renal injury after cardiac surgery. *The Lancet* **2005**, *365* (9466), 1231-1238.
54. Han, W.; Waikar, S.; Johnson, A.; Betensky, R.; Dent, C.; Devarajan, P.; Bonventre, J., Urinary biomarkers in the early diagnosis of acute kidney injury. *Kidney international* **2008**, *73* (7), 863-869.
55. Vaidya, V. S.; Waikar, S. S.; Ferguson, M. A.; Collings, F. B.; Sunderland, K.; Gioules, C.; Bradwin, G.; Matsouaka, R.; Betensky, R. A.; Curhan, G. C., Urinary biomarkers for sensitive and specific detection of acute kidney injury in humans. *Clinical and translational science* **2008**, *1* (3), 200-208.
56. Levey, A. S.; Eckardt, K.-U.; Tsukamoto, Y.; Levin, A.; Coresh, J.; Rossert, J.; Zeeuw, D. D.; Hostetter, T. H.; Lameire, N.; Eknoyan, G., Definition and classification of chronic kidney disease: a position statement from Kidney Disease: Improving Global Outcomes (KDIGO). *Kidney international* **2005**, *67* (6), 2089-2100.
57. Chaturvedi, S.; Farmer, T.; Kapke, G. F., Assay validation for KIM-1: human urinary renal dysfunction biomarker. *International journal of biological sciences* **2009**, *5* (2), 128.
58. Woo, K.-S.; Choi, J.-L.; Kim, B.-R.; Kim, J.-E.; An, W.-S.; Han, J.-Y., Urinary neutrophil gelatinase-associated lipocalin levels in comparison with glomerular filtration rate for evaluation of renal function in patients with diabetic chronic kidney disease. *Diabetes & metabolism journal* **2012**, *36* (4), 307-313.
59. Macisaac, R. J.; Tsalamandris, C.; Thomas, M. C.; Premaratne, E.; Panagiotopoulos, S.; Smith, T.; Poon, A.; Jenkins, M. A.; Ratnaike, S.; Power, D. A., Estimating glomerular filtration rate in diabetes: a comparison of cystatin-C-and creatinine-based methods. *Diabetologia* **2006**, *49* (7), 1686-1689.
60. Kashani, K.; Al-Khafaji, A.; Ardiles, T.; Artigas, A.; Bagshaw, S. M.; Bell, M.; Bihorac, A.; Birkhahn, R.; Cely, C. M.; Chawla, L. S., Discovery and validation of cell cycle arrest biomarkers in human acute kidney injury. *Critical care* **2013**, *17* (1), R25.
61. MacBeath, G., Protein microarrays and proteomics. *Nature genetics* **2002**, *32*, 526-532.
62. Madoz-Gúrpide, J.; Wang, H.; Misek, D. E.; Brichory, F.; Hanash, S. M., Protein based microarrays: a tool for probing the proteome of cancer cells and tissues. *Proteomics* **2001**, *1* (10), 1279-1287.
63. Tighe, P. J.; Ryder, R. R.; Todd, I.; Fairclough, L. C., ELISA in the multiplex era: potentials and pitfalls. *PROTEOMICS-Clinical Applications* **2015**, *9* (3-4), 406-422.
64. Anger, P.; Bharadwaj, P.; Novotny, L., Enhancement and quenching of single-molecule fluorescence. *Physical review letters* **2006**, *96* (11), 113002.
65. Tam, F.; Goodrich, G. P.; Johnson, B. R.; Halas, N. J., Plasmonic enhancement of molecular fluorescence. *Nano letters* **2007**, *7* (2), 496-501.
66. Kinkhabwala, A.; Yu, Z.; Fan, S.; Avlasevich, Y.; Müllen, K.; Moerner, W., Large single-molecule fluorescence enhancements produced by a bowtie nanoantenna. *Nature Photonics* **2009**, *3* (11), 654.
67. Rose, A.; Hoang, T. B.; McGuire, F.; Mock, J. J.; Ciraci, C.; Smith, D. R.; Mikkelsen, M. H., Control of radiative processes using tunable plasmonic nanopatch antennas. *Nano letters* **2014**, *14* (8), 4797-4802.
68. Luan, J.; Morrissey, J. J.; Wang, Z.; Derami, H. G.; Liu, K.-K.; Cao, S.; Jiang, Q.; Wang, C.; Kharasch, E. D.; Naik, R. R.; Singamaneni, S., Add-on plasmonic patch as a universal fluorescence enhancer. *Light: Science & Applications* **2018**, *7* (1), 29.
69. Li, J.-F.; Li, C.-Y.; Aroca, R. F., Plasmon-enhanced fluorescence spectroscopy. *Chemical Society Reviews* **2017**, *46* (13), 3962-3979.

70. Novo, C.; Gomez, D.; Perez-Juste, J.; Zhang, Z.; Petrova, H.; Reismann, M.; Mulvaney, P.; Hartland, G. V., Contributions from radiation damping and surface scattering to the linewidth of the longitudinal plasmon band of gold nanorods: a single particle study. *Physical Chemistry Chemical Physics* **2006**, *8* (30), 3540-3546.
71. Hu, M.; Novo, C.; Funston, A.; Wang, H.; Staleva, H.; Zou, S.; Mulvaney, P.; Xia, Y.; Hartland, G. V., Dark-field microscopy studies of single metal nanoparticles: understanding the factors that influence the linewidth of the localized surface plasmon resonance. *Journal of materials chemistry* **2008**, *18* (17), 1949-1960.
72. Lin, K.-Q.; Yi, J.; Hu, S.; Liu, B.-J.; Liu, J.-Y.; Wang, X.; Ren, B., Size Effect on SERS of gold nanorods demonstrated via single nanoparticle spectroscopy. *The Journal of Physical Chemistry C* **2016**, *120* (37), 20806-20813.
73. Ni, W.; Kou, X.; Yang, Z.; Wang, J., Tailoring longitudinal surface plasmon wavelengths, scattering and absorption cross sections of gold nanorods. *ACS Nano* **2008**, *2* (4), 677-686.
74. Park, K.; Biswas, S.; Kanel, S.; Nepal, D.; Vaia, R. A., Engineering the optical properties of gold nanorods: independent tuning of surface plasmon energy, extinction coefficient, and scattering cross section. *The Journal of Physical Chemistry C* **2014**, *118* (11), 5918-5926.
75. Jain, P. K.; Lee, K. S.; El-Sayed, I. H.; El-Sayed, M. A., Calculated absorption and scattering properties of gold nanoparticles of different size, shape, and composition: applications in biological imaging and biomedicine. *The journal of physical chemistry B* **2006**, *110* (14), 7238-7248.
76. Wang, G.; Huang, H.; Zhang, G.; Zhang, X.; Fang, B.; Wang, L., Dual amplification strategy for the fabrication of highly sensitive interleukin-6 amperometric immunosensor based on poly-dopamine. *Langmuir* **2011**, *27* (3), 1224-31.
77. Dineshkumar, T.; Ashwini, B. K.; Rameshkumar, A.; Rajashree, P.; Ramya, R.; Rajkumar, K., Salivary and serum interleukin-6 levels in oral premalignant disorders and squamous cell carcinoma: diagnostic value and clinicopathologic correlations. *Asian Pacific journal of cancer prevention: APJCP* **2016**, *17* (11), 4899.
78. Sahibzada, H. A.; Khurshid, Z.; Khan, R. S.; Naseem, M.; Siddique, K. M.; Mali, M.; Zafar, M. S., Salivary IL-8, IL-6 and TNF- α as potential diagnostic biomarkers for oral cancer. *Diagnostics* **2017**, *7* (2), 21.
79. John, M. A. S.; Li, Y.; Zhou, X.; Denny, P.; Ho, C.-M.; Montemagno, C.; Shi, W.; Qi, F.; Wu, B.; Sinha, U., Interleukin 6 and interleukin 8 as potential biomarkers for oral cavity and oropharyngeal squamous cell carcinoma. *Archives of Otolaryngology-Head & Neck Surgery* **2004**, *130* (8), 929-935.
80. Wang, G.; He, X.; Chen, L.; Zhu, Y.; Zhang, X., Ultrasensitive IL-6 electrochemical immunosensor based on Au nanoparticles-graphene-silica biointerface. *Colloids Surf B Biointerfaces* **2014**, *116*, 714-9.
81. Hong, D. S.; Angelo, L. S.; Kurzrock, R., Interleukin-6 and its receptor in cancer: implications for translational therapeutics. *Cancer* **2007**, *110* (9), 1911-28.
82. Orendorff, C. J.; Gearheart, L.; Jana, N. R.; Murphy, C. J., Aspect ratio dependence on surface enhanced Raman scattering using silver and gold nanorod substrates. *Physical chemistry chemical physics : PCCP* **2006**, *8* (1), 165-70.
83. Cohen, L.; Walt, D. R., Highly Sensitive and Multiplexed Protein Measurements. *Chemical reviews* **2018**.
84. Hanash, S. M.; Pitteri, S. J.; Faca, V. M., Mining the plasma proteome for cancer biomarkers. *Nature* **2008**, *452* (7187), 571.
85. Shaw, L. M.; Korecka, M.; Clark, C. M.; Lee, V. M.-Y.; Trojanowski, J. Q., Biomarkers of neurodegeneration for diagnosis and monitoring therapeutics. *Nature reviews Drug discovery* **2007**, *6* (4), nrd2176.

86. Blennow, K.; Zetterberg, H., Understanding biomarkers of neurodegeneration: ultrasensitive detection techniques pave the way for mechanistic understanding. *Nature medicine* **2015**, *21* (3), 217.
87. Savage, M. J.; Kalinina, J.; Wolfe, A.; Tugusheva, K.; Korn, R.; Cash-Mason, T.; Maxwell, J. W.; Hatcher, N. G.; Haugabook, S. J.; Wu, G., A sensitive $\alpha\beta$ oligomer assay discriminates Alzheimer's and aged control cerebrospinal fluid. *Journal of Neuroscience* **2014**, *34* (8), 2884-2897.
88. Westermann, D.; Neumann, J. T.; Sörensen, N. A.; Blankenberg, S., High-sensitivity assays for troponin in patients with cardiac disease. *Nature Reviews Cardiology* **2017**, *14* (8), 472.
89. Rissin, D. M.; Kan, C. W.; Campbell, T. G.; Howes, S. C.; Fournier, D. R.; Song, L.; Piech, T.; Patel, P. P.; Chang, L.; Rivnak, A. J., Single-molecule enzyme-linked immunosorbent assay detects serum proteins at subfemtomolar concentrations. *Nature biotechnology* **2010**, *28* (6), 595.
90. Zhang, B.; Yang, J.; Zou, Y.; Gong, M.; Chen, H.; Hong, G.; Antaris, A. L.; Li, X.; Liu, C.-L.; Chen, C., Plasmonic micro-beads for fluorescence enhanced, multiplexed protein detection with flow cytometry. *Chemical Science* **2014**, *5* (10), 4070-4075.
91. Steward, M. W.; Lew, A. M., The importance of antibody affinity in the performance of immunoassays for antibody. *Journal of immunological methods* **1985**, *78* (2), 173-190.
92. Roth, S.; Hadass, O.; Cohen, M.; Verbarg, J.; Wilsey, J.; Danielli, A., Photobleaching: Improving the Sensitivity of Fluorescence-Based Immunoassays by Photobleaching the Autofluorescence of Magnetic Beads (Small 3/2019). *Small* **2019**, *15* (3), 1970016.
93. Zhang, P.; Zhou, X.; He, M.; Shang, Y.; Tetlow, A. L.; Godwin, A. K.; Zeng, Y., Ultrasensitive detection of circulating exosomes with a 3D-nanopatterned microfluidic chip. *Nature Biomedical Engineering* **2019**, *1*.
94. Espina, V.; Woodhouse, E. C.; Wulfkühle, J.; Asmussen, H. D.; Petricoin III, E. F.; Liotta, L. A., Protein microarray detection strategies: focus on direct detection technologies. *Journal of immunological methods* **2004**, *290* (1-2), 121-133.
95. Chen, Z.; Tabakman, S. M.; Goodwin, A. P.; Kattah, M. G.; Daranciang, D.; Wang, X.; Zhang, G.; Li, X.; Liu, Z.; Utz, P. J., Protein microarrays with carbon nanotubes as multicolor Raman labels. *Nature biotechnology* **2008**, *26* (11), 1285.
96. Luan, J.; Morrissey, J. J.; Wang, Z.; Derami, H. G.; Liu, K.-K.; Cao, S.; Jiang, Q.; Wang, C.; Kharasch, E. D.; Naik, R. R., Add-on plasmonic patch as a universal fluorescence enhancer. *Light: Science & Applications* **2018**, *7* (1), 29.
97. Reisch, A.; Didier, P.; Richert, L.; Oncul, S.; Arntz, Y.; Mély, Y.; Klymchenko, A. S., Collective fluorescence switching of counterion-assembled dyes in polymer nanoparticles. *Nature Communications* **2014**, *5*, 4089.
98. Hu, J.; Zhang, Z.-L.; Wen, C.-Y.; Tang, M.; Wu, L.-L.; Liu, C.; Zhu, L.; Pang, D.-W., Sensitive and quantitative detection of C-reaction protein based on immunofluorescent nanospheres coupled with lateral flow test strip. *Analytical chemistry* **2016**, *88* (12), 6577-6584.
99. Huang, L.; Liao, T.; Wang, J.; Ao, L.; Su, W.; Hu, J., Brilliant Pitaya-Type Silica Colloids with Central-Radial and High-Density Quantum Dots Incorporation for Ultrasensitive Fluorescence Immunoassays. *Advanced Functional Materials* **2018**, *28* (4), 1705380.
100. Reisch, A.; Klymchenko, A. S., Fluorescent polymer nanoparticles based on dyes: seeking brighter tools for bioimaging. *Small* **2016**, *12* (15), 1968-1992.
101. Shulov, I.; Oncul, S.; Reisch, A.; Arntz, Y.; Collot, M.; Mely, Y.; Klymchenko, A. S., Fluorinated counterion-enhanced emission of rhodamine aggregates: ultrabright nanoparticles for bioimaging and light-harvesting. *Nanoscale* **2015**, *7* (43), 18198-18210.
102. Melnychuk, N.; Klymchenko, A. S., DNA-functionalized dye-loaded polymeric nanoparticles: ultrabright FRET platform for amplified detection of nucleic acids. *Journal of the American Chemical Society* **2018**, *140* (34), 10856-10865.

103. Xu, Z.; Peng, S.; Wang, Y. Y.; Zhang, J. K.; Lazar, A. I.; Guo, D. S., Broad-Spectrum Tunable Photoluminescent Nanomaterials Constructed from a Modular Light-Harvesting Platform Based on Macrocyclic Amphiphiles. *Advanced Materials* **2016**, *28* (35), 7666-7671.
104. Kasha, M.; Rawls, H.; El-Bayoumi, M. A., The exciton model in molecular spectroscopy. *Pure and applied Chemistry* **1965**, *11* (3-4), 371-392.
105. Méallet-Renault, R.; Héroult, A.; Vachon, J.-J.; Pansu, R. B.; Amigoni-Gerbier, S.; Larpent, C., Fluorescent nanoparticles as selective Cu (II) sensors. *Photochemical & Photobiological Sciences* **2006**, *5* (3), 300-310.
106. Trofymchuk, K.; Reisch, A.; Shulov, I.; Mély, Y.; Klymchenko, A. S., Tuning the color and photostability of perylene diimides inside polymer nanoparticles: towards biodegradable substitutes of quantum dots. *Nanoscale* **2014**, *6* (21), 12934-12942.
107. Trofymchuk, K.; Reisch, A.; Didier, P.; Fras, F.; Gilliot, P.; Mely, Y.; Klymchenko, A. S., Giant light-harvesting nanoantenna for single-molecule detection in ambient light. *Nature photonics* **2017**, *11* (10), 657.
108. Holmberg, A.; Blomstergren, A.; Nord, O.; Lukacs, M.; Lundeberg, J.; Uhlén, M., The biotin-streptavidin interaction can be reversibly broken using water at elevated temperatures. *Electrophoresis* **2005**, *26* (3), 501-510.
109. Chen, H.; Shao, L.; Li, Q.; Wang, J., Gold nanorods and their plasmonic properties. *Chemical Society Reviews* **2013**, *42* (7), 2679-2724.
110. Huang, X.; Neretina, S.; El-Sayed, M. A., Gold nanorods: from synthesis and properties to biological and biomedical applications. *Advanced Materials* **2009**, *21* (48), 4880-4910.
111. Dreaden, E. C.; Alkilany, A. M.; Huang, X.; Murphy, C. J.; El-Sayed, M. A., The golden age: gold nanoparticles for biomedicine. *Chemical Society Reviews* **2012**, *41* (7), 2740-2779.
112. Ge, S.; Kojio, K.; Takahara, A.; Kajiyama, T., Bovine serum albumin adsorption onto immobilized organotrichlorosilane surface: influence of the phase separation on protein adsorption patterns. *Journal of Biomaterials Science, Polymer Edition* **1998**, *9* (2), 131-150.
113. Ashitate, Y.; Tanaka, E.; Stockdale, A.; Choi, H. S.; Frangioni, J. V., Near-infrared fluorescence imaging of thoracic duct anatomy and function in open surgery and video-assisted thoracic surgery. *The Journal of thoracic and cardiovascular surgery* **2011**, *142* (1), 31-38. e2.
114. Liu, C.; Bao, L.; Tang, B.; Zhao, J. Y.; Zhang, Z. L.; Xiong, L. H.; Hu, J.; Wu, L. L.; Pang, D. W., Fluorescence-converging carbon nanodots-hybridized silica nanosphere. *Small* **2016**, *12* (34), 4702-4706.
115. Cai, Y.; Liu, J. G.; Tazuin, L. J.; Huang, D.; Sung, E.; Zhang, H.; Joplin, A.; Chang, W.-S.; Nordlander, P.; Link, S., Photoluminescence of gold nanorods: Purcell effect enhanced emission from hot carriers. *ACS nano* **2017**.
116. Thompson, D. K.; Huffman, K. M.; Kraus, W. E.; Kraus, V. B., Critical appraisal of four IL-6 immunoassays. *PLoS one* **2012**, *7* (2), e30659.
117. Samant, P. P.; Prausnitz, M. R., Mechanisms of sampling interstitial fluid from skin using a microneedle patch. *Proceedings of the National Academy of Sciences* **2018**, *115* (18), 4583-4588.
118. Munier, M.; Jubeau, S.; Wijaya, A.; Moranchais, M.; Dumay, J.; Marchal, L.; Jaouen, P.; Fleurence, J., Physicochemical factors affecting the stability of two pigments: R-phycoerythrin of *Grateloupia turuturu* and B-phycoerythrin of *Porphyridium cruentum*. *Food chemistry* **2014**, *150*, 400-407.
119. Ma, Y.; Li, W.; Cho, E. C.; Li, Z.; Yu, T.; Zeng, J.; Xie, Z.; Xia, Y., Au@Ag core-shell nanocubes with finely tuned and well-controlled sizes, shell thicknesses, and optical properties. *ACS nano* **2010**, *4* (11), 6725-6734.
120. Liu, K.-K.; Tadepalli, S.; Tian, L.; Singamaneni, S., Size-dependent surface enhanced Raman scattering activity of plasmonic nanorattles. *Chemistry of Materials* **2015**, *27* (15), 5261-5270.

121. Dixit, C. K.; Aguirre, G. R., Protein microarrays with novel microfluidic methods: current advances. *Microarrays* **2014**, *3* (3), 180-202.
122. De La Rica, R.; Stevens, M. M., Plasmonic ELISA for the ultrasensitive detection of disease biomarkers with the naked eye. *Nature nanotechnology* **2012**, *7* (12), 821.
123. Deng, W.; Xie, F.; Baltar, H. T.; Goldys, E. M., Metal-enhanced fluorescence in the life sciences: here, now and beyond. *Physical Chemistry Chemical Physics* **2013**, *15* (38), 15695-15708.
124. Anker, J. N.; Hall, W. P.; Lyandres, O.; Shah, N. C.; Zhao, J.; Van Duyne, R. P., Biosensing with plasmonic nanosensors. *Nature materials* **2008**, *7* (6), 442-453.
125. Joshi, G. K.; Deitz-McElyea, S.; Johnson, M.; Mali, S.; Korc, M.; Sardar, R., Highly specific plasmonic biosensors for ultrasensitive microRNA detection in plasma from pancreatic cancer patients. *Nano letters* **2014**, *14* (12), 6955-6963.
126. Kelly, K. L.; Coronado, E.; Zhao, L. L.; Schatz, G. C., The optical properties of metal nanoparticles: the influence of size, shape, and dielectric environment. *The Journal of Physical Chemistry B* **2003**, *107* (3), 668-677.
127. Stewart, M. E.; Anderton, C. R.; Thompson, L. B.; Maria, J.; Gray, S. K.; Rogers, J. A.; Nuzzo, R. G., Nanostructured plasmonic sensors. *Chemical reviews* **2008**, *108* (2), 494-521.
128. Mayer, K. M.; Lee, S.; Liao, H.; Rostro, B. C.; Fuentes, A.; Scully, P. T.; Nehl, C. L.; Hafner, J. H., A label-free immunoassay based upon localized surface plasmon resonance of gold nanorods. *ACS nano* **2008**, *2* (4), 687-692.
129. Tadepalli, S.; Kuang, Z.; Jiang, Q.; Liu, K.-K.; Fisher, M. A.; Morrissey, J. J.; Kharasch, E. D.; Slocik, J. M.; Naik, R. R.; Singamaneni, S., Peptide functionalized gold nanorods for the sensitive detection of a cardiac biomarker using plasmonic paper devices. *Scientific reports* **2015**, *5*.
130. Acimovic, S. S.; Ortega, M. A.; Sanz, V.; Berthelot, J.; Garcia-Cordero, J. L.; Renger, J.; Maerkl, S. J.; Kreuzer, M. P.; Quidant, R., LSPR chip for parallel, rapid, and sensitive detection of cancer markers in serum. *Nano letters* **2014**, *14* (5), 2636-2641.
131. Masson, J.-F., Surface plasmon resonance clinical biosensors for medical diagnostics. *ACS Sensors* **2017**, *2* (1), 16-30.
132. Gorodkiewicz, E.; Sankiewicz, A.; Laudański, P., Surface plasmon resonance imaging biosensors for aromatase based on a potent inhibitor and a specific antibody: Sensor development and application for biological material. *Open Chemistry* **2014**, *12* (5), 557-567.
133. Ye, L.; Mosbach, K., Molecular imprinting: synthetic materials as substitutes for biological antibodies and receptors. *Chemistry of Materials* **2008**, *20* (3), 859-868.
134. Benito-Peña, E.; Navarro-Villoslada, F.; Carrasco, S.; Jockusch, S.; Ottaviani, M. F.; Moreno-Bondi, M. C., Experimental mixture design as a tool for the synthesis of antimicrobial selective molecularly imprinted monodisperse microbeads. *ACS applied materials & interfaces* **2015**, *7* (20), 10966-10976.
135. Xu, J.; Haupt, K.; Tse Sum Bui, B., Core-Shell Molecularly Imprinted Polymer Nanoparticles as Synthetic Antibodies in a Sandwich Fluoroimmunoassay for Trypsin Determination in Human Serum. *ACS Applied Materials & Interfaces* **2017**, *9* (29), 24476-24483.
136. Liu, J.; Yin, D.; Wang, S.; Chen, H. Y.; Liu, Z., Probing Low-Copy-Number Proteins in a Single Living Cell. *Angewandte Chemie International Edition* **2016**, *55* (42), 13215-13218.
137. Muhammad, P.; Tu, X.; Liu, J.; Wang, Y.; Liu, Z., Molecularly Imprinted Plasmonic Substrates for Specific and Ultrasensitive Immunoassay of Trace Glycoproteins in Biological Samples. *ACS Applied Materials & Interfaces* **2017**, *9* (13), 12082-12091.
138. Luan, J.; Liu, K.-K.; Tadepalli, S.; Jiang, Q.; Morrissey, J. J.; Kharasch, E. D.; Singamaneni, S., PEGylated Artificial Antibodies: Plasmonic Biosensors with Improved Selectivity. *ACS applied materials & interfaces* **2016**, *8* (36), 23509-23516.

139. Sun, Y.; Mayers, B.; Xia, Y., Metal nanostructures with hollow interiors. *Adv. Mater.* **2003**, *15* (7-8), 641-646.
140. Shiomi, T.; Matsui, M.; Mizukami, F.; Sakaguchi, K., A method for the molecular imprinting of hemoglobin on silica surfaces using silanes. *Biomaterials* **2005**, *26* (27), 5564-5571.
141. Wang, C.; Hu, R.; Morrissey, J. J.; Kharasch, E. D.; Singamaneni, S., Single Molecule Force Spectroscopy to Compare Natural versus Artificial Antibody–Antigen Interaction. *Small* **2017**.
142. Ko, G. J.; Grigoryev, D. N.; Linfert, D.; Jang, H. R.; Watkins, T.; Cheadle, C.; Racusen, L.; Rabb, H., Transcriptional analysis of kidneys during repair from AKI reveals possible roles for NGAL and KIM-1 as biomarkers of AKI-to-CKD transition. *American Journal of Physiology-Renal Physiology* **2010**, *298* (6), F1472-F1483.
143. Adiyanti, S. S.; Loho, T., Acute kidney injury (AKI) biomarker. *Acta Med Indones* **2012**, *44* (3), 246-55.
144. Mehta, R. L.; Kellum, J. A.; Shah, S. V.; Molitoris, B. A.; Ronco, C.; Warnock, D. G.; Levin, A., Acute Kidney Injury Network: report of an initiative to improve outcomes in acute kidney injury. *Critical care* **2007**, *11* (2), R31.
145. Li, P. K. T.; Burdmann, E. A.; Mehta, R. L.; Committee, W. K. D. S., Acute kidney injury: global health alert. *Kidney international* **2013**, *83* (3), 372-376.
146. Shao, X.; Tian, L.; Xu, W.; Zhang, Z.; Wang, C.; Qi, C.; Ni, Z.; Mou, S., Diagnostic value of urinary kidney injury molecule 1 for acute kidney injury: a meta-analysis. *PLoS One* **2014**, *9* (1), e84131.
147. Jana, N. R.; Gearheart, L.; Murphy, C. J., Wet chemical synthesis of high aspect ratio cylindrical gold nanorods. *The Journal of Physical Chemistry B* **2001**, *105* (19), 4065-4067.
148. Nikoobakht, B.; El-Sayed, M. A., Preparation and growth mechanism of gold nanorods (NRs) using seed-mediated growth method. *Chemistry of Materials* **2003**, *15* (10), 1957-1962.
149. Buerk, D., Enzyme-based Electrochemical Biosensors. *Biosensors—Theory and Applications*. Lancaster, PA: Technomic Publication Co **1993**, 90-91.
150. Luong, J. H.; Male, K. B.; Glennon, J. D., Biosensor Technology: Technology Push Versus Market Pull. *Biotechnol. Adv.* **2008**, *26* (5), 492-500.
151. Stefan, R.-I.; Van Staden, J.; Aboul-Enein, H. Y., Immunosensors in Clinical Analysis. *Fresenius J Anal Chem* **2000**, *366* (6-7), 659-668.
152. Wang, C.; Luan, J.; Tadepalli, S.; Liu, K.-K.; Morrissey, J. J.; Kharasch, E. D.; Naik, R. R.; Singamaneni, S., Silk-Encapsulated Plasmonic Biochips with Enhanced Thermal Stability. *ACS Appl. Mater. Interfaces* **2016**.
153. Chen, H.; Kou, X.; Yang, Z.; Ni, W.; Wang, J., Shape-and Size-dependent Refractive Index Sensitivity of Gold Nanoparticles. *Langmuir* **2008**, *24* (10), 5233-5237.
154. Anker, J. N.; Hall, W. P.; Lyandres, O.; Shah, N. C.; Zhao, J.; Van Duyne, R. P., Biosensing with Plasmonic Nanosensors. *Nat. Mater* **2008**, *7* (6), 442-453.
155. Rogers, J.; Nuzzo, R., Nanostructured Plasmonic Sensors. *Chem Rev* **2008**, *108* (2), 4945-21.
156. Mayer, K. M.; Hafner, J. H., Localized Surface Plasmon Resonance Sensors. *Chem. Rev* **2011**, *111* (6), 3828-3857.
157. Mosbach, K.; Ramström, O., The Emerging Technique of Molecular Imprinting and its Future Impact of Biotechnology. *Bio/technology* **1996**, *14* (2), 163-170.
158. Haupt, K.; Mosbach, K., Molecularly Imprinted Polymers and Their Use in Biomimetic Sensors. *Chem. Rev* **2000**, *100* (7), 2495-2504.
159. Wulff, G., Molecular Imprinting in Cross-linked Materials with the Aid of Molecular Templates—a Way towards Artificial Antibodies. *Angew. Chem. Int. Ed. Engl.* **1995**, *34* (17), 1812-1832.

160. Shea, K. J. In *Molecular Imprinting of Synthetic Network Polymers-the De-novo Synthesis of Macromolecular Binding and Catalytic Sites*, Abstr Pap Am Chem S, AMER CHEMICAL SOC 1155 16TH ST, NW, WASHINGTON, DC 20036: 1994; pp 467-POLY.
161. Dutta, P.; Pernites, R. B.; Danda, C.; Advincula, R. C., SPR Detection of Dopamine Using Cathodically Electropolymerized, Molecularly Imprinted Poly-p-aminostyrene Thin Films. *Macromol. Chem. Phys.* **2011**, *212* (22), 2439-2451.
162. Cai, D.; Ren, L.; Zhao, H.; Xu, C.; Zhang, L.; Yu, Y.; Wang, H.; Lan, Y.; Roberts, M. F.; Chuang, J. H., A Molecular-imprint Nanosensor for Ultrasensitive Detection of Proteins. *Nat. Nanotechnol* **2010**, *5* (8), 597-601.
163. Haupt, K., Biomaterials: Plastic Antibodies. *Nat. Mater* **2010**, *9* (8), 612-614.
164. Bui, B. T. S.; Haupt, K., Molecularly Imprinted Polymers: Synthetic Receptors in Bioanalysis. *Anal. Bioanal. Chem* **2010**, *398* (6), 2481-2492.
165. Abbas, A.; Tian, L.; Morrissey, J. J.; Kharasch, E. D.; Singamaneni, S., Hot Spot-Localized Artificial Antibodies for Label-Free Plasmonic Biosensing. *Adv. Funct. Mater.* **2013**, *23* (14), 1789-1797.
166. Tian, L.; Liu, K.-K.; Morrissey, J. J.; Gandra, N.; Kharasch, E. D.; Singamaneni, S., Gold Nanocages with Built-in Artificial Antibodies for Label-free Plasmonic Biosensing. *J. Mater. Chem. B* **2014**, *2* (2), 167-170.
167. Asanuma, H.; Hishiya, T.; Komiyama, M., Tailor-made Receptors by Molecular Imprinting. *Adv. Mater* **2000**, *12* (14), 1019-1030.
168. Sellergren, B., *Molecularly Imprinted Polymers: Man-made Mimics of Antibodies and Their Application in Analytical Chemistry*. Elsevier: 2000; Vol. 23.
169. Komiyama, M.; Takeuchi, T.; Mukawa, T.; Asanuma, H., Front Matter. *Molecular Imprinting: From Fundamentals to Applications* **2003**, i-xii.
170. Turner, N. W.; Jeans, C. W.; Brain, K. R.; Allender, C. J.; Hlady, V.; Britt, D. W., From 3D to 2D: a Review of the Molecular Imprinting of Proteins. *Biotechnol Prog* **2006**, *22* (6), 1474-1489.
171. Hoshino, Y.; Kodama, T.; Okahata, Y.; Shea, K. J., Peptide Imprinted Polymer Nanoparticles: a Plastic Antibody. *J. Am. Chem. Soc* **2008**, *130* (46), 15242-15243.
172. Tov, O. Y.; Luvitch, S.; Bianco-Peled, H., Molecularly Imprinted Hydrogel Displaying Reduced Non-specific Binding and Improved Protein Recognition. *J Sep Sci* **2010**, *33* (11), 1673-1681.
173. Nishino, H.; Huang, C. S.; Shea, K. J., Selective Protein Capture by Epitope Imprinting. *Angew. Chem. Int. Ed.* **2006**, *45* (15), 2392-2396.
174. Qian, X.; Peng, X.-H.; Ansari, D. O.; Yin-Goen, Q.; Chen, G. Z.; Shin, D. M.; Yang, L.; Young, A. N.; Wang, M. D.; Nie, S., In Vivo Tumor Targeting and Spectroscopic Detection with Surface-enhanced Raman Nanoparticle Tags. *Nat. Biotechnol* **2008**, *26* (1), 83-90.
175. Cheng, L.; Wang, C.; Feng, L.; Yang, K.; Liu, Z., Functional Nanomaterials for Phototherapies of Cancer. *Chem. Rev* **2014**, *114* (21), 10869-10939.
176. Pochechueva, T.; Chinarev, A.; Bovin, N.; Fedier, A.; Jacob, F.; Heinzelmann-Schwarz, V., PEGylation of Microbead Surfaces Reduces Unspecific Antibody Binding in Glycan-based Suspension Array. *J Immunol Methods* **2014**, *412*, 42-52.
177. Sun, Y.; Mayers, B.; Xia, Y., Metal Nanostructures with Hollow Interiors. *Adv. Mater* **2003**, *15* (7-8), 641-646.
178. Morrissey, J. J.; Kharasch, E. D., The Specificity of Urinary Aquaporin 1 and Perilipin 2 to Screen for Renal Cell Carcinoma. *J. Urol.* **2013**, *189* (5), 1913-1920.
179. Wong, E. K.; Goodship, T. H.; Kavanagh, D., Complement Therapy in Atypical Haemolytic Uraemic Syndrome (aHUS). *Mol Immunol* **2013**, *56* (3), 199-212.

180. Hill, A.; Kelly, R. J.; Hillmen, P., Thrombosis in Paroxysmal Nocturnal Hemoglobinuria. *Blood* **2013**, *121* (25), 4985-4996.
181. HAM, T. H., Studies on Destruction of Red Blood Cells: I. Chronic Hemolytic Anemia with Paroxysmal Nocturnal Hemoglobinuria: an Investigation of the Mechanism of Hemolysis, with Observations on Five Cases. *Arch Intern Med* **1939**, *64* (6), 1271-1305.
182. Zheng, Y.; Ma, Y.; Zeng, J.; Zhong, X.; Jin, M.; Li, Z.-Y.; Xia, Y., Seed-Mediated Synthesis of Single-Crystal Gold Nanospheres with Controlled Diameters in the Range 5–30 nm and their Self-Assembly upon Dilution. *Chem Asian J* **2013**, *8* (4), 792-799.
183. Ma, Y.; Li, W.; Cho, E. C.; Li, Z.; Yu, T.; Zeng, J.; Xie, Z.; Xia, Y., Au@Ag Core–Shell Nanocubes with Finely Tuned and Well-Controlled Sizes, Shell Thicknesses, and Optical Properties. *ACS Nano* **2010**, *4* (11), 6725-6734.
184. Xia, X.; Wang, Y.; Ruditskiy, A.; Xia, Y., 25th Anniversary Article: Galvanic Replacement: A Simple and Versatile Route to Hollow Nanostructures with Tunable and Well-Controlled Properties. *Adv. Mater* **2013**, *25* (44), 6313-6333.
185. Sun, Y.; Mayers, B.; Xia, Y., Metal Nanostructures with Hollow Interiors. *Advanced Materials* **2003**, *15* (7-8), 641-646.
186. Gandra, N.; Portz, C.; Singamaneni, S., Biomedical Applications: Multifunctional Plasmonic Nanorattles for Spectrum-Guided Locoregional Therapy (Adv. Mater. 3/2014). *Adv. Mater* **2014**, *26* (3), 350-350.
187. Sharma, S.; Johnson, R. W.; Desai, T. A., XPS and AFM Analysis of Antifouling PEG Interfaces for Microfabricated Silicon Biosensors. *Biosens. Bioelectron* **2004**, *20* (2), 227-239.
188. Ross, P. D.; Subramanian, S., Thermodynamics of Protein Association Reactions: Forces Contributing to Stability. *Biochemistry* **1981**, *20* (11), 3096-3102.
189. Cram, D. J., The Design of Molecular Hosts, Guests, and their Complexes (Nobel lecture). *Angew. Chem. Int. Ed. Engl.* **1988**, *27* (8), 1009-1020.
190. Levey, A. S.; Eckardt, K.-U.; Tsukamoto, Y.; Levin, A.; Coresh, J.; Rossert, J.; Zeeuw, D. D.; Hostetter, T. H.; Lameire, N.; Eknoyan, G., Definition and Classification of Chronic Kidney Disease: a Position Statement from Kidney Disease: Improving Global Outcomes (KDIGO) *Kidney Int* **2005**, *67* (6), 2089-2100.
191. Gibney, R. N.; Sever, M. S.; Vanholder, R. C., Disaster Nephrology: Crush Injury and Beyond. *Kidney Int* **2014**, *85* (5), 1049-1057.
192. Willets, K. A.; Van Duyne, R. P., Localized surface plasmon resonance spectroscopy and sensing. In *Annual Review of Physical Chemistry*, 2007; Vol. 58, pp 267-297.
193. Zarick, H. F.; Erwin, W. R.; Boulesbaa, A.; Hurd, O. K.; Webb, J. A.; Puretzky, A. A.; Geohegan, D. B.; Bardhan, R., Improving Light Harvesting in Dye-Sensitized Solar Cells Using Hybrid Bimetallic Nanostructures. *Acs Photonics* **3** (3), 385-394.
194. Abadeer, N. S.; Murphy, C. J., Recent Progress in Cancer Thermal Therapy Using Gold Nanoparticles. *Journal of Physical Chemistry C* **120** (9), 4691-4716.
195. Anker, J. N.; Hall, W. P.; Lyandres, O.; Shah, N. C.; Zhao, J.; Van Duyne, R. P., Biosensing with plasmonic nanosensors. *Nat Mater* **2008**, *7* (6), 442-453.
196. Tadepalli, S.; Kuang, Z.; Jiang, Q.; Liu, K.-K.; Fisher, M. A.; Morrissey, J. J.; Kharasch, E. D.; Slocik, J. M.; Naik, R. R.; Singamaneni, S., Peptide Functionalized Gold Nanorods for the Sensitive Detection of a Cardiac Biomarker Using Plasmonic Paper Devices. *Scientific Reports* **2015**, *5*, 16206.
197. Wang, C.; Luan, J.; Tadepalli, S.; Liu, K.-K.; Morrissey, J. J.; Kharasch, E. D.; Naik, R. R.; Singamaneni, S., Silk-Encapsulated Plasmonic Biochips with Enhanced Thermal Stability. *ACS Applied Materials & Interfaces* **2016**.

198. Abbas, A.; Tian, L. M.; Morrissey, J. J.; Kharasch, E. D.; Singamaneni, S., Hot Spot-Localized Artificial Antibodies for Label-Free Plasmonic Biosensing. *Advanced Functional Materials* **2013**, *23* (14), 1789-1797.
199. Limei, T.; Keng-Ku, L.; Morrissey, J. J.; Gandra, N.; Kharasch, E. D.; Singamaneni, S., Gold nanocages with built-in artificial antibodies for label-free plasmonic biosensing. *J. Mater. Chem. B* **2014**, *2* (2), 167-170.
200. Luan J, L. K., Tadepalli S, Jiang Q, Morrissey JJ, Kharasch ED, Singamaneni S, PEGlated Artificial Antibodies: Plasmonic Biosensors with Improved Selectivity. *Acs Applied Materials & Interfaces* **2016**, *In press*.
201. Chen, L. X.; Wang, X. Y.; Lu, W. H.; Wu, X. Q.; Li, J. H., Molecular imprinting: perspectives and applications. *Chemical Society Reviews* **2016**, *45* (8), 2137-2211.
202. Yan, H. Y.; Row, K. H., Characteristic and synthetic approach of molecularly imprinted polymer. *International Journal of Molecular Sciences* **2006**, *7* (5-6), 155-178.
203. Lofgreen, J. E.; Ozin, G. A., Controlling morphology and porosity to improve performance of molecularly imprinted sol-gel silica. *Chemical Society Reviews* **2014**, *43* (3), 911-933.
204. Whitcombe, M. J.; Kirsch, N.; Nicholls, I. A., Molecular imprinting science and technology: a survey of the literature for the years 2004-2011. *Journal of Molecular Recognition* **2014**, *27* (6), 297-401.
205. Sari, E.; Uzek, R.; Duman, M.; Denizli, A., Fabrication of surface plasmon resonance nanosensor for the selective determination of erythromycin via molecular imprinted nanoparticles. *Talanta* **2016**, *150*, 607-614.
206. Hongyan, H.; Guoqi, F.; Yan, W.; Zhihua, C.; Yizhe, J.; Zilun, C., Imprinting of protein over silica nanoparticles via surface graft copolymerization using low monomer concentration. *Biosens. Bioelectron.* **2010**, *26* (2), 760-765.
207. Takeuchi, T.; Hishiya, T., Molecular imprinting of proteins emerging as a tool for protein recognition. *Organic & Biomolecular Chemistry* **2008**, *6* (14), 2459-2467.
208. Hansen, D. E., Recent developments in the molecular imprinting of proteins. *Biomaterials* **2007**, *28* (29), 4178-4191.
209. Lv, T. W.; Yan, H. Y.; Cao, J. K.; Liang, S. R., Hydrophilic Molecularly Imprinted Resorcinol-Formaldehyde-Melamine Resin Prepared in Water with Excellent Molecular Recognition in Aqueous Matrices. *Analytical Chemistry* **2015**, *87* (21), 11084-11091.
210. Bhakta, S.; Seraji, M. S. I.; Suib, S. L.; Rusling, J. F., Antibody-like Biorecognition Sites for Proteins from Surface Imprinting on Nanoparticles. *Acs Applied Materials & Interfaces* **2015**, *7* (51), 28197-28206.
211. Li, F.; Li, J.; Zhang, S. S., Molecularly imprinted polymer grafted on polysaccharide microsphere surface by the sol-gel process for protein recognition. *Talanta* **2008**, *74* (5), 1247-1255.
212. Cumbo, A.; Lorber, B.; Corvini, P. F. X.; Meier, W.; Shahgaldian, P., A synthetic nanomaterial for virus recognition produced by surface imprinting. *Nature Communications* **2013**, *4*.
213. Yang, Y. Q.; He, X. W.; Wang, Y. Z.; Li, W. Y.; Zhang, Y. K., Epitope imprinted polymer coating CdTe quantum dots for specific recognition and direct fluorescent quantification of the target protein bovine serum albumin. *Biosens. Bioelectron.* **2014**, *54*, 266-272.
214. Stewart, S.; Fredericks, P. M., Surface-enhanced Raman spectroscopy of peptides and proteins adsorbed on an electrochemically prepared silver surface. *Spectrochimica Acta Part a-Molecular and Biomolecular Spectroscopy* **1999**, *55* (7-8), 1615-1640.
215. Wulff, G., Forty years of molecular imprinting in synthetic polymers: origin, features and perspectives. *Microchimica Acta* **2013**, *180* (15-16), 1359-1370.

Curriculum Vitae

Jingyi Luan

PhD, McDonnell International Scholar

Department of Mechanical Engineering & Materials Science

Washington University in St. Louis

luanjingyi@wustl.edu

RESEARCH INTERESTS

Innovative design and fabrication of functional plasmonically-active nanomaterials and devices to overcome scientific and technological barriers in the implementation of ultrasensitive nanosensors in point-of-care and resource-limited settings.

Research Expertise Summary: Plasmonic nanomedicine (in vitro biosensing for point-of-care diagnostics, molecular bioimaging), plasmon-enhanced fluorescence and surface enhanced Raman scattering (SERS)-based biological and chemical sensors with particular emphasis on the design and fabrication of unconventional and highly efficient plasmonically active material, multifunctional materials based on bacterial nanocellulose, metal-organic frameworks for biopreservation, silk based microstructure, bioinspired structural

and functional materials, polymer surfaces and interfaces, responsive and adaptive materials and scanning probe microscopy of soft and biological materials.

EDUCATION

PhD candidate, Mechanical Engineering & Materials Science

2014-present

Washington University in St. Louis

St. Louis,

U SA

Advisor: Prof. Srikanth Singamaneni

2014-present

Exchange program, Electrical Engineering and Computer Sciences

2012-

2013

University of California, Berkeley

Berkeley,

USA

Bachelor of Engineering, Electronic and Information Engineering

2013

Xi'an Jiaotong University

Xi'an, CN

PEER-REVIEWED PUBLICATIONS (in order of time the paper was prepared and accepted)

1. Liang, C.; **Luan, J. (Co-first author)**; Wang, Z.; Gupta R.; Cao, S.; Sun, H.; Kharasch, E. D.; Morrissey, J. J.; Singamaneni, S., Optically Tailored Plasmonic Patch for Femtomolar Detection of Protein Biomarkers. In preparation, 2020.
2. Wang, Z.; **Luan, J. (Co-first author)**; Seth, A; Liu, L.; You, M.; Singamaneni, S., Minimally invasive and ultrasensitive monitor of protein biomarkers in interstitial fluid using microneedle patch. In preparation, 2020.
3. **Luan, J.**; Gupta, R.; Singamaneni, S., Plasmonic Biosensors based on Molecularly Imprinted Polymer as Biorecognition layer (review). In preparation, 2020.
4. Zhang, M.; **Luan, J.**; Morrissey, J. J.; Cao, S.; Wang, Z.; Jiang, Q.; Kharasch, E.; Singamaneni, S., Femtomolar detection of protein biomarkers based on SERS sandwich immunoassay. In preparation, 2020.
5. **Luan, J.**; Seth, A; Gupta, R; Wang, Z.; Derami, H.; Rathi, P; Cao, S.; Singamaneni, S., Ultrabright Plasmonic-fluor as a Cross-platform Nanolabel for Femtomolar Detection of Bioanalytes. **Nature Biomedical Engineering**, accepted, 2020.
6. Gupta, R.; **Luan, J.**; Chakrabartty, S.; Scheller, E. L.; Morrissey, J. J.; Singamaneni, S., Refreshable Nanobiosensor based on Organosilica Encapsulation of Biorecognition Elements. *ACS Applied Materials & Interfaces* 2020, 12, 5420–5428 (**Journal impact factor: 8.457**)

7. Xiong, R.; **Luan, J.**; Kang, S.; Ye, C.; Singamaneni, S.; Tsukruk, V. V., Biopolymeric photonic structures: design, fabrication, and emerging applications. *Chemical Society Reviews*, 2020 (**Journal impact factor: 40.4**)
8. Gupta, P.; **Luan, J.**; Wang, Z.; Cao, S.; Naik, R.; Singamaneni, S., Add-On Plasmonic Patch for On-demand Electromagnetic Hotspots. *ACS Applied Materials & Interfaces* 2019, 11, 37939–37946 (**Journal impact factor: 8.457**)
9. Cao, S.; Tang, R.; Sudlow, G.; Wang, Z.; Liu, K.-K.; **Luan, J.**; Tadepalli, S.; Achilefu, S.; Singamaneni, S., Red Blood Cell Mimicking Silk Microcapsules. *ACS Applied Material and Interface*, 2019, 11, 5499–5508 (**Journal impact factor: 8.457**).
10. Jiang, Q.; Deoukchen, G.; Tadepalli, S.; Liu, K.-K.; Kwon, H.; **Luan, J.**; Min, Y.; Jun, Y.-S.; Singamaneni, S., Photothermally Active Reduced Graphene Oxide/Bacterial Nanocellulose Composites as Biofouling-Resistant Ultrafiltration Membranes. *Environmental science & technology*, 2019, 53, 412–421. (**Journal impact factor: 6.198**)
11. **Luan, J.**; Xu, T.; Morrissey, J. J.; Kharasch, E. D.; Singamaneni, S., Environmental Stability of Plasmonic Biosensors based on Natural vs. Artificial Antibody. *Analytical Chemistry* 2018, 90, 13, 7880-7887. (**Journal impact factor: 6.32**)
12. **Luan, J.**; Morrissey, J.; Wang, Z.; Derami, H.; Liu, K-K.; Cao, S.; Jiang, Q.; Wang, C.; Kharasch, E.; Naik, R.; Singamaneni, S., Add-on Plasmonic Patch as a Universal Fluorescence Enhancer. *Light: Science & Applications*, 7, 29 (2018). (**Journal impact factor: 14.1**)

13. Wang, C.; Sun, H.; **Luan, J.**; Jiang, Q.; Tadepalli, S.; Morrissey, J. J.; Kharasch, E. D.; Singamaneni, S., Metal-Organic Framework Encapsulation for Biospecimen Preservation. *Chemistry of Materials*, 2018, 30, 4, 1291-1300 (**Journal impact factor: 9.89**)
14. Tadepalli, S.; Yim, J.; Madireddi, K.; **Luan, J.**; Naik, R. R.; Singamaneni, S., Gold Nanorod-Mediated Photothermal Enhancement of the Biocatalytic Activity of a Polymer-Encapsulated Enzyme. *Chemistry of Materials* 2017, 29 (15), 6308-6314. (**Journal impact factor: 9.89**)
15. Wang, C.; Tadepalli, S.; **Luan, J.**; Liu, K. K.; Morrissey, J. J.; Kharasch, E. D.; Naik, R. R.; Singamaneni, S., Metal-Organic Framework as a Protective Coating for Biodiagnostic Chips. *Advanced Materials* 2017, 29 (7). (**Journal impact factor: 21.95**)
16. **Luan, J.**; Hu, R.; Tadepalli, S.; Morrissey, J. J.; Kharasch, E. D.; Singamaneni, S., Amplification of Refractometric Biosensor Response through Biomineralization of Metal–Organic Framework Nanocrystals. *Advanced Materials Technologies* 2017, 2 (7). (**Journal impact factor: 4.6**)
17. Tian, L.; **Luan, J.**; Liu, K.-K.; Jiang, Q.; Tadepalli, S.; Gupta, M. K.; Naik, R. R.; Singamaneni, S., Plasmonic Biofoam: A Versatile Optically Active Material. *Nano Letters* 2016, 16 (1), 609-616. (**Journal impact factor: 12.1**)
18. **Luan, J.**; Liu, K.-K.; Tadepalli, S.; Jiang, Q.; Morrissey, J. J.; Kharasch, E. D.; Singamaneni, S., PEGylated Artificial Antibodies: Plasmonic Biosensors with Improved Selectivity. *ACS Applied Materials & Interfaces* 2016, 8 (36), 23509-23516. (**Journal impact factor: 8.457**)

19. Wang, C.; **Luan, J.**; Tadepalli, S.; Liu, K.-K.; Morrissey, J. J.; Kharasch, E. D.; Naik, R. R.; Singamaneni, S., Silk-Encapsulated Plasmonic Biochips with Enhanced Thermal Stability. *ACS applied materials & interfaces* 2016, 8 (40), 26493-26500. (**Journal impact factor: 8.457**)
20. Tian, L.; Jiang, Q.; Liu, K.-K.; **Luan, J.**; Naik, R. R.; Singamaneni, S., Bacterial Nanocellulose-Based Flexible Surface Enhanced Raman Scattering Substrate. *Advanced Materials Interfaces* 2016, 3 (15), 1600214. (**Journal impact factor: 4.83**)

SELECTED PRESENTATIONS

Oral presentations

Materials Research Society

Boston, USA, 2017

Dramatic Enhancement of Fluorescence in Bioassays via a Lighting-Up Plasmonic Patch

Poster presentation

Materials Research Society

Boston, USA, 2017

PEGylated Artificial Antibodies: Plasmonic Biosensors with Improved Selectivity

Poster presentation

Ultrabright Plasmonic-fluor as a Cross-platform Nanolabel for Femtomolar Detection of
Bioanalytes